

NORTHWESTERN UNIVERSITY

Atomistic Modeling of Defects and Phase Transformations in Energy  
Materials

A DISSERTATION

SUBMITTED TO THE GRADUATE SCHOOL  
IN PARTIAL FULFILLMENT OF THE REQUIREMENTS

for the degree

DOCTOR OF PHILOSOPHY

Field of Materials Science & Engineering

By

Shane Patel

EVANSTON, ILLINOIS

March 2023

© Copyright by Shane Patel 2023

All Rights Reserved

## ABSTRACT

Atomistic Modeling of Defects and Phase Transformations in Energy Materials

Shane Patel

Atomistic methods offer a powerful set of tools in the study of materials systems, as they allow materials scientists to ask questions with a high degree of specificity. They are well suited for studying and designing energy materials, critical due to the climate crisis, in part due to their ability to probe defect properties. In this document, we present projects that extend the reach of these tools, and use them to study both long established materials systems, such as Zr cladding in nuclear reactors, as well as cutting edge materials such as disordered layered Li-ion battery cathodes. We begin with a brief overview of how defects are studied using atomistic methods, and how this can apply to different energy material systems, in Chapter 2.

In Chapter 3, we adapt the minima hopping method (MHM) to interfacial structure prediction and apply it to study a canonical problem, the non-stoichiometric grain boundaries in  $\text{SrTiO}_3$ . Our method employs a hybrid approach by first exploring the potential energy surface with an empirical force field to generate candidate structures, which are then refined using *ab-initio* Density Functional Theory (DFT) calculations. Using this

approach, we find stable interfacial structures for SrTiO<sub>3</sub> (111) and (112) grain boundaries that are lower in energy compared to those reported in the literature for given system size. Our method allows the prediction of interfacial structure at the atomic scale to improve our understanding of grain boundaries and heterointerfaces.

In Chapter 4, we study the role of cation disorder in Li<sub>3</sub>IrO<sub>4</sub> cathodes, which have alternating cation planes of pure Li layers and a disordered Ir-Li plane, in facilitating anionic redox, using DFT. We calculate a cluster expansion to explore structural stability in the fully lithiated phase, and subsequently calculate the behavior upon delithiation of both a stable ordered structure and a model disordered structure. We then perform a high-throughput screening of Li<sub>3</sub>MO<sub>4</sub> structures, uncovering novel phases and identifying Li<sub>3</sub>OsO<sub>4</sub>, Li<sub>3</sub>PtO<sub>4</sub>, and Li<sub>3</sub>RhO<sub>4</sub> as potential candidates for further study as a battery cathode.

In Chapter 5, we have developed a novel Moment Tensor Potential (MTP), a class of machine learning interatomic potentials, to flexibly treat dissolved hydrogen in hexagonal  $\alpha$ -Zirconium in tetrahedral and octahedral interstitial sites, as well as the variety of relevant hydride phases:  $\gamma$ -ZrH, the dominant  $\delta$ -ZrH<sub>2-x</sub>, and  $\epsilon$ -ZrH<sub>2</sub>. Our approach is to train MTP using an active learning scheme based on NPT classical molecular dynamics (MD) simulations at varying temperatures. Our trained MTP is capable of modeling the phase transformation at the solvus boundary between metallic  $\alpha$ -Zr and the hydride phases in excellent agreement with DFT, while also capturing the temperature and compositional dependence of the  $\epsilon$ -ZrH<sub>2</sub> to  $\delta$ -ZrH<sub>2-x</sub> transformation. Finally, we validate the capability of the MTP to capture relevant phenomena such as H diffusion, H-vacancy ordering, and point and planar defect behavior.

## Acknowledgements

The pursuit of my PhD was made possible and enriched by many people, both within and outside the Materials Science community, whose contributions I would like to thank here.

My advisor, Professor Chris Wolverton, supported me throughout my journey. His depth of knowledge of the materials science literature and sharp questions consistently proved to be invaluable, and he always provided me the intellectual freedom to pursue problems and questions that I found interesting. As the leader of our research group, Chris's approach to science has fostered an inclusive and open environment for the pursuit of knowledge and the growth of skills and expertise.

The bulk of my intellectual growth during graduate school has been due to the nurturing of and enthusiastic mentorship with senior members of the Wolverton group. Former post-docs Drs. Shiqiang Hao and Jiangang He were invaluable in teaching me the hands-on, practical fundamentals of atomistic modeling and Density Functional Theory. Drs. Maximilian Amsler and Yi Xia were my primary collaborators on two of the projects I led. Both developed tools and approaches that were used extensively in my research, while also providing careful eyes as co-authors and invaluable mentorship throughout the research and writing process as we tackled challenging problems. Drs. Eric Isaacs and Yizhou Zhu provided deep knowledge of modeling battery systems, and were also enthusiastic collaborators. Senior graduate students in the group also provided invaluable mentorship

during my first few years and helped get my career as a materials scientist off the ground, in particular Drs. David Snyder, Vinay Hegde, Logan Ward, and Zhenpeng Yao. In my last few years of graduate school, I've had the privilege of mentoring new members of our group, and I always try to pay forward the generosity of time I was shown by my predecessors.

My internal committee members, Professors Sossina M. Haile and Vinayak P. Dravid provided crucial guidance and experimental perspective of battery systems, especially during the early years of my PhD. My external committee member, Dr. Maria K. Chan, offered enthusiastic support throughout my PhD as well, and was always eager to discuss new directions during our CEES EFRC meetings.

At Rutgers University, I had the pleasure of working with Professor Dunbar P. Birnie and Dr. Brian Vezbicke, who first piqued my interest in materials science as a way to address the climate crisis.

Over the last decade, I've made countless friends and comrades involved in the climate justice movement, in particular those who I've organized with in Sunrise Chicago and the fossil fuel divestment movement. Your clarity of purpose and solidarity through incredibly murky social and political circumstances has been a source of perseverance and hope in my life.

I was very lucky to have a close group of friends during graduate school, primarily established as we struggled through our first class in Computational Materials Science: Max D, Max W, Shreya, Chris M, Michaela, Rohit, and Tiffany. I will always remember so fondly the time (and food!) we shared together, just steps away from Lake Michigan's best beachfront park, Loyola Beach.

My groups of friends from Rutgers, who I've only grown closer to since we've left school. Beverly, Jen, Sylvia, Kevin, Glenn, Max, Allison, and Ryan. Thanks for always being down to chat, hangout, visit, meander around NYC, and make incredible food together. Jake, Vetri, Saad, and Anne, thank you for sharing my interest in organizing, cities, politics, and getting mad together about them.

My parents, Brinda and Vijesh, my sister Trisha, my grandparents, Saroj and Bhupendra, my uncle Tarang. Your influence on me is beyond compact description, but I will attempt to summarize it as approaching each of your relationships with care, and the world with curiosity.

Throughout grad school, the (great-)aunts, (great-)uncles, and cousins who make up my family have consistently checked in on me and shared their belief and support throughout. Having a family that is simultaneously big, diverse, and close is one of my life's great privileges.

I would like to specifically acknowledge Chris M, Rohit, Trisha, and my parents, who dedicated significant time to physically and emotionally supporting me when I ruptured my Achilles tendon two months before my qualification exams were scheduled, and in the long months of recovery post-surgery. Trisha slept in our living room for two weeks, right before a cross country move, to look after me. When she left, my parents took her place for another two weeks. Chris and Rohit picked up groceries and largely cooked for me for a month after they left, when I was on crutches and later in a boot. Chris took me to medical appointments when I couldn't walk and taught me a little guitar when I couldn't have any outdoor hobbies. Without this physical support I certainly would have paused

my PhD studies, and without the emotional support of you and my broader community, I quite likely would have left early. I'm endlessly thankful for the sacrifices you each made.

## **Dedication**

This dissertation is dedicated to my parents, Brinda and Vijesh, my sister Trisha, my grandparents Saroj and Bhupendra, and my uncle Tarang. I feel incredibly lucky to have been raised by each of you, I've carried your influences everywhere I have been and forever will.

## Table of Contents

ABSTRACT	3
Acknowledgements	5
Dedication	9
Table of Contents	10
List of Tables	14
List of Figures	15
Chapter 1. The Energy Transition and Computational Materials Science	19
Chapter 2. Background: Computational Approaches to Materials Defects and their Application to Energy Materials	22
2.1. Atomistic Modeling	22
2.1.1. First Principles Calculations and High-Throughput Databases	22
2.1.2. Interatomic Potentials and Machine Learning	24
2.2. Planar and Point Defects	26
2.3. Atomic Disorder	31
Chapter 3. Predicting Interfacial Structure by Adapting the Minima Hopping Method	34

	11
3.1. Introduction	34
3.2. Methods and Computational Details	37
3.2.1. Biasing the Minima Hopping Search Towards Conserving Interfacial Structures	37
3.2.2. Interfacial MHM with the Buckingham Potential	40
3.2.3. Density Functional Theory and First Principles Thermodynamics	41
3.3. Results and Discussions	44
3.3.1. SrTiO <sub>3</sub> Σ3 (111)	45
3.3.2. SrTiO <sub>3</sub> Σ3 (112)	49
3.4. Conclusion	51
Chapter 4. Cation Disorder and Oxygen Redox in Li <sub>3</sub> MO <sub>4</sub> Cathodes	53
4.1. Introduction, Background, and Crystal Structure	53
4.2. Methods	57
4.3. Investigation of Li <sub>3</sub> IrO <sub>4</sub> , Results and Discussion	58
4.3.1. Cation ordering in disordered Li <sub>3</sub> IrO <sub>4</sub> layer	58
4.3.2. Thermodynamics of Delithiation and Lithiation of Ordered and Disordered Li <sub>3</sub> IrO <sub>4</sub> Phases	61
4.3.3. Calculation of OCV	68
4.3.4. Signs of Anionic Redox and the Role of Cation Disorder	70
4.4. High Throughput Screening of Li <sub>3</sub> MO <sub>4</sub> Cathodes	78
4.5. Conclusion	81

Chapter 5. Phase Transformations and Defects in Zr-H using First-Principles and Machine Learning Interatomic Potentials	83
5.1. Introduction	83
5.2. Methods	88
5.2.1. Density Functional Theory Calculations	88
5.2.2. Active Learning of Moment Tensor Potentials and Description of Training Sets	89
5.2.3. Suppression of lost atoms during high temperature molecular dynamics	94
5.3. Results: Bulk and Vibrational Properties, and Phase Transformations in Zr-H	96
5.3.1. Comparison of calculated bulk properties between DFT and trained MTP	97
5.3.1.1. Lattice and elastic constants of bulk phases	97
5.3.1.2. 0 K Energetics of Bulk Phases	97
5.3.2. Vibrational Properties and Finite Temperature Thermodynamics	103
5.3.3. Calculation of Solvus Boundary and Applicability of MTP	107
5.3.4. Phase Transformation of $\epsilon$ -ZrH <sub>2</sub> to $\delta$ -ZrH <sub>2-x</sub>	108
5.4. Results: Validation of Zr-ZrH <sub>x</sub> MTP for Defects Thermodynamics and Migration	115
5.4.1. H-Vacancy ordering on fcc-Zr lattice	115
5.4.2. Migration of H in $\alpha$ -Zr and $\delta$ -ZrH <sub>2-x</sub>	117
5.4.3. Modeling of Defects in Zr	125
5.5. Discussion	129

	13
5.6. Conclusion	130
Chapter 6. Summary and Outlook	132
References	134
Vita	153

## List of Tables

3.1	Interfacial energy as calculated using the Buckingham potential and DFT, for structures found by the MHM, the GA, and AIRSS algorithms for structures deficient of a single SrO unit.	47
4.1	Enumerated $\text{Li}_3\text{IrO}_4$ structures, with their stability as calculated by electrostatics and DFT. Also included is structural information and the coordination of O	63
5.1	Summary of training information for the MTP presented in this work.	95
5.2	Comparison of equilibrium lattice parameters and elastic constants using DFT, the trained MTP, literature, and experiment.	98
5.3	Fit of H diffusion constant and activation energy in $\delta\text{-ZrH}_{2-x}$ phases, as simulated with the trained MTP	125
5.4	Comparison of point and planar defects in $\alpha\text{-Zr}$ , as calculated by the trained MTP and DFT	127
5.5	Selection criteria when evaluating candidate trained MTP	130

## List of Figures

3.1	Schematic of two methods used to bias the search during interface structure prediction	40
3.2	Comparison of interfacial energies of structures found by various methods, calculated using DFT.	46
3.3	Potential energy surface between two closely related SrTiO <sub>3</sub> (111) grain boundaries deficient in TiO <sub>2</sub>	48
3.4	Comparison of interfacial energies, as calculated by CASTEP and VASP	50
4.1	Crystal structures of lithiated Li <sub>x</sub> IrO <sub>4</sub> phases	56
4.2	a) Formation energies predicted by the cluster expansion. b) Formation energies as calculated by DFT c) Effective cluster interaction of fitted cluster expansion, as a function of cluster diameter.	62
4.3	a) The low energy structure found via cluster expansion at the composition Li <sub>3</sub> IrO <sub>4</sub> , with C2/m symmetry b) the view of the mixed cation plane.	64
4.4	Comparison formation energy of binary oxides as calculated using the optB88-vdW functional and experiment	65

4.5	Convex hulls of formation energies during delithiation of ordered and disordered $\text{Li}_3\text{IrO}_4$	67
4.6	Open circuit voltage, for $\text{Li}_3\text{IrO}_4$ with ordered and disordered mixed cation layers, upon lithiation and delithiation	69
4.7	DoS of Ordered and Disordered $\text{Li}_3\text{IrO}_4$	71
4.8	Expected magnetization behavior of O and Ir ions during delithiation	72
4.9	Local magnetization of O and Ir ions during delithiation of ordered and disordered $\text{Li}_3\text{IrO}_4$ , and minimum O-O bond distance	74
4.10	projected Crystal Orbital Hamilton Populations of short O-O bonds formed during delithiation of disordered $\text{Li}_3\text{IrO}_4$	75
4.11	$\Delta E_v^O$ of $\text{Li}_3\text{IrO}_4$ and $\text{Li}_2\text{IrO}_4$ with ordered and disordered cations, parameterized by nearest neighbor coordination	76
4.12	$\Delta E_v^O$ of $\text{LiIrO}_4$ and $\text{IrO}_4$ with ordered and disordered cations, parameterized by nearest neighbor coordination	77
4.13	Thermodynamic stability of $\text{Li}_3\text{MO}_4$ and $\text{LiMO}_4$ candidates assessed during high throughput	80
4.14	Voltage along $\text{Li}_5\text{MO}_4$ to $\text{Li}_3\text{MO}_4$ to $\text{MO}_4$ , from high throughput	81
5.1	Structural schematic of Zr-H figures	85
5.2	Flowchart outlining process for training MTP with active learning and NPT-MD	90
5.3	H-H Pair interaction with and without repulsive ZBL	96

5.4	Convex Hull between Zr-ZrH <sub>2</sub> , containing conventional ordered phases and disordered structures	100
5.5	ZrH epitaxial Bain path	102
5.6	ZrH <sub>2</sub> epitaxial Bain path	103
5.7	Calculated vibrational properties of $\alpha$ -Zr, H interstitials, and hydride phases, using DFT and trained MTP.	105
5.8	Migration pathway of H between interstitials in $\alpha$ -Zr	106
5.9	Temperature dependence of free energy of hydrogen defects and $\gamma$ -ZrH phase, and calculated solvus boundary, with and without vibrational effects	109
5.10	Average lattice vectors for hydride stoichiometries ranging from ZrH <sub>1.6</sub> to ZrH <sub>2</sub> vs. the temperature set by the thermostat during molecular dynamics, showing phase transformation with fixed composition	112
5.11	Zr-Zr RDF as captured during MD, in the vicinity of $\epsilon$ -ZrH <sub>2</sub> to $\delta$ -ZrH <sub>2-x</sub> phase transformation	113
5.12	Temperature and compositional dependence of the phase boundary between $\epsilon$ and $\delta$ phases	114
5.13	Convex hull of structures used to fit H-Vac cluster expansion on fcc Zr lattice, as calculated under DFT and the trained MTP, and fitted ECI	116
5.14	Convex Hull of 147 ZrH <sub>x</sub> structures used to fit a cluster expansion, calculated under DFT and trained MTP	118

5.15	Comparison of formation energy of structures used to fit cluster expansion of H-vacancy in tetrahedral sites on fcc-Zr lattice, as calculated by DFT and the trained MTP	119
5.16	MTP vs DFT prediction error as a function of hydrogen composition of structures used to fit cluster expansion	120
5.17	Diffusivity of dilute H in $\alpha$ -Zr as calculated using our trained MTP, and compared with experimental measures	122
5.18	Diffusivity of H in $\delta$ -ZrH <sub>2-x</sub> as calculated using the trained MTP, compared with experimental measures.	124
5.19	Interfacial energy of $\alpha$ -Zr and $\gamma$ -ZrH	128

## CHAPTER 1

**The Energy Transition and Computational Materials Science**

Climate change is the great challenge facing society broadly in the 21st century, and one that requires coordination between actors with disparate economic means, interests, and histories. The exploitation of fossil fuels, on one hand, has increased atmospheric CO<sub>2</sub> from a pre-industrial baseline of 280 parts per million (ppm) to about 415 as of 2021 [44], and on the other, has undergirded an energy system that has been the bedrock for the rapid advancement of both lifespans and quality of life across the world. One of the key geopolitical dynamics that colors our response to climate change is that governments and individuals who have benefited the least from fossil fuel exploitation and have therefore emitted the least CO<sub>2</sub> are the most vulnerable to the negative effects of climate change, which require economic means and built physical infrastructure to weather. Front line communities and governments, including many regions with the fastest growing populations, must therefore rapidly develop economically, ideally with minimal exploitation of fossil fuels. Wealthy countries must transition their energy systems to be carbon-free as rapidly as possible, while maintaining quality of life. The Intergovernmental Panel on Climate Change (IPCC) refers to this urgently necessary process as climate resilient development [63]. This energy transition will require new raw industrial inputs, such as cobalt and lithium for batteries. Many of these inputs will be sourced from developing economies such as the Democratic Republic of Congo [138] and Bolivia [129], opening

new frontiers for both economic development where it is needed, and the potential for exploitation.

Materials science & engineering offers a powerful toolbox in addressing these fundamental tensions between the need to decarbonize the economy sector while supporting development of emerging economies. Ideally, materials science can assist us in both improving the efficiency of existing technologies, reducing the raw inputs needed for technologies in the present day, while also enabling the deployment of new technologies that can decarbonize intensive industries.

At the heart of materials science is the concept that materials processing influences atomic structure, which in turn governs materials properties. Atomistic computational simulations allow materials scientists to finely study the relationship between structure and materials properties, while also giving insight in how materials processing may impact structure. The rapid expansion of computational power at the disposal of materials theorists has presented new opportunities over the last couple decades. First, materials theorists may increase theoretical complexity at the cost of increased computational cost in order to capture phenomena such as correlated electrons more accurately. Second, we may treat many more systems at a fixed level of theory, enabling high-throughput (HT) studies. Finally, we may treat larger system sizes, more accurately treating complex phenomena such as point and planar defects or atomistic disorder. While I have explored all of these directions during my PhD., the bulk of the work I have led has followed the third route.

We will begin this dissertation with a brief discussion of the approaches computational materials scientists use to model defects in materials, and their application to energy

materials. Then, this dissertation will explore three projects that I have led during my PhD. First we adapt the Minima Hopping Method, a structural search method often used for molecules, clusters, and crystal structures, for interfacial structure, exploring how the combination of point and planar defects lead to a difficult structural optimization problem. Then, we will consider study the role of cation disorder in facilitating anionic redox in  $\text{Li}_3\text{MO}_4$  type layered cathode materials. In the last project we cover, we developed a novel machine learning interatomic potential (MLP) to model the Zr-H binary system. Using this potential, we investigate the role of H defects in  $\alpha$ -Zr in mediating a phase transformation at the solvus boundary, as well as the role of disorder in the  $\epsilon$ -ZrH<sub>2</sub> to  $\delta$ -ZrH<sub>2-x</sub> phase transformation. We then evaluate the ability for this potential to capture other defect behavior relevant to the Zr-H system. Finally, we summarize the work covered in this dissertation, and offer an outlook on related work that might build off our results.

## CHAPTER 2

# **Background: Computational Approaches to Materials Defects and their Application to Energy Materials**

In this chapter, we will provide a brief background of how computational materials science can be leveraged to study materials defects, and its particular application to energy materials. We aim to provide useful background and context for the work carried out in later chapters, as well as a stand-alone document that can serve as a useful introduction to new researchers in the field. Energy materials form a vast category, ranging from battery materials including electrodes and electrolytes, thermoelectrics, catalysts, and high temperature structural metals used to withstand harsh conditions during energy production. Atomistic methods allow for fine control in the study of structure-property relationships, making it a toolbox with a wide variety of applications for energy materials.

### **2.1. Atomistic Modeling**

#### **2.1.1. First Principles Calculations and High-Throughput Databases**

As the name suggests, atomistic modeling approaches the task of predicting the behavior of materials based on the interactions of the constituent atoms. For solids, which we will be primarily treating in this dissertation, these calculations are facilitated by the application of periodic boundary conditions, which allow for infinite systems to be captured in finite simulation cells. First principles methods approach the problem by solving for

the electronic structure of a group of atoms, using various approximations to make the problem computationally tractable. The choice of approximation presents an accuracy-efficiency trade-off. When the level of accuracy is chosen appropriately, these methods can capture both thermodynamic aspects of a materials system and electronic behavior capably [99]. Density Functional Theory (DFT) sits at a favorable point on this accuracy-efficiency landscape, allowing for the calculation of 100s of atoms in a single simulation cell, and has become a workhorse for computational scientists in a variety of fields. DFT is built on the two theorems of Hohenberg and Kohn [56]. The first proves that the external potential  $v_{ext}(\mathbf{r})$  acting on  $N$  electrons uniquely determines the ground state electron density  $\rho(\mathbf{r})$ . Within the Born-Oppenheimer approximation, in which electrons are treated as dynamic and the much more massive nuclei as fixed,  $v_{ext}(\mathbf{r})$  corresponds to the potential supplied by the charge of the atomic nuclei. This simplifies the problem of solving for the the  $3N$ -dimensional system of interacting electrons, to treating the 3-dimensional electron density. The second theorem proves that there is a universal functional of the energy,  $F[\rho(\mathbf{r})]$ , which is minimized by the exact ground state. Kohn and Sham built upon this by introducing a Schrödinger-like equation:

$$(2.1) \quad \left[ -\frac{\hbar}{2m_e} \nabla^2 + v_{ext}(\mathbf{r}) + e^2 \int \frac{\rho(\mathbf{r}')}{|\mathbf{r}' - \mathbf{r}|} d\mathbf{r}' + v_{XC}(\mathbf{r}) \right] \psi(\mathbf{r}) = \epsilon_i \psi_i(\mathbf{r})$$

Here, the first term in brackets is the kinetic energy (where  $\hbar$  and  $m_e$  are respectively the reduced Planck constant, the third corresponds to the Coulomb repulsion between the electrons (often called the Hartree term), and  $v_{XC}$  is the exchange-correlation (XC) interaction. At its simplest, the XC can be approximated as being a local functional of simply the charge density, as within the Local Density Approximation (LDA), or the

charge density and its gradient, as within the Generalized Gradient Approximation (GGA) [119]. Though many DFT packages exist, throughout this work we will use the Vienna Ab-Initio Simulation Package (VASP) [83, 84, 81, 82].

GGA, in combination with the the rotationally invariant approach developed by Dudarev (DFT+U) [33] used to treat the self interaction error, have become the foundation for many computational studies, including those used to populate high-throughput databases, including the Open Quantum Materials Database (OQMD) [127], Materials Project (MP)[69], and AFLOWLIB.org [25, 26]. These databases are primarily composed of bulk calculations, which have been leveraged for countless studies of energy materials. For example, the OQMD has been used for several studies related to batteries, including to search for HF scavenging coatings and for potential cathode materials [6]. The OQMD has also been used to search for promising novel thermoelectric materials with ultralow lattice thermal conductivity [53]. MP has also been leveraged for several energy material studies, including a study of the relationship between voltage and safety by considering O<sub>2</sub> release [68]. While it is often beneficial to go beyond the GGA when studying energy materials with significant electron correlation, including meta-GGAs or approaches that capture dynamical correlations such as Dynamical Mean Field Theory (DMFT) [64], the bulk of the work presented in this dissertation will be carried out at the level of DFT+U.

### 2.1.2. Interatomic Potentials and Machine Learning

Interatomic potentials are much less computationally intensive to evaluate than first principles methods, because they bypass the need to explicitly calculate electronic structure,

and instead rely on energy and forces calculated from geometric relationships. The functional form of these interatomic potentials are usually motivated by physical intuition. A simple example is the modified Buckingham potential [13], which defines the pair interaction energy between two atoms,  $i$  and  $j$ , as:

$$(2.2) \quad U_{ij} = A \exp \frac{-r_{ij}}{\rho} - \frac{C_6}{r_{ij}^6} + \frac{q_i q_j}{r_{ij}}$$

Here,  $A$ ,  $\rho$ , and  $C_6$  are fitting parameters, while  $r_{ij}$  is the interatomic distance between  $i$  and  $j$ , and  $q$  is their charge. On the right hand side, the first two terms constitute the Buckingham interaction; the first exponential term describes a short range repulsive term between pairs of ions, the second is a longer-range van der Waals attractive interaction between ions. The final term describes the Coulomb interaction between a pair of ions. At the other end of the complexity spectrum are potentials such as the second nearest neighbor modified embedded atom method + charge equilibration (2NN MEAM + QEq) potentials, which have proved useful when studying complicated battery cathode phases [88].

These interatomic potentials can often successfully reproduce the mechanical properties of a single phase, but their rigidity means they struggle with capturing the interaction of multiple phases. Machine Learning Interatomic Potentials (MLP) are a class of potentials that seek to gain both further flexibility and accuracy, by eschewing rigid functional forms and the introducing clever local descriptors and representations of interactions. We include a discussion of the different forms of MLP and in section 5.1, and Deringer has written a nice overview of some of the early work in modeling battery materials using MLP [28], in particular highlighting their use in modeling Li diffusion in complicated

liquid and solid electrolytes, which are very difficult to model with DFT due to disorder and structure size. We use a Buckingham potential to guide interfacial structure search in Chapter 3, and train a Moment Tensor Potential, a class of MLP, to model Zr-H phase transformations and defects in Chapter 5.

## 2.2. Planar and Point Defects

We will begin this section by discussing how point and planar defects are modeled, as they share a similar mathematical and conceptual frameworks, and will then discuss their application to energy materials. We will make some simplifying assumptions. In general, when calculating a defect formation energy, a surface energy, or interfacial energy, we would like to consider the Gibbs free energy  $\Delta G_f$ , which accounts for finite temperature effects. For now, we will assume that the calculated internal energy,  $E_{DFT}$  at 0K is a suitable approximation. For the calculation of a point and planar defect, we generally follow a supercell approach, in which a large structure is created to incorporate the desired defect, with the size sufficient such that the periodic images of the defect do not interact and can be considered isolated.

For a point defect  $x$  with a charge  $q$ , such as an interstitial, vacancy, or substitutional atom, we can calculate a defect formation energy  $\Delta E_{x,f}$

$$(2.3) \quad \Delta E_{x,f} = E_{x,tot} - E_{bulk,tot} - \sum_i (n_i \mu_i) + (q * E_F)$$

The above equation gives the formation energy per defect (or defect complex) considered. Here,  $E_{x,tot}$  is the calculated internal energy of a supercell incorporating a defect  $x$ ,  $E_{bulk,tot}$  is the energy of the reference bulk phase sans defect,  $n_i$  is the number of atoms

of species  $i$  added or removed to incorporate the defect vs. bulk, and  $\mu_i$  is its respective chemical potential. For a charged defect, we must also consider the chemical potential of the electron added or removed to incorporate the defect, equivalent to the Fermi level  $E_F$ , which gives rise to the final term. We note that the study of charged defects introduces an electrostatic potential that emanates throughout the cell, which greatly increases [86, 43]. There have been useful packages developed to automate parts of the defect calculation workflow, such as PyCDT [19].

Planar (2D) defects - surfaces, grain boundaries, and heterointerfaces - break the symmetry of the constituent bulk phase(s) in 1 dimension. Surfaces are created by cleaving a supercell of the bulk phase along a specific plane (defined by the Miller indices), leaving two identical surfaces in contact with vacuum. The free energy of a surface  $\gamma$  can be calculated as:

$$(2.4) \quad \gamma = \frac{E_{tot,slab} - E_{tot,bulk} - \sum_i (n_i \mu_i)}{2A}$$

Here,  $E_{tot,slab}$  is the total energy of the surface slab, while  $E_{tot,bulk}$  is the reference bulk phase of the corresponding size. The term  $2A$  arises from the fact that the total surface energy is an extensive quantity which scales with the area of the surface ( $A$ ), with the 2 arising from the 2 surfaces created by cleaving the bulk structure due to periodic boundary conditions.  $n_i$  is the number of atoms of species  $i$ , and  $\mu_i$  is their chemical potential, which are needed to account for deviations from the ideal stoichiometry. These deviations from ideal stoichiometry may simply be the result of how planes of atoms are removed when a bulk structure is cleaved to form a surface slab. In the simple case of rock-salt NaCl, cleaving along either the (110) or (100) plane leaves will result in a charge neutral surface

plane, in which each plane is identical, with  $\text{Na}^+$  ions balanced by  $\text{Cl}^-$ . However, creating a (111) surface gives rise to alternating planes of pure  $\text{Na}^+$  and  $\text{Cl}^-$ , giving rise to polar surfaces [87]. Thus, the requirement of 2 identical surfaces will lead to an excess of Na or Cl, which must be accounted for by considering the excess  $n_i$ . The breaking of symmetry at the surface also means that it may be energetically favorable to form planes that are different than what forms in the bulk, which are known as *surface reconstructions*. Surface reconstructions will too often lead to non-stoichiometric surfaces.

Finally, we will discuss the calculation of interfacial structure. The construction of interface structures requires the cleaving and reorientation of bulk structures along desired planes, which, in the case of hetero-interfaces, must then be strained off their equilibrium lattice parameters such that the two slabs can be matched. This introduces a coherency strain,  $\delta E_{cs}$ . When calculating an the formation energy of an interfacial structure,  $\Delta E_{f,int}$ , we assume that we can decompose this energy into  $\delta E_{cs}$  and a term that is proportional to the interfacial energy  $\sigma$ . For the sake of simplicity, we will assume that the interface cell does not contain vacuum, and instead contains two identical interfaces.

$$(2.5) \quad \Delta E_{f,int} = E_{tot,int} - E_{tot,bulk} - \sum_i (n_i \mu_i) = \delta E_{cs} * N + 2\sigma A$$

Here,  $\Delta E_{f,int}$  is the formation energy of the interfacial structure,  $E_{tot,int}$  is the calculated total energy of the interface cell,  $E_{tot,bulk}$  is the reference energy of the two bulk phases, and  $\sum_i (n_i \mu_i)$  once again accounts for the penalty of off-stoichiometry.  $\delta E_{cs}$  is the coherency strain per atom,  $N$  is the total number of atoms in the structure,  $\sigma$  is the interfacial energy, and  $A$  is the area of the interface. The coherency strain can be directly calculated, by

calculating the energy cost of straining the bulk phases to the shared lattice parameter [168], or by calculating a series of similar super cells, and applying a linear fit to back out  $\delta E_{cs}$  [73]. Analogously to ensuring periodic images of point defects are sufficiently isolated by unperturbed bulk, interface and surface structures should be thick enough (and have enough vacuum) such that the two planar defects do not interact.

We will now turn our attention to a brief discussion of the determination of  $\mu_i$ , which applies to the discussion of both point and planar defects. Fundamentally,  $\mu_i$  is the change in free energy when a unit of particle i is removed:

$$(2.6) \quad \mu_i = \frac{\partial G}{\partial n_{i,T,P}}$$

It thus represents the change in energy when a particle is taken from or given to a reservoir. The determination of  $\mu_i$  requires identifying the relevant phases which are acting as a reservoir, and finding the  $\mu_i$  which stabilize the coexistence of these phases. This involves solving a system of equations in which  $\mu_i$  are unknown and the total energy of a set of phases have been calculated. As a simple example, consider the coexistence of an elemental phase A with a binary compound  $AB_2$ . We can define the chemical potential as such:

$$(2.7) \quad \begin{aligned} \mu_A &= E_A \\ \mu_A + 2\mu_B &= E_{AB_2} \end{aligned}$$

Here,  $E_x$  refers to the total energy of a phase x per formula unit. One of these phases will generally be the structure hosting the defect or forming the surface (and in the case of heterointerfaces, you might supply two phases like this), however the other possible

phases may not be so obvious. One choice might be to consider possible coexistence regions around the phase of interest, ie for a ternary system, all of the three phase regions surrounding the phase of interest in the phase diagram, and using these phases to bound the range of the chemical potentials. The chemical potential may also be used to predict finite temperature behavior, for example, in the case of a gaseous  $O_2$  reference. Thus, a careful study of what defect structures are predicted to arise at a given set of chemical potentials can help guide experimental processing conditions.

The study of point defects has a wide applicability in energy materials. For instance, in thin-film photovoltaics, defects levels must be carefully engineered to allow for shallow donor and acceptor states in the band structure to form p-n junctions, while also limiting the carrier trapping [117]. In thermoelectrics, the introduction of a low concentration of Na and Sb point defects in a host of PbSe has been shown to result in a very low lattice thermal conductivity due to strong phonon scattering, leading to  $zT$  (the thermoelectric figure of merit) values that are about 20% higher than the defect free PbSe [140]. Calculation of oxygen point defects has been used to screen perovskite  $ABO_3$  compounds in high-throughput for applicability for thermochemical water splitting. [35].

Surfaces and interfaces also provide a rich design space for engineering energy materials. The careful consideration of various  $LiMn_2O_4$  battery cathode surface reconstructions and their stability against varying chemical potentials can guide experimental processing conditions to suppress manganese dissolution[163, 75]. Surface and interface calculations can also be used to predict charge transfer and the formation of space-charge layers at electrode-electrolyte interfaces in solid-state batteries,. [144, 164, 143]. The structure

of polyelemental nanoparticles can be predicted by the incorporation of interface and surface energies [21]; this approach can also be used to predict the formation of high-index surfaces useful in catalysis [61]. Grain boundaries in thermoelectrics have also proven a fruitful design space due to their ability to scatter phonons and drive down thermal conductivity [182].

In this dissertation, we will discuss the search for interfacial reconstructions in non-stoichiometric  $\text{SrTiO}_3$  grain boundaries in Chapter 3, point defects of Li and O in  $\text{Li}_x\text{MO}_4$  cathodes. Point defects are especially important in the work of the Zr-H binary system presented in Chapter 5, as their thermodynamics contribute to the solvus boundary between  $\alpha - \text{Zr}$  and the formation of hydride phases.

### 2.3. Atomic Disorder

Related to the idea of point defects is the concept of structural disorder. In the extreme case are amorphous phases which lack any long range order, we will instead discuss in this section the concept of disorder on fixed lattice sites, a phenomenon commonly found when studying alloys. These systems prove challenging to model by straight-forward atomistic modeling, as the presence of disorder eludes the use of a single compact unit cell with periodic boundaries. In particular, we would like to use Monte Carlo to sample many large configurations to estimate configurational entropy, but this would prove to be intractable if all calculations were carried out at the level of first principles. Two powerful tools atomistic modelers have for addressing atomic disorder are cluster expansion and special quasirandom structures (SQS), both of which have been successfully used beyond their initial use in modeling metal alloys. Both cluster expansion and SQS rest on the idea

of representing structures by their constituent *clusters*. We'll first consider the cluster expansion formalism, which is a generalized Ising model. In the simple Ising model for spin systems, interaction terms up to the nearest neighbor pair are considered before truncation; we call this nearest neighbor pair interaction term  $J_{2,1}$ , the 2 signifying a pair interaction and 1 signifying the nearest neighbor. In the generalized Ising model, we build of a model for the energy per lattice site based on further interaction terms:

$$(2.8) \quad E(\boldsymbol{\sigma}) = E_{ce}(\boldsymbol{\sigma}) = \sum_f J_f \Pi_f(\boldsymbol{\sigma})$$

Here,  $\boldsymbol{\sigma}$  is a vector indicating the species of occupying each mixing site, and can be used to define a single finite structure. When considering the simple case of binary mixing (as we do in this dissertation), in which two distinct species share a single fixed lattice site, we assign a spin variable,  $\sigma_i = \pm 1$ .  $f$  are the distinct, non-equivalent clusters which can be formed from each lattice site, including pair, triplet, quadruplet clusters, and further.  $\Pi_f \boldsymbol{\sigma}$  are the correlations, and are the averaged spin-products for each type distinct cluster type for a structure represented by  $\boldsymbol{\sigma}$ . For example, if we imagine a simple 2D grid of alternating spins (in which each site's nearest neighbor in each direction is the opposite spin), the averaged spin-product for the nearest neighbor pair cluster is  $1 * -1 = -1$ . We could continue to define the correlation matrix by considering more clusters of increasing complexity and separation (in addition to the point clusters), for the structures of interest. Thus, the challenge of fitting a cluster expansion becomes supplying enough training examples to fit the Effective Cluster Interaction (ECI) terms,  $J_f$ , for each type of cluster, by minimizing some measure of the error, such as the root mean square

error. We can guard against over-fitting by using cross validation.

$$(2.9) \quad CV = \left( \frac{1}{n} \sum_{i=1}^n (E_i^{DFT} - E_i^{CE})^2 \right)^{\frac{1}{2}}$$

Once  $J_f$  has been fitted, it can quickly be used to calculate the energy of structures, either to explore other ordered ground states, or as a Hamiltonian for Monte Carlo.

The goal when generating an SQS is to create a compact unit cell that most closely matches the correlation matrix for the disordered state, which can easily be calculated due to the independence of site occupations [183]. The SQS can thus be searched for through generating structures and evaluating the difference between  $\Pi_f(\boldsymbol{\sigma})$  and  $\Pi_f(\boldsymbol{\sigma}^{rnd})$ , either through enumeration of all possible structures under a given size, or a search guided by an optimization method such as Monte Carlo [157].

Atomistic disorder has a wide applicability in understanding and designing energy materials. For example, in battery cathodes, computational tools have been used to study the delithiation of  $\text{LiCoO}_2$  as a function of temperature [169], the design of core-shell particles for olivine  $\text{LiM}_{1-y}\text{M}_y\text{PO}_4$  [141], and have found further importance recently in the study of high capacity disordered-rocksalt materials [94, 37, 173]. In thermoelectrics, disorder has been used to introduce valley degeneracy in  $\text{CaZn}_2\text{Sb}_2$ - $\text{CaMg}_2\text{Sb}_2$  solid solutions for increased electrical conductivity [170]. We use cluster expansions and SQS in chapter 4 to model Li and Ir mixing in  $\text{Li}(\text{Li}_r)\text{O}_2$ , and in chapter 5 to model H-Vacancy disorder in tetrahedral interstices of an fcc Zr lattice.

## CHAPTER 3

## Predicting Interfacial Structure by Adapting the Minima Hopping Method

*This chapter is adapted from a publication in preparation for submission. Once accepted, permission will be requested*

### 3.1. Introduction

The microscopic structure of interfaces in multicomponent systems fundamentally influences the bulk performance of functional materials, and constitutes a critical factor in materials design. At the atomic scale, the presence of interfaces leads to the breaking of symmetry and the introduction of novel chemical bonding environments, leading to complex structure-property relationships that continue to be the subject of intense research. Interfaces in the form of grain boundaries in polycrystalline materials or heterointerfaces can greatly impact mechanical and electronic properties, as well as transport phenomena [8], which either lead to performance degradation or can be exploited to improve materials behavior [80]. Examples include a correlation between higher degrees of ordering at grain boundaries and improved flexural strength in  $\text{Al}_2\text{O}_3$  [40], the ability to tailor grain boundary structure and in turn grain boundary thermal transport via dopants in  $\beta$ -SiC for use as thermoelectrics [49], and similarly the tuning of grain boundary structure and electrical conductivity in Cu nanowires via dopants [20]. Interfaces between different phases introduce further complexity due to the relative alignment of electronic

bands, strongly impacting electronic behavior [27]. Negative effects of grain boundaries and hetero-interfaces are prominent in battery applications due to the salience of both electronic and ion transfer, as these interfaces are often the site of space-charge regions and can lead to sluggish charge transfer [95, 162].

The examples above demonstrate that a better understanding of the structure-property relationships of interfaces would advance defect engineering both when their presence is desired to improve materials performance, or when avoiding their formation leads to detrimental effects. Experimentally, high resolution transmission electron microscopy (HRTEM) is often used to study interfacial structure [36, 60, 171]. HRTEM results, however, are often difficult to interpret on their own in the vicinity of the interface, due to the breaking of symmetry and the role of hetero-interfaces and grain boundaries as sources and sinks of defects [59]. Therefore, numerical simulations are particularly powerful to complement experimental techniques with theoretical insight [128, 103]. Atomistic simulations of interfacial structures with *ab initio* or classical methods have become popular in the last decades, but they remain challenging due to the absence of bulk (translational) symmetry that lead to unexpected atomic reconstruction in the vicinity of the interface. Further, at heterointerfaces, differences in chemical potentials of elements between two phases can drive species across the interface, creating deviations from the bulk stoichiometry in the vicinity of the grain boundary which further lead to complexity in atomic structure.

To address this issue, several strategies have emerged to determine interfacial structures. Some attempts treat interface structure holistically, starting from the search for low-strain interface orientations and following through to structure optimization [145],

while others include experimental information [134]. In single phase systems, von Alfthan *et al.* studied ordering at  $\Sigma = 5$  (001) Si twist grain boundaries using a Tersoff potential by varying the number of atoms in the system and annealing using molecular dynamics (MD) simulations [159]. Tschopp *et al.* have extensively used a scheme of varying atomic density in the vicinity of the grain boundary, combined with rigid cell translations to study asymmetric tilt grain boundaries in Cu and Al [151, 152], later explicitly studying the role of vacancies and interstitials in  $\alpha$ -Fe through enumeration [153] followed by local relaxation.

Non-stoichiometric grain boundaries in multicomponent systems are particularly challenging for interfacial structure prediction, since the interfaces act as sources and sinks of defects. In particular, the  $\Sigma 3$  (111) and  $\Sigma 3(112)$  [110] grain boundaries in  $\text{SrTiO}_3$  have been the subject of multiple studies using atomistic simulations, and has meanwhile become a canonical problem and somewhat of a benchmark system for interfacial structure prediction algorithms. Chua *et al.* first used a genetic algorithm (GA) to find candidate structures with a Buckingham potential which were subsequently relaxed using DFT [24]. The foundation of this work was laid out in Ref. [13], which carefully compared the transferability of interatomic potentials in  $\text{SrTiO}_3$  for the study of grain boundaries. Later, the Ab-Initio Random Structure Search (AIRSS) approach was used to treat the (111) grain boundary [132], while an adaptive genetic algorithm (AGA), for which the embedded atom method (EAM) potential energy landscape was refit during the search, was used to treat the (112) grain boundary [178].

Here, we present an algorithm based on the minima hopping method (MHM) [2] to predict the atomistic structure of interfaces. In our approach, we drive the search towards

low-energy interface structures by efficiently sampling atomic configurations that are generated using bursts of short molecular dynamics simulation, where the initial atomic velocity are weighted with a spatially-resolved order parameter while preserving the grain boundary orientation. We apply our algorithm to study both (111) and (112) grain boundaries of SrTiO<sub>3</sub> and discover interface structures that are lower in energy than previous reports for selected system sizes.

### 3.2. Methods and Computational Details

#### 3.2.1. Biasing the Minima Hopping Search Towards Conserving Interfacial Structures

The minima hopping method (MHM) is a structural search method that aims at globally optimizing the potential energy of a system by using a sequence of short molecular dynamics trials to overcome kinetic barriers on the potential energy landscape followed by local structural relaxations [2, 4]. A sophisticated feedback mechanism on the kinetic energy of the escape trials based on the history of explored structures is employed to accelerate the search [180]. While the MHM was first developed to predict the structures of molecular systems [48, 9] it was later extended to study periodic systems [2], surface reconstructions [1, 42], high-pressure phases [3], protein folding [125], and to find chemical reaction pathways [131].

To adapt the MHM for interfacial structure prediction, we modify how the structures are generated in the algorithm by biasing the initial velocities of the MD escape trials. We first initialize the atomic velocities with randomized directions and magnitudes drawn from a Gaussian distribution, which are then rotated approximately along low-barrier

transitions by a process called softening [2]. Then, we employ one of two means to weight the velocities.

In the first method, which we call *distance order method* (DOM), we simply gradually scale the coefficient of the initial velocity to zero as the distance to the interface increases. Assuming that the interface normal is oriented along the  $z$ -axis of the simulation cell, we use a smooth weighting function, a Gaussian  $\mathcal{N}(c_z, \sigma)$  centered at the interface location  $c_z$ . Since our simulation cells employ periodic boundary conditions, two interfaces exist in one cell with their centers at  $c_z, j$ , where  $j \in \{1, 2\}$ . The velocity of each atom  $i$  at  $\vec{r}_i$  is then scaled based on the distance along the  $z$ -direction from both  $c_z, j$ , summing the contributions from the two interfaces.

In the second method, which we call *local order method* (LOM), we use an adaptive scheme to capture the local environment of each atom which serves as a scaling function. For this purpose, we use the atomic bond-orientational order parameter  $o_\alpha$ , which was first introduced to study the distribution of bond environments in liquids and glasses [142], and was later adapted for the study of grain boundaries in silicon [159], and implemented for interfacial structure prediction in SrTiO<sub>3</sub> [24]. Briefly, the order parameter is derived by comparing the local environment of each atom  $\alpha$  of species  $Z_\alpha$  in the structure with the local environment of atoms of the same species within a certain radius  $r$ , a set of atoms  $N_\alpha$  in the vicinity of  $\alpha$  around its position  $\vec{r}_\alpha$ . For each atom of species  $Z_\alpha$ , we define the following quantity, by summing over Laplace's spherical harmonics defined by its angular relationship with the atoms within its neighborhood:

$$(3.1) \quad q_l^m(\alpha) = \frac{1}{C_\alpha} \sum_{\beta \in N_\alpha} Y_l^m(\Theta_{\alpha\beta}, \phi_{\alpha\beta})$$

Here,  $\Theta_{\alpha\beta}$  and  $\phi_{\alpha\beta}$  are respectively the colatitude and azimuthal angle between  $\alpha$  and a single neighbor  $\beta$ , while  $C_\alpha$  is a normalization constant such that  $\langle q_l^m | q_l^m \rangle \stackrel{!}{=} 1$ . For each neighbor  $\beta$ , we define the similarity  $b_{\alpha\beta}$  as

$$(3.2) \quad b_{\alpha\beta} = \sum_{m=-l}^l q_l^m(\alpha) q_l^m(\beta)$$

$o_\alpha$  is then defined as the average over all  $b_{\alpha\beta}$  for which  $Z_\alpha = Z_\beta$ , and is zero if no neighbors exist of the same species. The absolute value of the order parameter will be between zero and one, where values closer to one correspond to a more ordered environment. Our final weighting function to scale the initial velocity is then  $1 - |o_\alpha|$ . For atoms in the bulk, where the environment is highly ordered, the escape trial velocities will be small, while near the interface they will not be substantially damped. For our investigation of SrTiO<sub>3</sub> we used a cutoff radius of  $\sigma = 1.1a_0$  to define the local environment of an atom, where  $a_0$  is the lattice constant of SrTiO<sub>3</sub>, 3.865 Å. This value of  $\sigma$  was empirically found to be appropriate for our MHM simulation.

Both methods described above are visualized in Fig. 3.1, which shows a schematic of two phases composed of the same two species forming an interface. While our benchmarks showed that both approaches work well to bias the MHM simulations towards sampling interfaces structures, we found that using the LOM is more efficient. Hence, for the results shown in the remainder of this work we use the LOM scheme to weight the initial velocities. In fact, the LOM approach is an elegant means for biasing the structural rearrangements to the interface without arbitrarily freezing regions within the structure, as the size of that region would need to be converged, and would not be able to adapt during the structural search. Note that in structures where a single species occupies multiple symmetrically

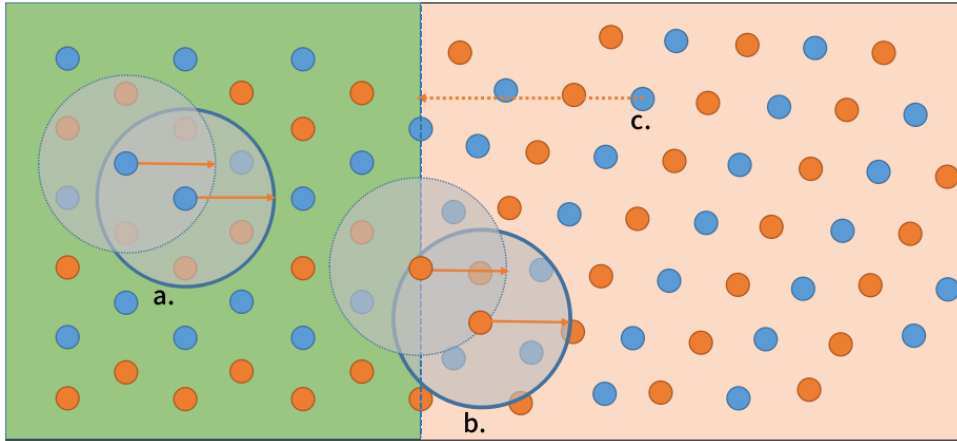


Figure 3.1. A schematic comparison of the two methods to bias the search towards new interface structures. The green (left) and cream (right) regions are distinct phases containing the same two atomic species, represented by orange and blue circles. The interface between the two phases is represented by the vertical dashed line. Points labeled a. and b. correspond to an ordered and disordered environment, respectively, showing the comparison of bond environment based on the LOM. Far from the interface, the two central blue atoms have identical environments (the dashed and solid circles around a. represent the identical environments), while in the vicinity of the interface there is a greater variety of bond environments and therefore higher disorder (the dashed and solid circles around b. have different environments). The horizontal dashed line connecting the atom at c. shows its distance to the interface, which can be used by a Gaussian decay function to bias the structural search with DOM: atoms farther away from the interface are initialized with lower kinetic energy in an MHM cycle.

distinct sites, the order parameter may classify crystalline regions as disordered. Hence, distinct Wyckoff sites of the same species have to be labeled independently.

### 3.2.2. Interfacial MHM with the Buckingham Potential

The MHM simulations were carried out on the empirical Buckingham potential energy landscape, as parametrized in Ref. [24], to facilitate comparison with the original GA approach by Chua et al. As in that work, we used the parameters from the Thomas

potential [148], with a cutoff of 20 Å and fifth order polynomial tapering between 18 and 20 Å following the work of Ref. [13]. The potential was implemented using the General Utility Lattice Program (GULP) [45, 46].

In the MHM runs, we use the Gaussian orbital method [180] with a cutoff radius of 8 Å in order to compare the atomic structures of the local minima. During the search, the cell vectors in the grain boundary plane were fixed to experimental values, while the lattice vector along the grain boundary normal was left unconstrained (along the  $z$ -direction). The local relaxations were considered converged when the maximal force components were less than 0.005 eV/Å.

The size of the initial grain boundary cell was determined from the theoretical lattice parameter of the cubic perovskite SrTiO<sub>3</sub>, which we fully relaxed using density functional theory (DFT) calculations (see Sec. 3.2.3 for details). As mentioned in Sec. 3.2.1, our simulation cells are constructed with two equivalent grain boundaries due to periodic boundary conditions, however they are not constrained to be equivalent during the structural search.

### 3.2.3. Density Functional Theory and First Principles Thermodynamics

Candidate structures found using the MHM are subsequently refined using DFT calculations within the projector augmented wave (PAW) formalism and the local density approximation (LDA) to the exchange-correlation functional, as implemented in the Vienna Ab-Initio Simulation Package (VASP)[83, 84, 81, 82]. A  $4 \times 4 \times 1$   $\Gamma$ -centered  $k$ -points mesh and a 520 eV plane-wave cutoff energy were used during these calculations, settings are similar to Refs. [24, 132]. For each stoichiometry, the 15 lowest energy structures

found with the MHM were considered during an initial coarse relaxation where we kept the in-plane lattice parameters fixed until the atomic forces were less than  $0.05 \text{ eV}/\text{\AA}$ . From this set, the 5 lowest energy structures were further relaxed with forces converged to  $0.005 \text{ eV}/\text{\AA}$ , using the FIRE algorithm [15] and no constraints on the lattice degrees of freedom.

In addition to the structures from the MHM runs, we also re-relaxed the ones found by the GA [24] and AIRSS [132] with the same workflow in order to facilitate comparison. Since those previous works used ultrasoft pseudopotentials with the CASTEP DFT code, we also show a comparison of their calculated interfacial energies with those found using our settings in Fig. 3.4.

We employ the same thermodynamic analysis scheme presented in Refs. [24, 132, 178] by treating  $\text{SrTiO}_3$  as a pseudobinary system of SrO and  $\text{TiO}_2$ , facilitating the comparison between non-stoichiometric grain boundaries with varying chemical potentials. The full treatment of this approach is shown in Ref. [71]. For a given structure, we define the interfacial free energy  $\sigma$  as

$$(3.3) \quad \sigma = \frac{1}{2A}(G - N_{\text{SrO}}\mu_{\text{SrO}} - N_{\text{TiO}_2}\mu_{\text{TiO}_2})$$

We estimate the Gibbs Free Energy  $G$  with the DFT total energy, while  $N$  is the number of formula units for the given binary in the structure. We use DFT total energies corresponding to the cubic perovskite  $\text{SrTiO}_3$  phase, the rocksalt SrO phase, and rutile  $\text{TiO}_2$  as reference values. We bound the values of the chemical potential by relating them to

the formation energy of SrTiO<sub>3</sub>:

$$(3.4) \quad \Delta G_{f,\text{SrTiO}_3}^0 = g_{\text{SrTiO}_3}^0 - g_{\text{SrO}}^0 - g_{\text{TiO}_2}^0$$

$$(3.5) \quad \mu_{\text{SrO}} + \mu_{\text{TiO}_2} = g_{\text{SrTiO}_3}^0$$

This is necessary for SrTiO<sub>3</sub> to be in equilibrium. By combining above equations we arrive at:

$$(3.6) \quad \Delta G_{f,\text{SrTiO}_3}^0 = \mu_{\text{SrO}} - g_{\text{SrO}}^0 + \mu_{\text{TiO}_2} - g_{\text{TiO}_2}^0$$

If  $\mu_{\text{TiO}_2} > g_{\text{TiO}_2}^0$ , TiO<sub>2</sub> would precipitate out of the interface (likewise for SrO), so we know the opposite must be true,  $\mu_{\text{TiO}_2} \leq g_{\text{TiO}_2}^0$ . Rearranging yields:

$$(3.7) \quad \Delta G_{f,\text{SrTiO}_3}^0 - (\mu_{\text{SrO}} - g_{\text{SrO}}^0) + g_{\text{TiO}_2}^0 = \mu_{\text{TiO}_2} \leq g_{\text{TiO}_2}^0$$

Now, consider:

$$(3.8) \quad \Delta G_{f,\text{SrTiO}_3}^0 \leq \mu_{\text{SrO}} - g_{\text{SrO}}^0 \leq 0$$

The left hand inequality becomes an equality (i.e., the middle expression reaches its minimum) when  $\mu_{\text{TiO}_2} = g_{\text{TiO}_2}^0$ . The right hand inequality becomes an equality (i.e., the middle term reaches its maximum) when  $\mu_{\text{SrO}} = g_{\text{SrO}}^0$ . Using these bounds on the term  $-(\mu_{\text{SrO}} - g_{\text{SrO}}^0)$  and introducing  $0 \leq \lambda \leq 1$ .

$$(3.9) \quad \mu_{\text{TiO}_2} = g_{\text{TiO}_2}^0 + \lambda \Delta G_{f,\text{SrTiO}_3}^0$$

Similarly

$$(3.10) \quad \mu_{\text{SrO}} = g_{\text{SrO}}^0 + (1 - \lambda)\Delta G_{f,\text{SrTiO}_3}^0$$

This formalism allows us to compare the stability of interfaces across stoichiometries with added or removed  $\text{TiO}_2$  or  $\text{SrO}$  units.

### 3.3. Results and Discussions

We employ our interfacial MHM framework to study the  $\Sigma 3$  (111) and  $\Sigma 3(112)$  [110] grain boundaries of  $\text{SrTiO}_3$ . Following the procedure of Ref. [24, 132], we fix the total system size such that the stoichiometric grain boundary supercells contain 120 total atoms, and off-stoichiometric boundaries are deficient of  $\text{TiO}_2$  and  $\text{SrO}$  units. We first verify that MHM is able to recover the  $\text{SrO}_3$ -terminated stoichiometric (111) grain boundary and the  $\text{SrTiO}$ -terminated stoichiometric (112) grain boundary, by initializing the search with a randomized configuration in the vicinity of the grain boundary (within three atomic planes of the interface in either direction).

Next, we search for non-stoichiometric (111) and (112) grain boundaries while considering systems that incorporate charge-neutral vacancies. Interfacial energies are shown in Fig. 3.2, both for structures found in this work and structures found in previous studies. As in Refs. [24, 132, 178], we do not include vacuum in our structural models, so there are two interfaces present in each simulation cell (see also Sec. 3.2 for details). Note that our comparisons with structures from the literature are based on Refs. [24, 132] for the (111) grain boundary, and Refs. [24, 178] for the (112) grain boundary.

### 3.3.1. SrTiO<sub>3</sub>Σ3 (111)

First we discuss the (111) grain boundaries, for which our MHM simulations discovered more stable grain structures than previous efforts using the GA and AIRSS. For both the TiO<sub>2</sub> and SrO deficient grain boundaries, we recover structures that are about 0.17 J/m<sup>2</sup> lower in energy than best structures previously found by AIRSS.

To compare our results and the performance of our method to earlier reports in the literature we first have to bring all calculations onto the same footing, which is not straightforward. For example, our work and Ref. [24] both use a hybrid approach, using classical interatomic potentials for the structural search (the empirical Buckingham potential) and refining the top candidate configurations with *ab-initio* DFT. On the other hand, Ref. [132] perform the structural search directly at the level of DFT.

Further, the energetic ordering of interfacial structures with the Buckingham potential does not necessarily correspond to the ordering with DFT. As an example, we show a comparison of structures deficient of a SrO in Table 3.1, where we list the energies computed with the Buckingham potential and DFT for configurations found by the MHM, GA, and AIRSS. For both grain boundaries SrTiO<sub>3</sub> (111) and (112), no structure found by Refs. [24, 132] relaxed to a lower energy with the Buckingham potential than the minimum found during our structural search. However, we note that the structure that is the lowest energy with the Buckingham potential is only the fourth most stable with DFT. Hence, although the MHM performs well in identifying the low-lying portion of the PES, the refinement of a range of low-energy candidate structure with DFT is crucial [47]. To circumvent this issue the structural search itself can be performed at the DFT level,

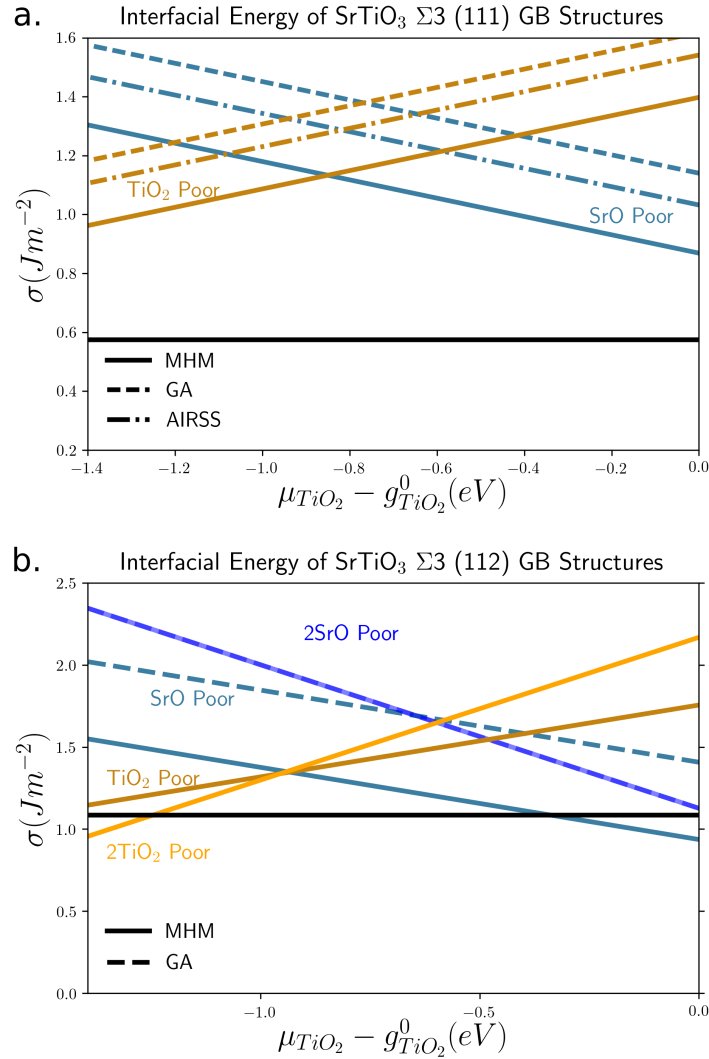


Figure 3.2. Comparison of interfacial energies of structures found by various methods, with a varying chemical potential range: the far right of the chemical potential range corresponds to SrTiO<sub>3</sub> in equilibrium with TiO<sub>2</sub>, and the far left corresponds to SrTiO<sub>3</sub> in equilibrium with SrO (see Sec. 3.2.3 for extended discussions). Different line colors correspond to varying stoichiometry, while different line styles correspond to different structure prediction algorithms employed. Panel a. shows the thermodynamics of SrTiO<sub>3</sub> grain boundaries with a (111) grain boundary (GB) plane. All approaches are able to recover the stoichiometric GB shown in solid black, but MHM is able to find more stable off-stoichiometric GB. b. shows the same for (112) grain boundary structures.

Table 3.1. Interfacial energy as calculated using the Buckingham potential and DFT, for structures found by the MHM, the GA [24], and AIRSS [132] algorithms (first column), for structures deficient of a single SrO unit. The top and bottom part correspond to SrTiO<sub>3</sub> (STO) (111) and SrTiO<sub>3</sub> (112), respectively. Column 2 shows the 5 most stable interfacial structures found during the MHM searches with the Buckingham potential. The corresponding DFT energies after a local relaxation are shown in column 4. Since GA and AIRSS structures were reported as DFT minima, we re-relaxed all DFT structures with the Buckingham potential (column 3). The reported GA and AIRSS structures are not more stable with DFT or the Buckingham potential than the lowest energy structures found by MHM. The chemical potentials  $\mu_{\text{TiO}_2}$  and  $\mu_{\text{SrO}}$  are chosen to minimize the reported interfacial energy, i.e., the condition  $\mu_{\text{TiO}_2} = g_{\text{TiO}_2}^0$ . The lowest energy values are in boldface.

	$\sigma_{\text{Buck}}$ (J/m <sup>2</sup> )		$\sigma_{\text{DFT}}$ (J/m <sup>2</sup> )
	From MHM	Relax from DFT min	DFT min
<hr/> <hr/> STO (111) <hr/>			
AIRSS		2.050	1.019
GA		2.058	1.119
MHM	<b>1.840</b>	<b>1.840</b>	0.969
	1.847	1.847	<b>0.851</b>
	1.901	1.901	0.913
	1.909	1.884	0.928
	1.915	1.915	0.961
<hr/> <hr/> STO (112) <hr/>			
GA		2.431	1.407
MHM	<b>1.809</b>	2.279	1.432
	2.178	<b>1.938</b>	<b>0.928</b>
	2.203	2.203	1.132
	2.217	2.217	1.193
	2.268	2.268	2.199

however the complexity of the configurational space at an interface combined with the high cost of DFT relaxations renders sampling all possible minima costly.

We will now take a closer look at the TiO<sub>2</sub> deficient (111) grain boundary structures found via MHM and AIRSS. These structures are of particular interest because the cation

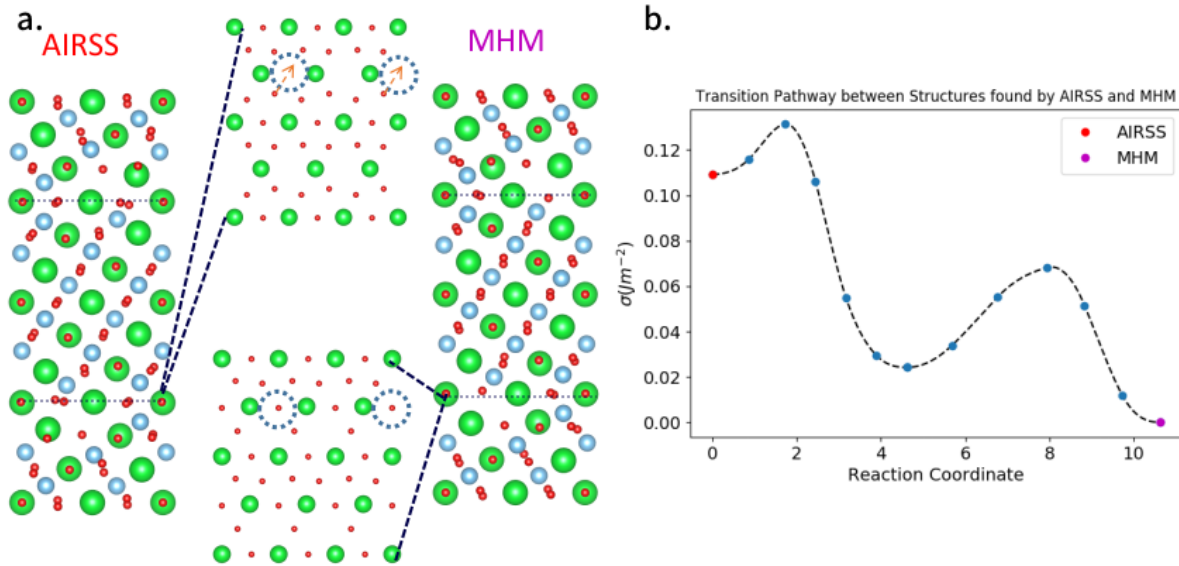


Figure 3.3. Panel a. shows the TiO<sub>2</sub> deficient (111) grain boundary structures, found by AIRSS (left) and the MHM (right). The insets show the orthogonal view of the grain boundary plane, where circles and arrows indicate the transition taken by the oxygen atoms. Panel b. shows the energy along the transition pathway between the two structures in panel a., calculated using the NEB method. All structural visualizations are drawn in VESTA [104].

occupation is consistent between the two structures, however the structure found via MHM is lower in energy by  $\approx 0.11$  J/m<sup>2</sup>. This difference in energy stems from a rearrangement of the anion sublattice, where one oxygen atom is shifted in the grain boundary region, as shown in Fig. 3.3 a. In fact, the two structures are so similar otherwise that we can easily determine a transition path between them and calculate the energy barrier. We employ the climbing image-nudged elastic band (NEB) method as implemented within the VTST toolkit [55], with fixed lattice vectors (taken from the structure found by AIRSS) and allowing all internal coordinates to relax. The energy along the NEB path is plotted in

Figure 3.3 b, showing that the forward reaction barrier (from AIRSS to MHM) is merely  $0.022 \text{ Jm}^{-2}$ .

Note also that the transition pathway between the two structures actually contains two distinct energy barriers, with the rate determining one located at a reaction coordinate of  $\approx 2 \text{ a.u.}$ . This illustrates the complexity of the PES for interfacial structure searching – even a seemingly simple transition towards the ground-state structure may encounter complicated intermediate states. Further, the MHM is particularly well suited to overcome such low barriers leading to low-energy structures, since the moves on the PES exploits the Bell-Evans-Polanyi principle which states that exothermic reactions tend to exhibit low activation energies [126].

We will briefly compare different DFT approaches to evaluate the interfacial structures of the (111) interface. Previous work using GA and AIRSS structural search algorithms utilized the CASTEP DFT code, while in the present work we use VASP with comparable DFT settings, similar to Ref. [178]. The comparison between structures as calculated using CASTEP and VASP is shown in Fig. 3.4. The differences in the results between the two DFT packages is small, with discrepancies within less than  $0.1 \text{ Jm}^{-2}$ . Most importantly, there is no change in the energetic ordering between the methods for either  $\text{TiO}_2$  poor or SrO poor grain boundary structures.

### 3.3.2. $\text{SrTiO}_3\Sigma 3$ (112)

In the (112) system, we recover the same grain boundary as Ref. [24] when two SrO units are removed at each interface (2 SrO-poor), but find a significantly more stable structure when the interface is deficient of a single SrO unit (SrO-poor). Similarly to  $\text{SrTiO}_3$  (111),

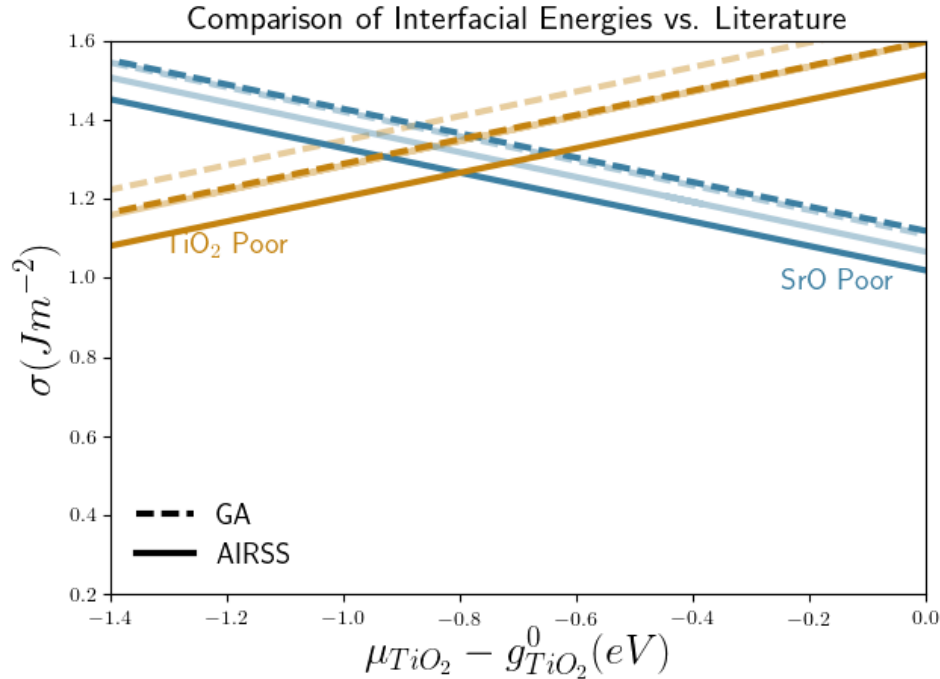


Figure 3.4. Comparison of interfacial energy of (111) GB structures found by GA and AIRSS, as reported in the literature using CASTEP, and recalculated in this work using VASP. A full discussion of the thermodynamic treatment is given in section 3.2.3. Different colors correspond to varying stoichiometries, while different line styles correspond to different structural search methods. Dashed lines and solid lines refer to Ref. [24] and [132], respectively. The lighter lines correspond to values reported in the literature (using CASTEP), while the opaque lines are from the current work (using VASP).

the lowest energy structure with DFT is the second lowest with the Buckingham potential, while the most stable structure under the Buckingham potential is less stable than many of the others reported with DFT (see lower part of Tab. 3.1). The lowest-energy structure we found with the MHM is slightly lower in energy than the energy value reported by Zhao *et al.* [178] at this stoichiometry. We contacted the authors in order to obtain the original atomic structure data reported in Ref. [178], however they were unable to locate

the data. Our careful visual inspection shows that the two structures appear similar, sharing a structural motif of one Ti coordinated by 5 O atoms in the vicinity of the grain boundary, with the orientation of this motif inverted at one grain boundary.

This structure begins to be more stable than the stoichiometric grain boundary under slightly  $\text{TiO}_2$  favoring conditions. In the thermodynamic analysis of Ref. [24], off-stoichiometry is only predicted at extreme conditions, where  $\text{TiO}_2$  is in equilibrium with  $\text{SrTiO}_3$ . While Chua *et al.* [24] were unable to find  $\text{TiO}_2$  deficient structures for this stoichiometry, we were able to recover low-energy structures with 1 and 2 units of  $\text{TiO}_2$  removed. Zhao *et al.* [178] find a very stable structure with 2  $\text{TiO}_2$  units removed, while at this stoichiometry we are only able to recover a significantly less stable structure. Note, however, that structure found with the AGA is larger in the direction perpendicular to the interfacial plane: Zhao *et al.* [178] varied the total number of atoms in their cells, including supercells that we did not consider in our work.

Since our computational setup in terms of system sizes is identical to Ref. [24], the ability of MHM to recover the  $\text{TiO}_2$  deficient structures gives further evidence that our algorithm is more useful in predicting structure at interfaces than a GA approach. Using an adaptive scheme as in Ref. [178] or machine learning interatomic potentials in conjunction with the MHM [38, 34] for interface structure prediction might further improve the efficiency of our method.

### 3.4. Conclusion

To summarize, we have successfully adapted the MHM to predict complex interface structures, using local order parameters to drive the search towards reconstructions in

the vicinity of the interface. We applied our method to study off-stoichiometric SrTiO<sub>3</sub>  $\Sigma 3$  (111) and  $\Sigma 3(112)$  [110] grain boundaries using a hybrid approach to approximate the PES, namely by conducting the structural search with an empirical potential, and subsequently refining the lowest energy candidates using local DFT relaxations. We found energetically more stable structures than those reported by Chua *et al.* [24], who used a genetic algorithm with the same Buckingham potential, and those reported by Schusteritsch *et al.* [132], who searched directly on the DFT PES using a random search approach. We found similar structures to Zhao *et al.* [178] for the same cell sizes, who used an adaptive method to improve the correspondence between their empirical EAM PES landscape and DFT.

Our calculations illustrates the complexity of interfacial structure prediction, where many configurations can exist in a very small energy range. Even a seemingly simple structural transition between two distinct interface structures exhibits a rather complex minimum energy pathway, as we demonstrate through our NEB calculations for a TiO<sub>2</sub> deficient (111) grain boundary. Effective structural search algorithms are hence called for to accurately predict the interface structures at the atomic scale, a necessary prerequisite to improve our understanding of structure-property relationships and interface engineering that probe grain boundaries as tuning parameters. By coupling our MHM with highly accurate machine-learning interatomic potentials we will be able to tackle larger system sizes with larger chemical complexity in the future.

## CHAPTER 4

**Cation Disorder and Oxygen Redox in  $\text{Li}_3\text{MO}_4$  Cathodes**

*This chapter is adapted from a publication in preparation for submission. Once accepted, permission will be requested*

**4.1. Introduction, Background, and Crystal Structure**

In the last two decades, lithium-ion batteries (LIB) have become ubiquitous in consumer technologies, enabling conveniences such as cordless tools, and technological revolutions such as the smartphone. Their role in society will only grow as they are primed to play a major role in the next phase of the energy transition in the transportation sector, as they power the electric vehicles and micromobility devices such as e-bikes that will replace miles traveled by conventional internal combustion engine vehicles. Batteries are also poised for widespread deployment into the electricity grid, where they will offer a host of grid services as more variable renewable energy sources are brought online. Improving the performance of batteries, evaluated by a host of metrics such as specific capacity (mAh/g), cost (\$/Wh), or cycle life, will allow for more rapid deployment as costs are driven down and products are improved.

In Li-ion cathode materials, such as layered  $\text{LiCoO}_2$  [102] or  $\text{LiNi}_x\text{Mn}_y\text{Co}_z\text{O}_2$  [7], spinel  $\text{LiMn}_2\text{O}_4$  [146], or olivine  $\text{LiFePO}_4$  [116], energy is reversibly stored by the facile incorporation and removal of lithium while other species generally remain in the cathode. In the conventional cathodes listed above, this reversible reaction can occur because the

transition metal(s) (TM) in the cathode are capable of taking various redox states as the Li content varies. For example, as  $\text{LiCoO}_2$  is delithiated and subsequently relithiated, the average nominal oxidation state changes from  $\text{Co}^{3.5+}$  to  $\text{Co}^{4+}$ .

In recent years, there have been efforts to increase the ratio of Li content to the heavy TM, in order to increase the capacity of these cathodes. One strategy has been to search for chemistries that form in the layered  $\text{R}\bar{3}\text{m}$  structure, but are capable of incorporating excess lithium into the TM layer, often called lithium excess layered oxides (LLO), such as  $\text{Li}[\text{Li}_{1/6}\text{Ni}_{1/6}\text{Co}_{1/6}\text{Mn}_{1/2}]$  [123]; these LLO are considered a solid solution of  $(1-y)\text{Li}_2\text{MnO}_3(y)\text{LiTMO}_2$  [62]. Within this strategy, researchers have found cathode materials in which the TM is not the only participant of the host oxide structure that is capable of reversible redox: oxygen too is capable of redox participation, flexibly moving from a nominal redox state of  $\text{O}^{2-}$  to  $\text{O}^{1-}$  [135] and even  $\text{O}^0$  [173]. This strategy has shown to be fruitful in cathodes with chemistries such as  $\text{Li}_{1.17}\text{Ni}_{0.25}\text{Mn}_{0.58}\text{O}_2$ ,  $\text{Li}_2\text{Ru}_{0.5}\text{Sn}_{0.5}\text{O}_3$ , and  $\text{Li}_{1.25}\text{Mn}_{0.5}\text{Nb}_{0.25}\text{O}_2$  [135].

In 2017, Perez et. al introduced the layered  $\text{Li}_3\text{IrO}_4$  cathode material. They found the structure was able to cycle up to  $\text{Li}_{4.7}\text{IrO}_4$ , exploiting traditional cationic redox on iridium, as well as reversibly down to  $\text{LiIrO}_4$ , exploiting anionic redox. This gives rise to a superlative capacity of about  $3.5 \text{ e}^{-1}/\text{Ir}$  and  $340 \text{ mAh g}^{-1}$ . [120].

$\text{Li}_3\text{IrO}_4$  forms in the  $\text{R}\bar{3}\text{m}$  layered crystal structure, shown in 4.1 like  $\text{LiCoO}_2$ . In  $\text{LiCoO}_2$ , there are alternating layers of pure Li and pure transition metal (Co) layer. In  $\text{Li}_3\text{IrO}_4$ , the pure Li layer remains, however the transition metal layer is instead replaced with a disordered layer that is half Ir and half Li.

In this work, we will use Density Functional Theory (DFT) calculations to study cation ordering in  $\text{Li}_3\text{IrO}_4$ , and its influence on anionic redox during delithiation. DFT has proven to be a powerful tool in studying Li-ion battery cathodes, by enabling careful study of the mechanisms for delithiation and high-throughput screening of novel candidate materials. [147, 67, 107, 74, 174].

Current theoretical studies of anionic redox in  $\text{Li}_3\text{IrO}_4$  have only considered a single ordered phase, P2/c, which has been dubbed the chain structure due to the Ir ordering, inherited from the study of  $\text{Li}_3\text{RuO}_4$ . More recently, Li et al. have studied an additional disordered phase, for which one Li and Ir in the chain ordering are exchanged [90]. This provides novel local bonding environment for  $\text{IrO}_6$  octahedra in terms of the character of the neighboring O, but the thermodynamics of the defect, or ordering in general, were not considered in this work. The present work will be outlined as follows. First, we will search for an ordered ground state for  $\text{Li}_3\text{IrO}_4$ , and introduce a disordered model structure created using special quasirandom structures [183]. Next, we will conduct a thermodynamic comparison upon delithiation of the ordered and disordered phases, quantifying predicted stability during delithiation with a convex hull construction, and predicted intercalation voltages. Then, we will consider signs of anionic redox in both the ordered and disordered  $\text{Li}_3\text{IrO}_4$ , including the density of states (DoS) at the fully occupied material, the change in local magnetization upon delithiation, and the formation of short-range O-O with anti-bonding character upon delithiation. We will then consider the role of cation disorder in the formation of oxygen defects, wrapping up our study of  $\text{Li}_3\text{IrO}_4$ . We will then apply what we've learned to screen for potential  $\text{Li}_3\text{MO}_4$  cathodes, considering the stability of ordered and disordered  $\text{Li}_3\text{MO}_4$  and  $\text{LiMO}_4$  phases. This search finds

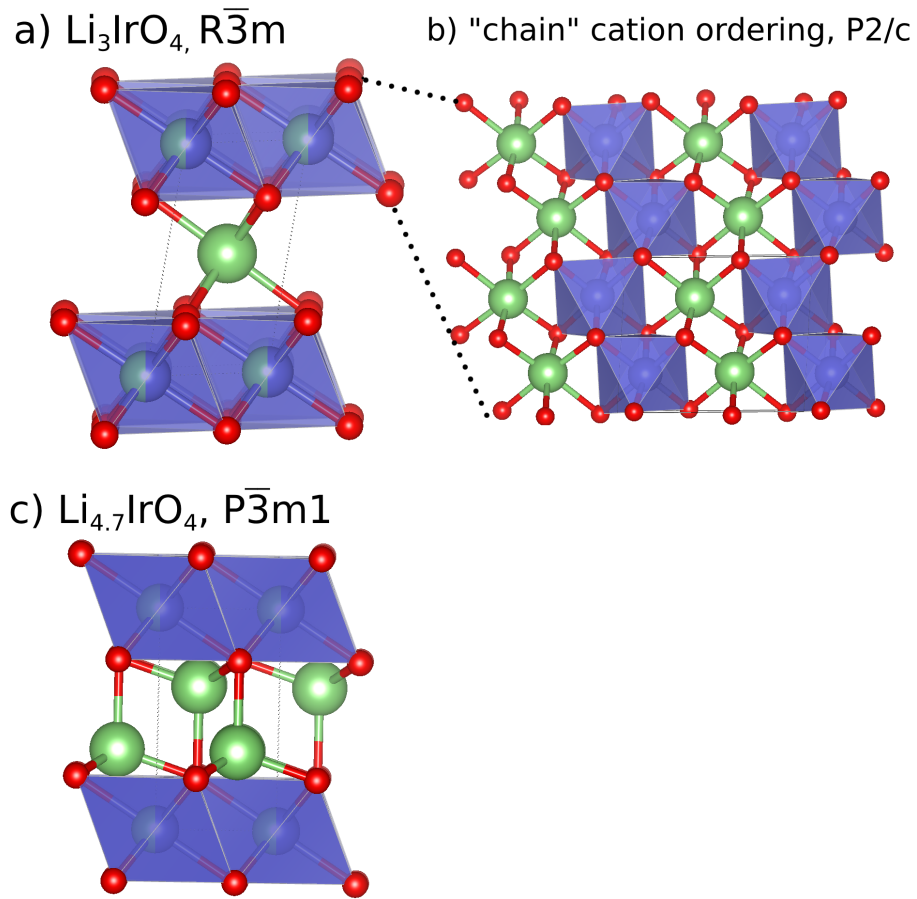


Figure 4.1. Crystal structures of lithiated  $\text{Li}_x\text{IrO}_4$  phases. a. shows the crystal structure of  $\text{Li}_3\text{IrO}_4$  with  $\overline{\text{R3m}}$  symmetry. With this symmetry, all cations sit in octahedral sites, with a mixed cation layer containing 50% Li and Ir, with no long range order. b. shows the previously studied chain ordering, corresponding to  $\text{P2/c}$  symmetry, which is known to form for  $\text{Li}_3\text{RuO}_4$ . c. shows the  $\text{Li}_{4.7}\text{IrO}_4$  structure with symmetry. Here, the mixed cation layer remains in octahedral sites, while the pure lithium layer becomes tetrahedrally coordinated. All structural visualizations are drawn in VESTA [104].

$\text{Li}_3\text{OsO}_4$  and to be a feasible candidate for further study, along with uncovering novel ordered compounds for  $\text{Li}_3\text{FeO}_4$ ,  $\text{Li}_3\text{TcO}_4$ ,  $\text{Li}_3\text{RhO}_4$ ,  $\text{Li}_3\text{PtO}_4$ ,  $\text{LiOsO}_4$ , and  $\text{LiCuO}_4$ , which may be synthesizable.

## 4.2. Methods

In this work, we use two distinct but similar calculation settings for the initial study of  $\text{Li}_3\text{IrO}_4$  and the high-throughput study of  $\text{Li}_3\text{MO}_4$ . In the case of the initial study, we use the Vienna Ab-Initio Simulation Package (VASP) for our DFT simulations [83, 84, 81, 82]. We use Projector Augmented-Wave potentials [16, 85], a plane-wave energy cut off 520 eV, and 8000 k-points per reciprocal atom (KPPRA) on a  $\Gamma$  centered mesh. Electronic steps are converged to within  $1 \times 10^{-5}$  eV. Relaxation is carried out with a force convergence of -0.005 eV/Å, using the Methfessel-Paxton of order one to describe partial orbital occupation, with a smearing width of 0.2 eV. A final static calculation is done with tetrahedron method smearing with Blöchl corrections. All calculations are spin-polarized, with Ir initialized in the high-spin state of  $5 \mu_B$ . We use a Hubbard U value of 2 eV to correct for self-interaction errors, using the rotationally invariant scheme of Dudarev [33], a common strategy when treating transition metal battery cathodes [5, 65]. Previous studies of lithium iridates have used a U value of = 1 [89] In addition, due to the layered nature of  $\text{Li}_3\text{IrO}_4$ , we use the optB88-vdW [78, 77] functional to correct for the inability of semilocal GGA methods to address non-local correlations that lead to dispersion, which are commonly found to be significant in delithiated layered oxides such as  $\text{LiCoO}_2$  [5] [64]. optB88-vdW was found to most effectively model  $\text{Li}_{0.5}\text{CoO}_2$  among 7 van der Waals correction schemes considered [5].

The literature unfortunately lacks experimental structural data for the  $\text{Li}_3\text{IrO}_4$  system upon delithiation, when Hubbard U values and van der Waals (vdW) corrections would be most necessary, so evaluating the suitability of these corrections empirically is difficult.

However, using these settings, we find that the volume per atom of the previously considered chain structure, and the low energy structure found in this work, are both within 1.1% of the experimentally measured volume per atom of  $9.09 \text{ \AA}^3$  of  $\text{Li}_3\text{IrO}_4$ .

For high-throughput calculations, we follow a multi-stage relaxation approach as used in the Open Quantum Materials Database (OQMD), as described previously [127, 76], which uses a multi-stage relaxation scheme for efficiency, followed by a high quality static calculation at the same energy cutoff and KPPRA as described above. Notably, Hubbard  $U$  is only used for a set of TM (V, Cr, Mn, Fe, Co, Ni, Cu, Th, U, Np, Pu), which do not include Ir. There is no vdW correction used for the high-throughput study.

### 4.3. Investigation of $\text{Li}_3\text{IrO}_4$ , Results and Discussion

#### 4.3.1. Cation ordering in disordered $\text{Li}_3\text{IrO}_4$ layer

Elucidating the effect of cation ordering in  $\text{Li}_3\text{IrO}_4$  is essential because it creates novel bonding environments for oxygen, which may influence the electronic behavior during delithiation. In previous work by Perez et al. and Li et al., treatment of  $\text{Li}_3\text{IrO}_4$  considered only the chain ordering of cations. In the chain ordering, half of the oxygen are coordinated by 4 Li and 2 Ir, and the other half are coordinated by 5 Li and 1 Ir. In later work by Li et. al, an anti-site defect was considered in which a  $1 \times 2 \times 1$  supercell of the chain-ordering structure was created, and then an Ir and Li were swapped. This defect arrangement does not change the total number of oxygen of each coordination in the structure, but leads to subtle changes in the reported electronic density of states (DoS) and x-ray absorption spectra (XAS). Li et. al argue that the oxygen coordinated by 4 Li and 2 Ir have 2 lone pairs, ( $\text{O}_{2LP}$ ), and the oxygen coordinated by 5 Li and 1 Ir have 3 lone pairs ( $\text{O}_{3LP}$ ).

Their proposed defect arrangement leads to a novel environment for Ir, in terms of  $O_{2LP}$  and  $O_{3LP}$ . In the base chain ordering, all of the Ir are coordinated by 4  $O_{2LP}$  and 2  $O_{3LP}$ , while in the antisite defect, there are Ir coordinated by 3  $O_{3LP}$ .

We've taken three main approaches to address structural disorder in  $Li_3IrO_4$ . The first is by building a binary cluster expansion of the disordered cation sites on the  $R\bar{3}m$  crystal structure. As described in section 2.3, a cluster expansion is a means of creating a generalized Ising-like Hamiltonian, fit using calculated energies such as those from DFT. The atoms in the mixed cation layer are labeled  $S_i = \pm 1$ , indicating occupation by either Li or Ir. Though the oxygen and pure lithium layers are involved in calculating the energy of each structure, they do not have explicit occupation labels. Thus, we are building a cluster expansion of the  $Li_{4-2x}Ir_{2x}O_4$ ,  $0 \leq x \leq 1$  system.

We note that near extreme values of  $x$ , we expect to form structures that may have qualitatively different bonding, which might be challenging to capture with a cluster expansion model. At  $x = 0$ , we are forming  $LiO$ , at  $x=0.5$ , we form our target composition of  $Li_3IrO_4$ , and at  $x = 1$ , we form  $LiIrO_2$ . If we assume oxygen has a charge state of  $O^{2-}$ , the cation charge states for these phases are:  $Li^{2+}$  at  $x = 0$  (likely indicating an ionic picture does not fit);  $Li^{1+}$ ,  $Ir^{5+}$  at  $x = 0.5$ , and  $Li^{1+}$ ,  $Ir^{3+}$  at  $x = 1$ . According to the OQMD and the ICSD, iridium forms oxides in the phases  $IrO_2$  and  $IrO_3$ , corresponding to charge states of  $Ir^{4+}$  and  $Ir^{6+}$  respectively. Further, there are no compounds known to form with the composition  $LiIrO_2$ ; the layered  $LiIrO_2$  structure is the lowest energy structure in the OQMD at this composition, with a stability of 0.182 eV/atom above the convex hull. Fig. 4.2 shows the details of the cluster expansion, fitted using the *maps* program as implemented in ATAT [156] on 121 total structures. Panels a) and b) show

the formation energies as predicted by the cluster expansion and as calculated by DFT, respectively, while panel c) shows the effective cluster interaction as a function of the cluster diameter. To calculate formation energies,  $\Delta E$  from total energies, we take end members as reference states, subtracting their energy in a ratio dependent on the value of  $x$ :

$$(4.1) \quad \Delta E_{\text{Li}_{4-2x}\text{Ir}_{2x}\text{O}_4} = E_{\text{Li}_{4-2x}\text{Ir}_{2x}\text{O}_4} - 4(1-x) * E_{\text{LiO}} - 2x * E_{\text{LiIrO}_2}$$

Here,  $E$  refers to total energies per formula unit. For example, at  $x = 0.5$

$$(4.2) \quad \Delta E_{\text{Li}_3\text{IrO}_4} = E_{\text{Li}_3\text{IrO}_4} - 2E_{\text{LiO}} - E_{\text{LiIrO}_2}$$

For the plotted convex hulls, these energies are normalized per mixing site. We note the very strong nearest neighbor pair interaction dominates the cluster expansion. The cross-validation score of the cluster expansion 24.7 meV / mixing site, and known and predicted ground states agree. The low energy structure at the composition of  $\text{Li}_3\text{IrO}_4$  is not the chain structure with  $P2/c$  symmetry, but instead a structure with monoclinic  $C2/m$  symmetry. This structure is shown in Fig. 4.3. The cluster expansion approach has limitations due to the size of cell considered, as well as the fact that it covers stoichiometries besides  $\text{Li}_3\text{IrO}_4$ . In addition, we've generated more possible structures via enumeration using the Supercell package, generating all structures up to 64 atoms that can be formed using  $AxBxC$  size supercells of the primitive cell, where  $A$ ,  $B$ , and  $C$  are integers less than or equal to 4. Finally, we have also generated a Special Quasirandom Structure (SQS) as a model for the fully disordered cation layer [183], generated using the `mcsqs` routine implemented in ATAT [157]. The SQS is generated by considering clusters

up to 6A for pair, triplet, and quadruplet clusters. We show the energy of the enumerated structures and SQS, along with the previously discussed line, chain, and chain disordered structures, in Table 4.1. The structures containing oxygen coordinated by 6 Li are notably high in energy, compared to the structures without these formations. We notice a monotonic relationship between the fraction of O coordinated by 6 Li and the calculated DFT stability. The SQS structure is 136 meV/atom higher in energy than the ordered phase, and though we have not accounted for the stabilizing factor configurational entropy with increasing temperature, the experimental synthesis temperature of 1223 K would not come close to countering this penalty for disorder. However, inspired by investigations in the  $\text{Li}_5\text{FeO}_4$  system [175], in which these oxygen coordinated by 6-Li were found to be critical in anionic redox, we will consider their behavior upon delithiation and their role in anionic redox.

#### 4.3.2. Thermodynamics of Delithiation and Lithiation of Ordered and Disordered $\text{Li}_3\text{IrO}_4$ Phases

We will next discuss the role of cation ordering in thermodynamic behavior of  $\text{Li}_3\text{IrO}_4$  upon lithiation and delithiation. During extreme delithiation, the competing phases with  $\text{Li}_x\text{IrO}_4$  are, according to the OQMD, the formation of  $\text{IrO}_3$  and  $\frac{1}{2}\text{O}_2$ . The under prediction of oxide formation energies from elemental references when using GGA methods such as PBE, is well established, and has been ascribed to the high reference energy of  $\text{O}_2$ . We will follow the work of Grindy et. al, and calculate a set of 14 binary oxides using our settings to correct for this effect. We have used an identical set of oxides for this correction this previous work, with the exception of  $\text{In}_2\text{O}_3$ , and find that it is just  $C=-0.013 \text{ eV/O}_2$ ,

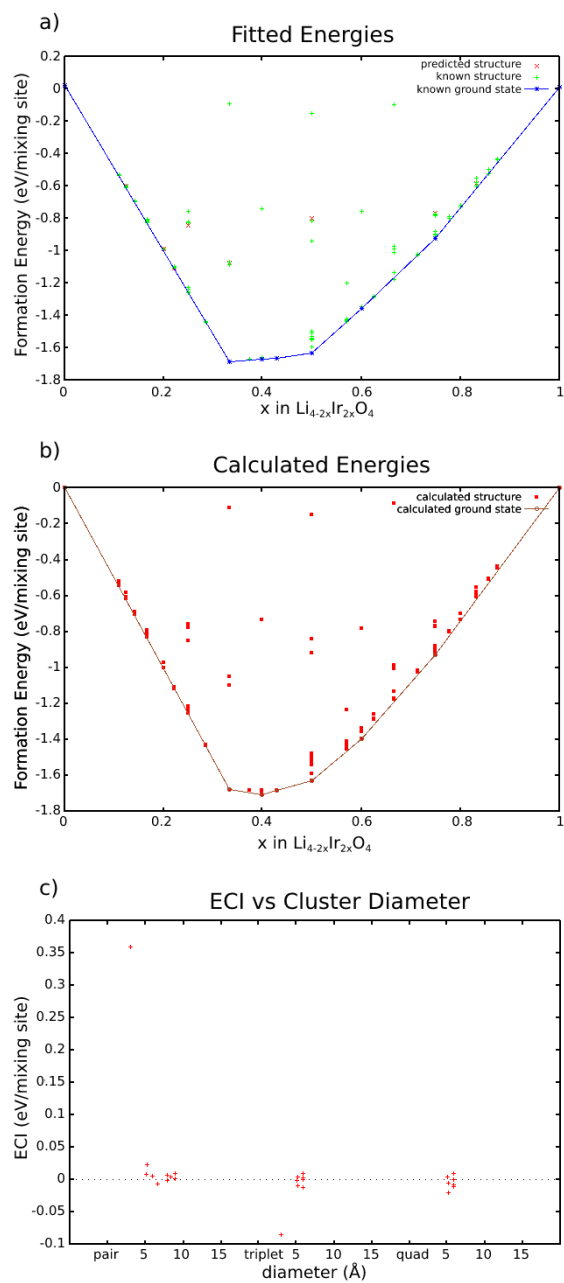


Figure 4.2. a) Formation energies predicted by the cluster expansion. b) Formation energies as calculated by DFT c) Effective cluster interaction of fitted cluster expansion, as a function of cluster diameter.

Table 4.1. Summary of  $\text{Li}_3\text{IrO}_4$  structures screened using the enumeration approach, with the addition of other structures discussed in the text. Also included is the lattice system and space group, as well as the fraction of O with a specific nearest neighbor coordination environment. All oxygen are 6 fold coordinated by a combination of Li and Ir. Formation energies are given as calculated using electrostatic interactions by the initial enumeration facilitated by *supercell*, as well as DFT. For both, predicted ground states are set to 0.

Struct. name	Lattice System	Space Group	ES Stab. (eV/atom)	Frac of O Coord. by x Li				DFT Stab. (eV/atom)
				3	4	5	6	
Line	Monocl.	C2/m	0.027	0	0.5	0.5	0	0.000
scell-1	Orthorh.	P2/m	0.000	0	0.5	0.5	0	0.009
chain dis.	Monocl	P2		0	0.5	0.5	0	0.029
chain	Monocl.	P2/c		0	0.5	0.5	0	0.031
scell-2	Triclinic	P-1	0.326	0.062	0.437	0.437	0.062	0.067
scell-3	Triclinic	P-1	0.473	0.083	0.416	0.416	0.083	0.080
scell-6	Triclinic	P-1	0.764	0.166	0.25	0.5	0.083	0.095
scell-5	Triclinic	P1	0.757	0.166	0.25	0.5	0.083	0.099
scell-4	Triclinic	P1	0.757	0.083	0.5	0.25	0.166	0.118
scell-7	Triclinic	P1	0.764	0.083	0.5	0.25	0.166	0.119
SQS	Triclinic	P1		0.125	0.375	0.375	0.125	0.136

far smaller than chemical accuracy (about 40 meV/formula unit), when calculated with opt-B88-vdW, and thus do not include it in future analysis. For comparison, for PBE and LDA, Grindy et al. found values of  $C = -1.198$  and  $0.254$  respectively. Our analysis is shown in Fig. 4.4.

In order to investigate the interplay of cation disorder and anionic redox in  $\text{Li}_3\text{IrO}_4$ , we have chosen to delithiate both the low energy C2/m phase and the disordered SQS structure, as limiting cases for ordered and disordered models.

Structural screening via a simple proxy method such as electrostatics proves challenging here for two reasons. First, the multiple possible charge states of O ( $\text{O}^{2-}$ ,  $\text{O}^{1-}$ ,  $\text{O}^0$ )

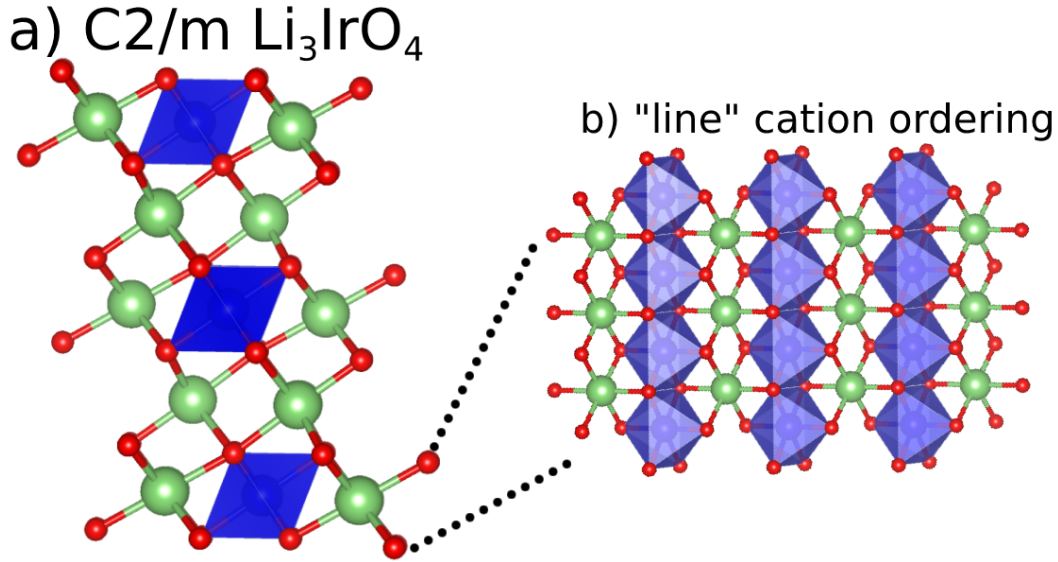


Figure 4.3. a) The low energy structure found via cluster expansion at the composition  $\text{Li}_3\text{IrO}_4$ , with C2/m symmetry b) the view of the mixed cation plane.

and Ir ( $\text{Ir}^{5+}$ ,  $\text{Ir}^{6+}$ ,  $\text{Ir}^{7+}$ ) increases the complexity of the screening. Second, as delithiation opens voids in the structure, we see more severe atomic relaxation off lattice sites. In particular, we note significant shortening of oxygen-oxygen neighbor distance in the delithiated disordered cells. Thus, we instead enumerate cells at stoichiometries  $\text{Li}_2\text{IrO}_4$  and  $\text{LiIrO}_4$ . For the ordered phase, which just contains 2 symmetrically distinct Li sites in the primitive unit cell, we generate the 2 possible structures for  $\text{Li}_2\text{IrO}_4$  and  $\text{LiIrO}_4$  from a single unit cell. Further, to probe whether more complex delithiated structures might be energetically favorable, we built structures from a  $2 \times 2 \times 2$  parent supercell containing 64 total atoms at a composition of  $\text{Li}_3\text{IrO}_4$ . We removed atoms such that zero, 0.25, 0.5, 0.75, or all lithium atoms were remaining in the mixed layer, creating 3 such structures for each occupation possibility. This leads to 15 delithiated structures each of  $\text{Li}_2\text{IrO}_4$

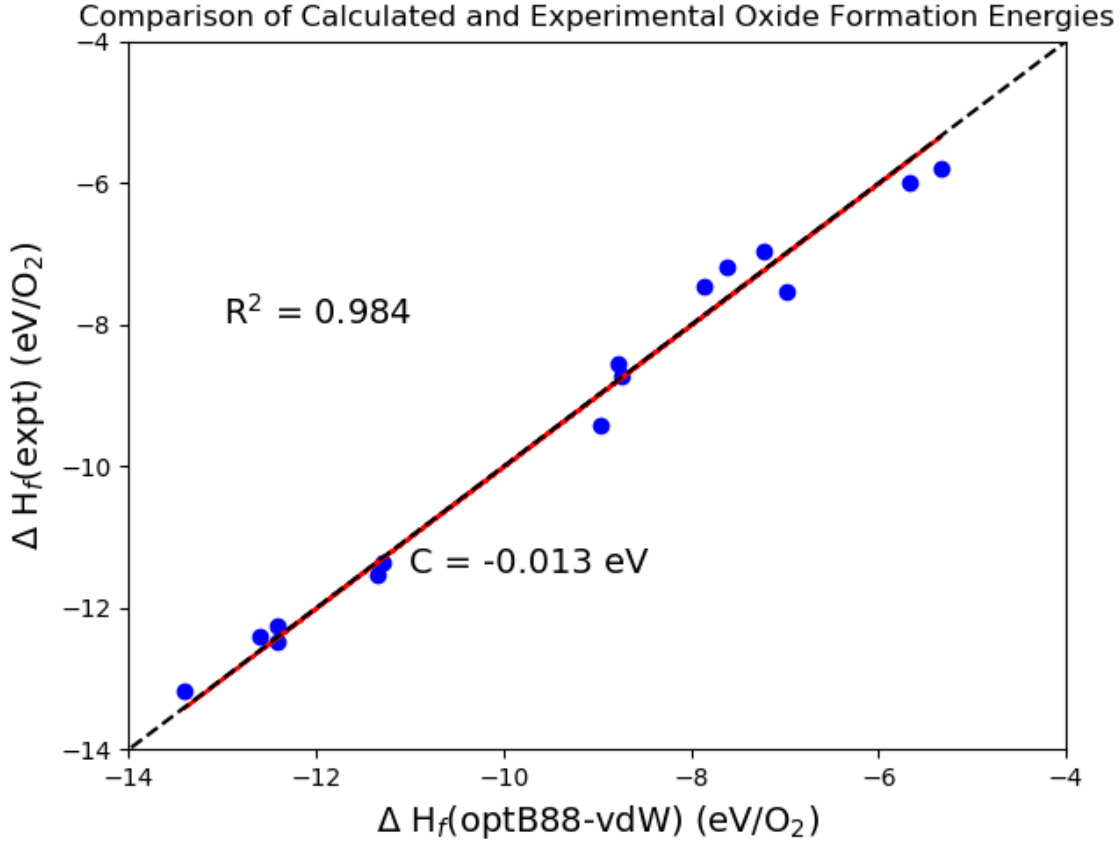


Figure 4.4. Comparison formation energy of binary oxides as calculated using the optB88-vdW functional and experiment. The correction of  $C = -0.013 \text{ eV/O}_2$  is within chemical accuracy, and is thus not added to future analysis.

and  $\text{LiIrO}_4$  from the parent  $\text{Li}_3\text{IrO}_4$  supercell. We follow a similar procedure for the SQS disordered cell, which is originally a 64 atom supercell. In this case, we create 5 structures for each occupation possibility. This leads to 25 delithiated structures each of  $\text{Li}_2\text{IrO}_4$  and  $\text{LiIrO}_4$  from the parent  $\text{Li}_3\text{IrO}_4$  supercell. There are many more possible structures, some quite likely lower in energy than what we have found, that we have not explored for the disordered cation case; with 24 total lithium atoms that are all unique in the SQS, there

are  $\binom{24}{8} = \binom{24}{16} = 735,471$  total candidates. Though 25 structures is very small compared to this number, we highlight that the relaxations are very computationally expensive for the delithiated disordered phases. Each took between 300-500 atomic steps to fully relax, likely due to the slow formation of O-O bonds, and each step is quite expensive due to low symmetry and large unit cell. Thus, our goal is not to find the exact lowest energy phase, but to find structural motifs that reveal signs of anionic redox. We have also calculated structures for which all Li have been removed, forming  $\text{IrO}_4$  structures from parents with ordered and disordered cation layers.

We plot the formation energies for these delithiated structures on a convex hull, against the formation of  $\text{IrO}_3 + \frac{1}{2}\text{O}_2$  for the  $\text{IrO}_4$  composition (as predicted by the OQMD), and  $\text{Li}_3\text{IrO}_4$  in Figure 4.5. We show two convex hulls, the first with formation considered against the stable C2/m  $\text{Li}_3\text{IrO}_4$  phase, which contains information on delithiated structures from both the ordered and disordered structures. In the second, we show the convex hull against the formation of the disordered  $\text{Li}_3\text{IrO}_4$  phase from the SQS, containing just the structures formed from the SQS parent cell. We could consider this as analogous to the Ir sites being kinetically trapped at their disordered positions, while the facile Li are able to move during cycling. The definition of the formation energy  $\Delta E$  is similar to the case for the cluster expansion, shown in Equation 4.1.

$$(4.3) \quad \Delta E_{\text{Li}_x\text{IrO}_4} = E_{\text{Li}_x\text{IrO}_4} - \left(\frac{x}{3}\right) * E_{\text{Li}_3\text{IrO}_4} - \left(\frac{3-x}{3}\right) * (E_{\text{IrO}_3} + \frac{1}{2}E_{\text{O}_2})$$

We note that the energy difference between ordered and disordered structures becomes significantly smaller as we delithiate. At a composition of about  $\text{Li}_3\text{IrO}_4$  the difference is about 110 meV/atom, which reduces to 50 and 60 meV for  $\text{Li}_2\text{IrO}_4$  and  $\text{LiIrO}_4$ . We also

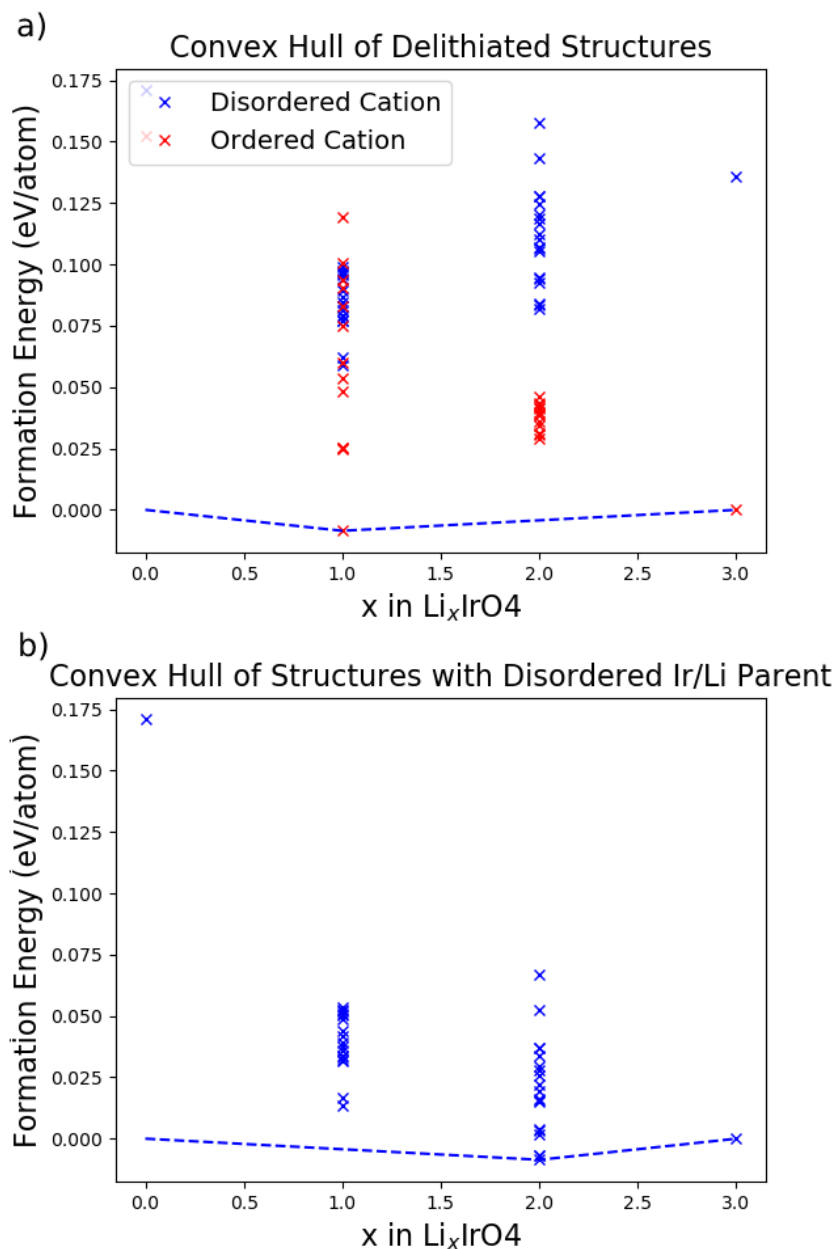


Figure 4.5. Convex hulls of formation energies during delithiation, defined against  $\text{Li}_3\text{IrO}_4$ ,  $\text{IrO}_3$ , and  $\text{O}_2$ , as in Equation 4.3. a) is defined against the ordered  $\text{Li}_3\text{IrO}_4$  structure with  $C2/m$  symmetry. We note the stable formation of an ordered structure at  $\text{LiIrO}_4$ , corresponding to a structure without any lithium remaining in the mixed layer. The energy difference between ordered and disordered structures becomes significantly smaller upon delithiation. b) shows the convex hull, considering only structures constructed from the disordered parent.

note that at  $\text{Li}_2\text{IrO}_4$ , all structures derived from the ordered parent structure are closely clustered, and much lower in energy than the structures derived from the disordered parent structure, while at  $\text{LiIrO}_4$  the two types of delithiated structures overlap in energy range.

### 4.3.3. Calculation of OCV

For the lithiation of delithiation of  $\text{Li}_3\text{IrO}_4$ , we can define the open circuit voltage (OCV) relative to  $\text{Li}/\text{Li}^+$  as follows:

$$(4.4) \quad V = \frac{\Delta G_f}{F \Delta N_{Li}}$$

Here  $F$  is the Faraday constant, and  $\Delta N_{Li}$  is the amount of Li removed.  $\Delta G_f$  is the change in free energy per mole, and can be approximated from the total energy  $\Delta E$  from DFT calculations.

$$(4.5) \quad \Delta E = E_{\text{Li}_x\text{IrO}_4} - E_{\text{Li}_{x'}\text{IrO}_4} - (x - x')E_{Li}$$

This is equivalent to stating that the open-circuit voltage is proportional to the difference in chemical potential of lithium,  $\mu_{Li}$  between the cathode and anode:

$$(4.6) \quad -eV(x) = \mu_{Li}(\text{Li}_x\text{IrO}_4) - \mu_{Li}(\text{Li metal})$$

The voltage profiles are shown in Figure. 4.6, and overlaid on the voltage profile obtained during reversible cycling up to  $\text{LiIrO}_4$  from Perez et al [120]. We note that the ordered cation voltage, calculated to be about 3.75 V vs.  $\text{Li}/\text{Li}^+$ , is in good agreement with the

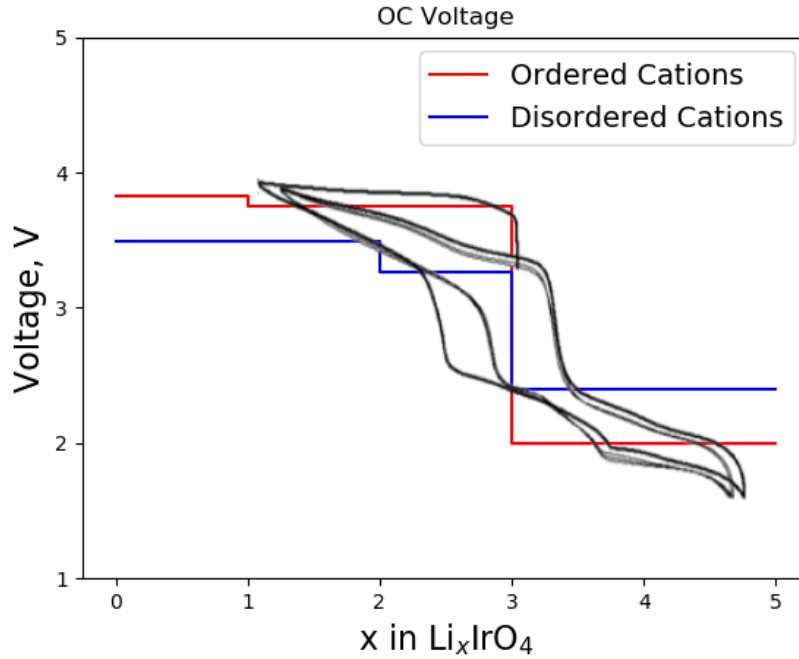


Figure 4.6. Open circuit voltage, as calculated using 4.4, for structures with ordered and disordered mixed cation layers. Here, the ordered cation voltage profile is calculated from  $\text{Li}_5\text{IrO}_4$ ,  $\text{Li}_3\text{IrO}_4$ , and  $\text{LiIrO}_4$  structures with the line ordering for the mixed cation layer, with the  $\text{LiIrO}_4$  structure with  $C_m$  symmetry found during delithiation. The disordered cation voltage profile is calculated from  $\text{Li}_5\text{IrO}_4$  and  $\text{Li}_3\text{IrO}_4$  structures with the disordered cation layer, as modeled using SQS. For both cases, the state for  $\text{IrO}_4$  is the formation of  $\text{IrO}_3$  and  $\frac{1}{2}\text{O}_2$ . Overlaid is the experimental voltage profile during cycling, delithiating up to  $x = 1$ , from Ref. [120]

flat voltage profile during the first cycle, while the disordered cation voltage, at about 3.48, is close to the average voltage during the subsequent cycles. However, during the subsequent cycling, we see a climbing voltage profile that is reminiscent of the delithiation of  $\text{LiCoO}_2$ .

#### 4.3.4. Signs of Anionic Redox and the Role of Cation Disorder

We will now consider three signs of anionic redox. As we discussed in the previous section, cation disorder could play an important role in anionic redox due to the presence of novel bonding environments, particularly for oxygen. The first will be by considering the density of states (DoS) of the ordered and disordered  $\text{Li}_3\text{IrO}_4$  structures. Seo et. al argue that the excess of O2p states, below the Fermi level, unmatched by cation states, is an indication that the oxygen site is capable of facilitating redox [135]. The DoS for the C2/m ordered structure and the SQS are shown in Figure 4.7, and were plotted using the Sumo program [96], with a Gaussian broadening of 0.1 eV applied. We can clearly see that the presence of disorder increases the excess O2p states below the Fermi level.

Next, we consider behavior the calculated local magnetization of Ir and O during delithiation, which we can use to understand unpaired electron spins. A schematic of the expected magnetization behavior of O and Ir ions in octahedral sites is shown in Figure 4.8, as well as the expected behavior of hybridized O 2p orbitals upon bond formation, following the arguments made by Chen et al. The loss of electrons from the 2p orbitals of  $\text{O}^{2-}$  should increase the local magnetization, which would be a simple sign of anionic redox activity upon delithiation. Further complicating the matter is possibility of oxygen bonding: in the case of peroxo-like  $\text{O}_2^{2-}$  formation, we expect the hybridized bond to show no local magnetic moment. Further electron loss upon formation of superoxo-like  $\text{O}_2^{1-}$  would reintroduce a local magnetic moment. Chen et al. report typical values of 1.49 and 1.28 Å for peroxo and superoxo O-O bond length. The magnetization of each Ir and O ion during delithiation is shown for structures with ordered and disordered parent structures in Figure 4.9. We can see that the introduction of disorder increases the range

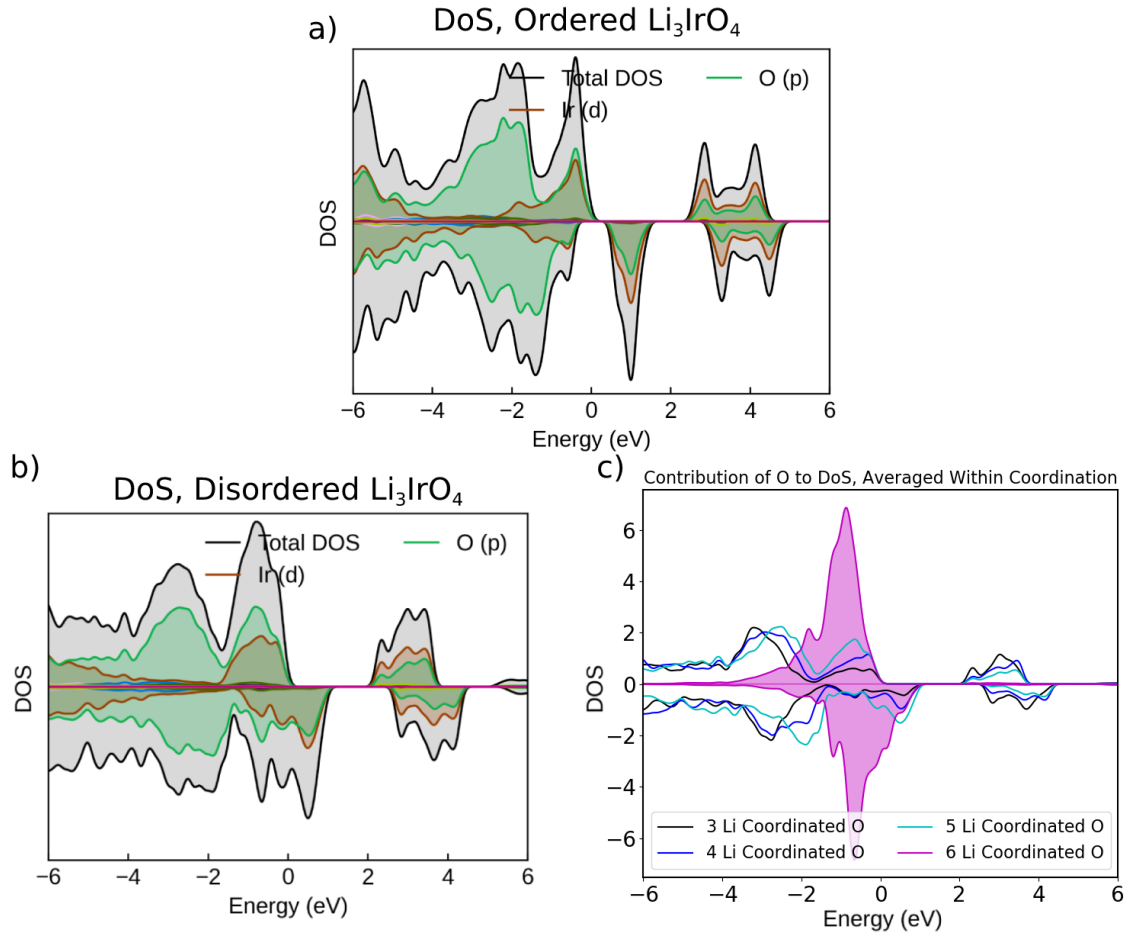


Figure 4.7. Density of States for a) ordered and b) disordered  $\text{Li}_3\text{IrO}_4$ . c) shows the Disordered DoS from oxygen specifically, averaged over all O sites with the same nearest neighbor environment. For all figures, the Fermi level  $E_F = 0$ . The DoS of the disordered structures shows significant excess  $\text{O}_{2p}$  states near the band edge.

of magnetization values for O for both  $\text{Li}_3\text{IrO}_4$  and  $\text{Li}_2\text{IrO}_4$ . Interestingly, we calculate that the stable Cm structure of ordered  $\text{LiIrO}_4$  does not exhibit magnetism at all.

Looking more closely at the magnetic behavior of iridium in the disordered structures, we see a decline in the magnetic moment during delithiation, which would indicate an increase in the positive charge state of the Ir cation, corresponding to some degree of

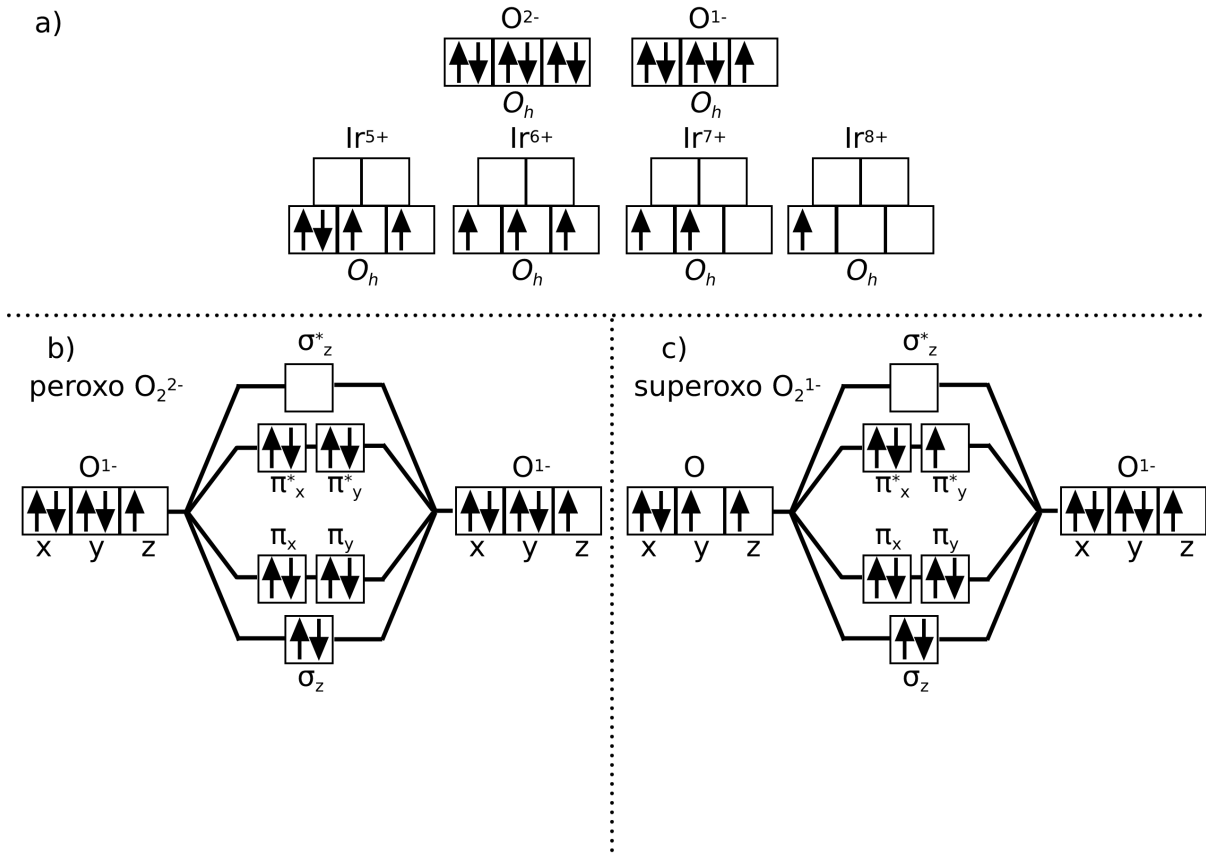


Figure 4.8. Schematics showing expected magnetization behavior. Panel a) shows the possible magnetization behavior for oxygen and iridium as we delithiate, and the remaining ions in the system lose electrons as the system loses  $Li^+$  ions. For oxygen in octahedral sites, we show that a change in charge oxidation state from  $O^{2-}$  to  $O^{1-}$  leads to an unpaired electron, and therefore non-zero magnetization. For Ir in octahedral sites, we show that we should initially increase magnetization as an electron loses its pair, followed by a decrease of magnetization as electrons are lost. Panels b) and c) show the expected behavior when two oxygen form a bond and the 2p valence states hybridize. Panel b) corresponds to peroxo-like bonding, in which each oxygen are missing an electron vs  $O^{2-}$  and form a bond with negligible magnetization c) corresponding to superoxo-like bonding, in which one oxygen is missing a further 2p valence electron, leading to a bond with sizable magnetization. Both types of oxygen bonding lead to significant anti-bonding character due to the population of  $\pi^*$  type bonds.

traditional cation redox. However, the disordered structures also show significantly more oxygen with substantial magnetic moments.

Further, we note that disordered  $\text{Li}_2\text{IrO}_4$  have 5 oxygen with short O-O bond distances, one set of 3 oxygen forming a linear chain across the mixed cation layer, and another pair of bonded oxygen, all with distances of about 1.42 Å.  $\text{LiIrO}_4$  has 4 oxygen with short O-O bond distances of about 1.24 Å. In both cases, all of these oxygen are calculated to have negligible local magnetic moment, indicating their peroxo-like character. We confirm the anti-bonding character of these bonds by calculating the projected Crystal Orbital Hamilton Populations (pCOHP) using Lobster [32, 29]. We show the average for short O-O bonds found in the disordered  $\text{Li}_2\text{IrO}_4$  and  $\text{LiIrO}_4$  in Fig. 4.10. Note that we follow convention in plotting the -pCOHP, with negative values in the vicinity of the Fermi level  $E_F$  corresponding to anti-bonding states.

Next, we will discuss the predicted stability against oxygen vacancy formation of the  $\text{Li}_3\text{IrO}_4$  and delithiated  $\text{Li}_x\text{IrO}_4$ ,  $0 \leq x \leq 2$  structures inheriting both ordered and disordered cations from the Line and SQS structures respectively. The formation energy of a dilute oxygen vacancy  $\Delta E_v^O$  is calculated as:

$$(4.7) \quad \Delta E_v^O = E_{\text{Li}_x\text{IrO}_{4-\delta}} - E_{\text{Li}_x\text{IrO}_4} + \mu_O$$

Here,  $E_{\text{Li}_x\text{IrO}_{4-\delta}}$  and  $E_{\text{Li}_x\text{IrO}_4}$  are the DFT energy of the structures, with and without the oxygen vacancy incorporated, and  $\mu_O$  is the chemical potential of oxygen, corresponding to the uncorrected  $\frac{1}{2}\text{O}_2$  reference state.

Oxygen vacancy results are shown in Figs. 4.11 and 4.12. The initial introduction of disorder to the  $\text{Li}_3\text{IrO}_4$  leads to oxygen fully coordinated by 6 Li, the least stable

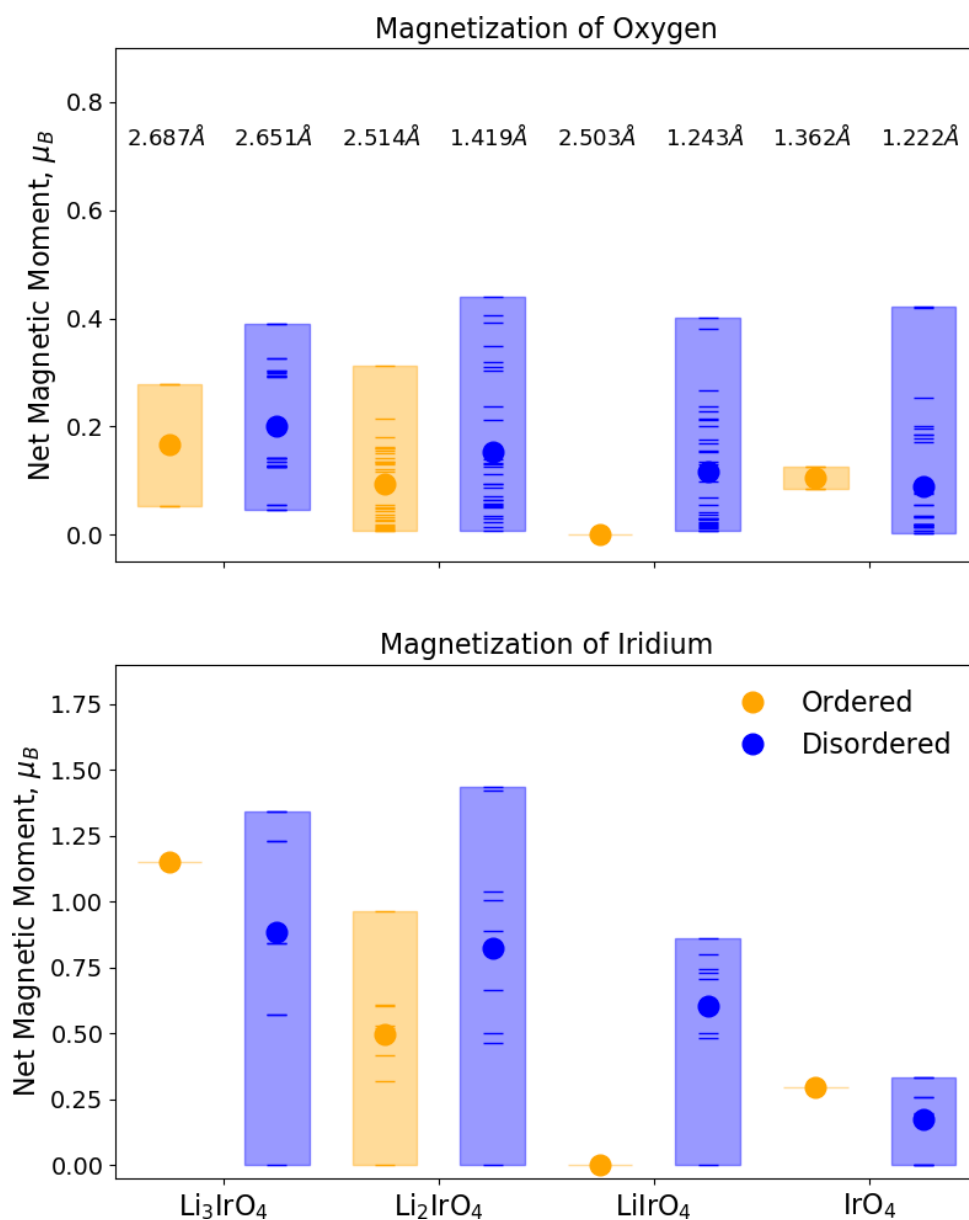


Figure 4.9. The local net magnetic moment of O and Ir ions during delithiation, for  $\text{Li}_x\text{IrO}_4$  structures with ordered and disordered parent lattices, taking the lowest energy structure found as an example. Boxes show the range of magnetization, while the solid circles mark the average magnetization value. Also shown are the minimum O-O bond distances in each structure. We can see that the presence of disorder shifts up both the average magnetization of oxygen, as well as the extreme values, and leads to short O-O bonds  $\leq 1.5$  Å at  $\text{Li}_2\text{IrO}_4$  and  $\text{LiIrO}_4$ .

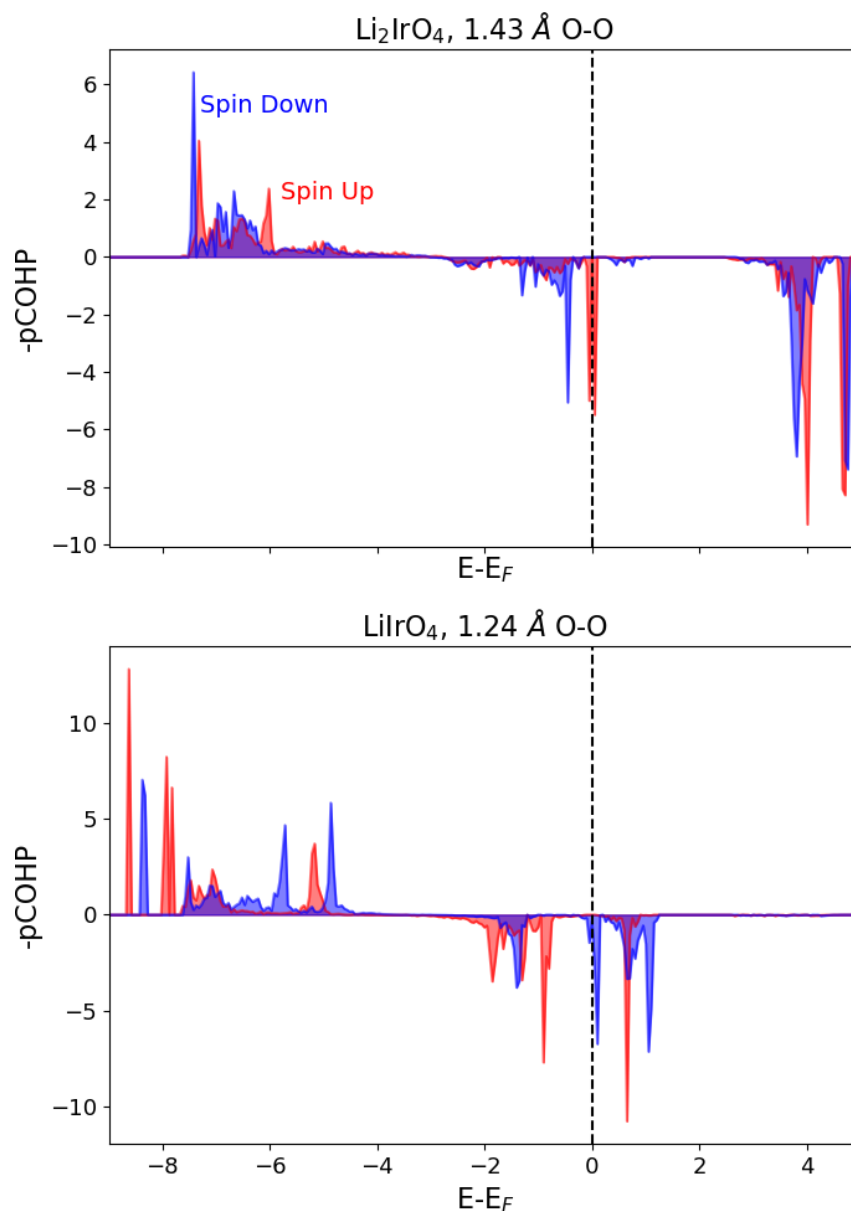


Figure 4.10. projected Crystal Orbital Hamilton Populations of short O-O bonds formed during delithiation of disordered  $\text{Li}_3\text{IrO}_4$ . Note that we have plotted the  $-\text{pCOHP}$  values, with the shown negative y-axis values indicating anti-bonding states. This analysis confirms the anti-bonding character of the observed O-O bonds from the schematic shown in Fig. 4.8.

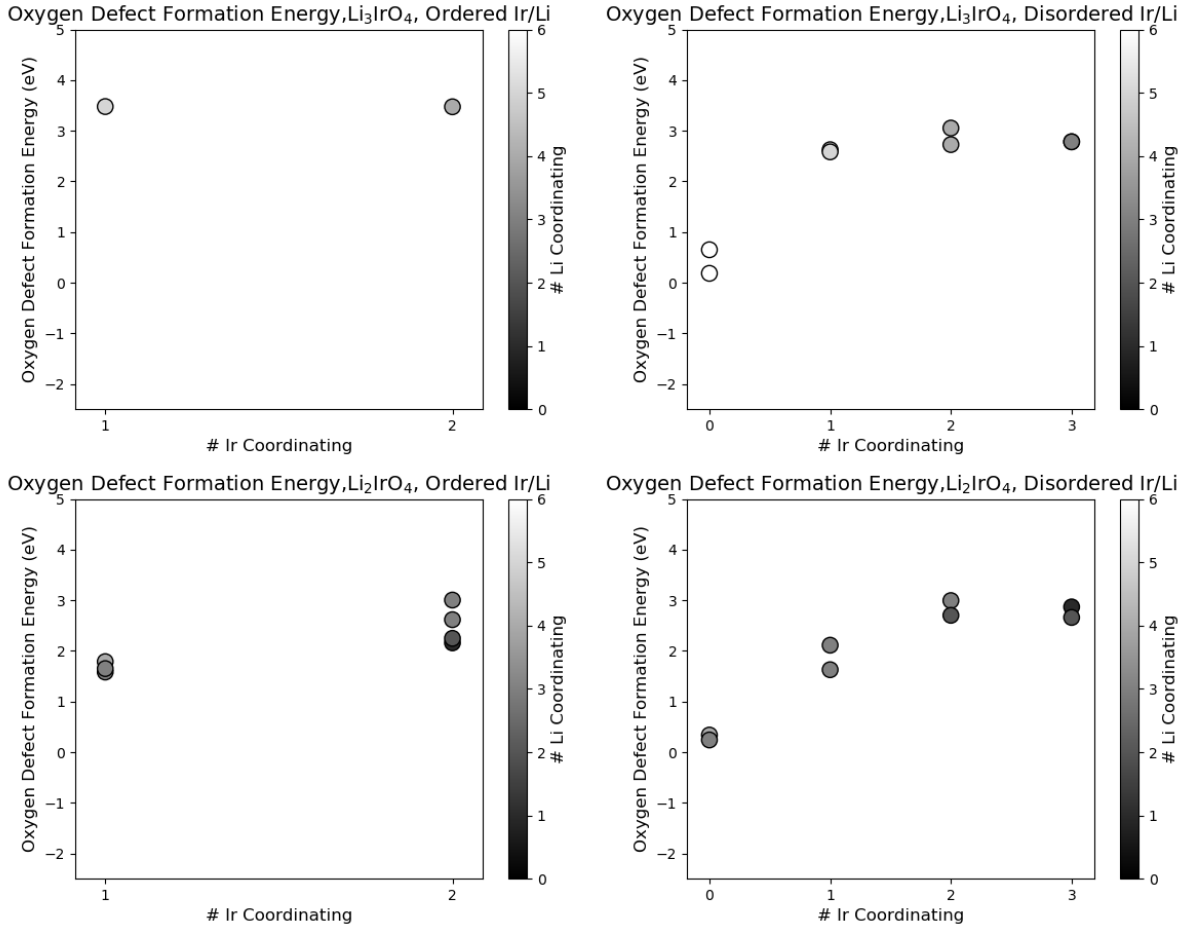


Figure 4.11.  $\Delta E_v^O$  of  $\text{Li}_3\text{IrO}_4$  and  $\text{Li}_2\text{IrO}_4$  structures, with ordered and disordered cation lattice. The  $\text{Li}_2\text{IrO}_4$  structures inherit the initial cation ordering from the fully lithiated Line and SQS structures, here we report results for the lowest energy delithiated  $\text{Li}_2\text{IrO}_4$  found during structural search. On the x-axis, we plot the number of coordinating Ir of the removed O, while the marker shade indicates the number of coordinating Li.

of which has a very low  $\Delta E_v^O$  of about 0.183 eV, so we still predict stability against spontaneous O release. In the fully lithiated case, oxygen coordinated by 4 and 5 Li in the disordered structure are lower in energy by about 1eV compared to the similarly coordinated oxygen in the ordered case. During delithiation, we see a reduction in defect formation energy for the ordered cation  $\text{Li}_2\text{IrO}_4$ , comparable with similarly coordinated

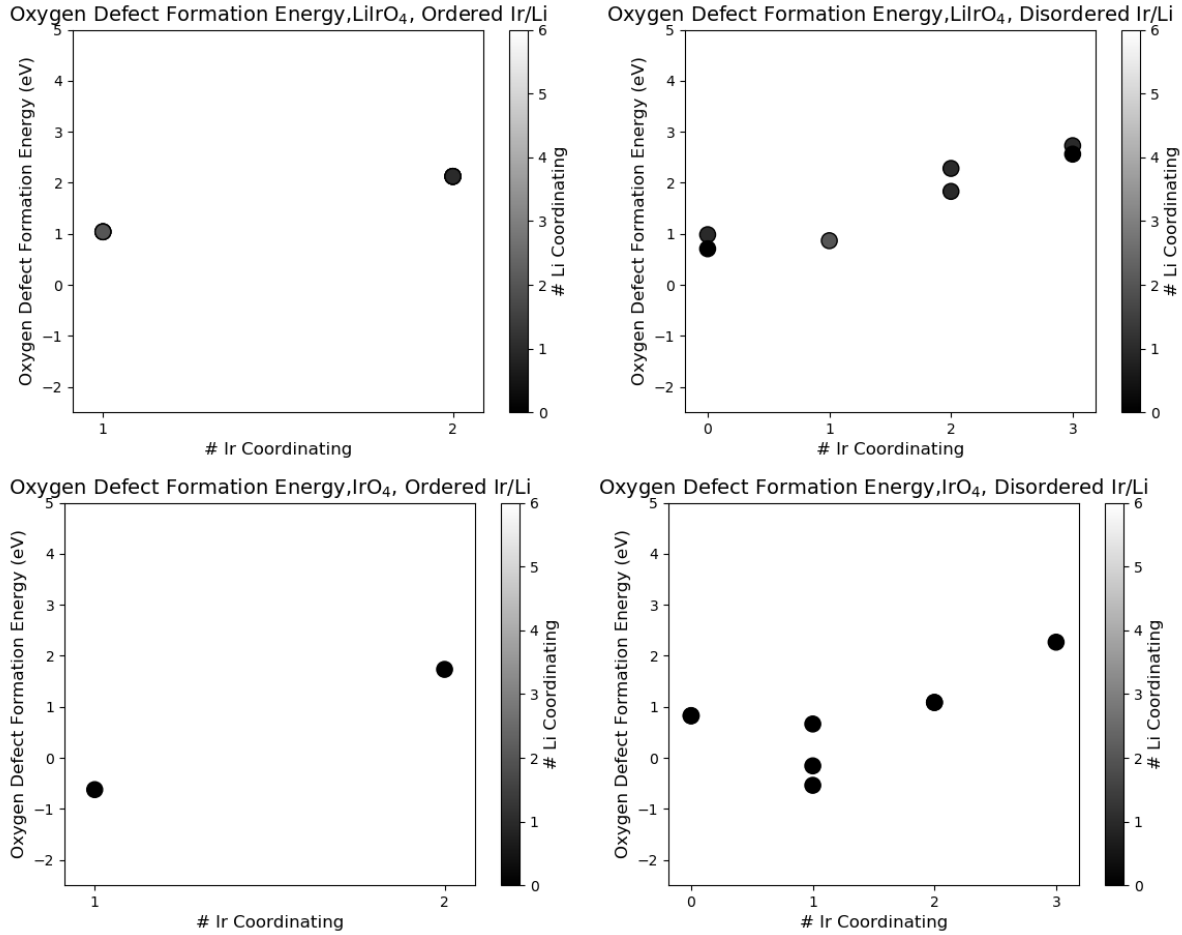


Figure 4.12.  $\Delta E_v^O$  of LiIrO<sub>4</sub> and IrO<sub>4</sub> structures, with ordered and disordered cation lattice. The LiIrO<sub>4</sub> and IrO<sub>4</sub> structures inherit the initial cation ordering from the fully lithiated Line and SQS structures, here we report results for the lowest energy delithiated LiIrO<sub>4</sub> found during structural search. On the x-axis, we plot the number of coordinating Ir of the removed O, while the marker shade indicates the number of coordinating Li.

oxygen in the disordered cation case. The oxygen were initially coordinated by 6 Li experience significant local delithiation, such that they are now coordinated by 3 or 4 Li, however the lowest defect formation energy actually increases to about 0.24 eV, likely due to the formation of a short range O-O bond. The lithium coordinated by 1 Ir see

a significant reduction in  $\Delta E_v^O$ . When delithiation reaches  $\text{LiIrO}_4$ ,  $\Delta E_v^O$  is comparable between the ordered and disordered cation structures, at about 1 eV for the O coordinated by 1 Ir. It is not until total delithiation to  $\text{IrO}_4$  that we predict spontaneous oxygen loss. This surprisingly contradicts calculations presented by Jacquet et. al, which predicts oxygen release for the ordered  $\text{LiIrO}_4$ , but not for the fully delithiated  $\text{IrO}_4$ . One possible cause may be their use of PBE and choice not to correct the oxygen reference state. [66]. Our close study of the role of disorder in the  $\text{Li}_x\text{IrO}_4$  system shows the tradeoffs

#### 4.4. High Throughput Screening of $\text{Li}_3\text{MO}_4$ Cathodes

Informed by the previous study of  $\text{Li}_3\text{IrO}_4$ , we will now screen candidate  $\text{Li}_3\text{MO}_4$  cathodes for similar behavior. Our screening approach is fairly simple: we calculate the energies of all  $\text{Li}_3\text{MO}_4$  candidates in the C2/m and P2/c symmetry, as well as a smaller 24 atom SQS structure. We also calculate the energies of  $\text{LiMO}_4$  candidate structures in the lowest energy structures found during the previous delithiation study of  $\text{Li}_3\text{IrO}_4$ , for structures inheriting C2/m, P2/c, and the SQS cation order. Finally, we also calculate the energies of  $\text{Li}_5\text{MO}_4$  structures, using the line ordering as discussed in the previous section. Here,  $M = \text{Ag, Au, Cd, Co, Cr, Cu, Fe, Hf, Hg, Ir, Lu, Mn, Mo, Nb, Ni, Os, Pd, Pt, Re, Rh, Ru, Sc, Ta, Tc, Ti, V, W, Y, Zn, Zr}$ .

The results of the  $\text{Li}_3\text{MO}_4$  and  $\text{LiMO}_4$  structural screens are shown in Fig. 4.13. In these figures, we compute the stability against competing phases, as determined by the OQMD. The structural screen of  $\text{Li}_3\text{MO}_4$  shows a host of ordered structures that may be stable, including  $\text{Li}_3\text{FeO}_4$ ,  $\text{Li}_3\text{OsO}_4$ ,  $\text{Li}_3\text{PtO}_4$ ,  $\text{Li}_3\text{RhO}_4$ ,  $\text{Li}_3\text{RuO}_4$ , and  $\text{Li}_3\text{TaO}_4$ .  $\text{Li}_3\text{TaO}_4$  and  $\text{Li}_3\text{NbO}_4$  are predicted to be within 15 meV of the OQMD convex hull, and have

been previously reported [179, 172].  $\text{Li}_3\text{OsO}_4$  was recently reported in the disordered rocksalt phase [39], while  $\text{Li}_3\text{RuO}_4$  [66] and  $\text{Li}_3\text{FeO}_4$ [175] are also known compounds.  $\text{Li}_3\text{PtO}_4$ ,  $\text{Li}_3\text{RhO}_4$  and  $\text{Li}_3\text{TcO}_4$  have not been reported previously, and the SQS for each of these compositions is also predicted to be comparable to  $\text{Li}_3\text{IrO}_4$ , and merit further investigation. However, the delithiated  $\text{LiMO}_4$  phases for each of these structures is found to be very unstable, unlike  $\text{LiIrO}_4$ , which likely means that the Li cannot be reversibly removed electrochemically. This leaves  $\text{Li}_3\text{OsO}_4$  as an interesting cathode candidate that may be synthesizable in the disordered layer structure.

Average voltages for the lithiation and delithiation  $\text{Li}_3\text{MO}_4$  structures that are within 75 meV of the hull are shown Fig. 4.14. We note that the high voltages corresponding to the delithiation of  $\text{Li}_3\text{MO}_4$  are to the competing phases the OQMD predicts to form at  $\text{MO}_4$ . This introduces a small error in the average voltage for phases that are predicted to form a stable  $\text{LiMO}_4$ , such as  $\text{Li}_3\text{IrO}_4$ ; in this case, the predicted average voltage would be 0.15 eV higher for this first step, before the delithiation step against the formation of  $\text{IrO}_3$  and  $\frac{1}{2}\text{O}_2$ . This high throughput screening screening shows that  $\text{Li}_3\text{OsO}_4$  merits further study, with a voltage plateau useful in battery applications, and similar behavior to  $\text{Li}_3\text{IrO}_4$ .  $\text{Li}_3\text{PtO}_4$ ,  $\text{Li}_3\text{RhO}_4$ , and  $\text{Li}_3\text{TcO}_4$  also show voltage plateaus that would be useful for battery applications, but would require unveiling more intricate delithiation behavior (such as cation migration [173]), as we do not find  $\text{LiMO}_4$  phases of these compositions to be stable.

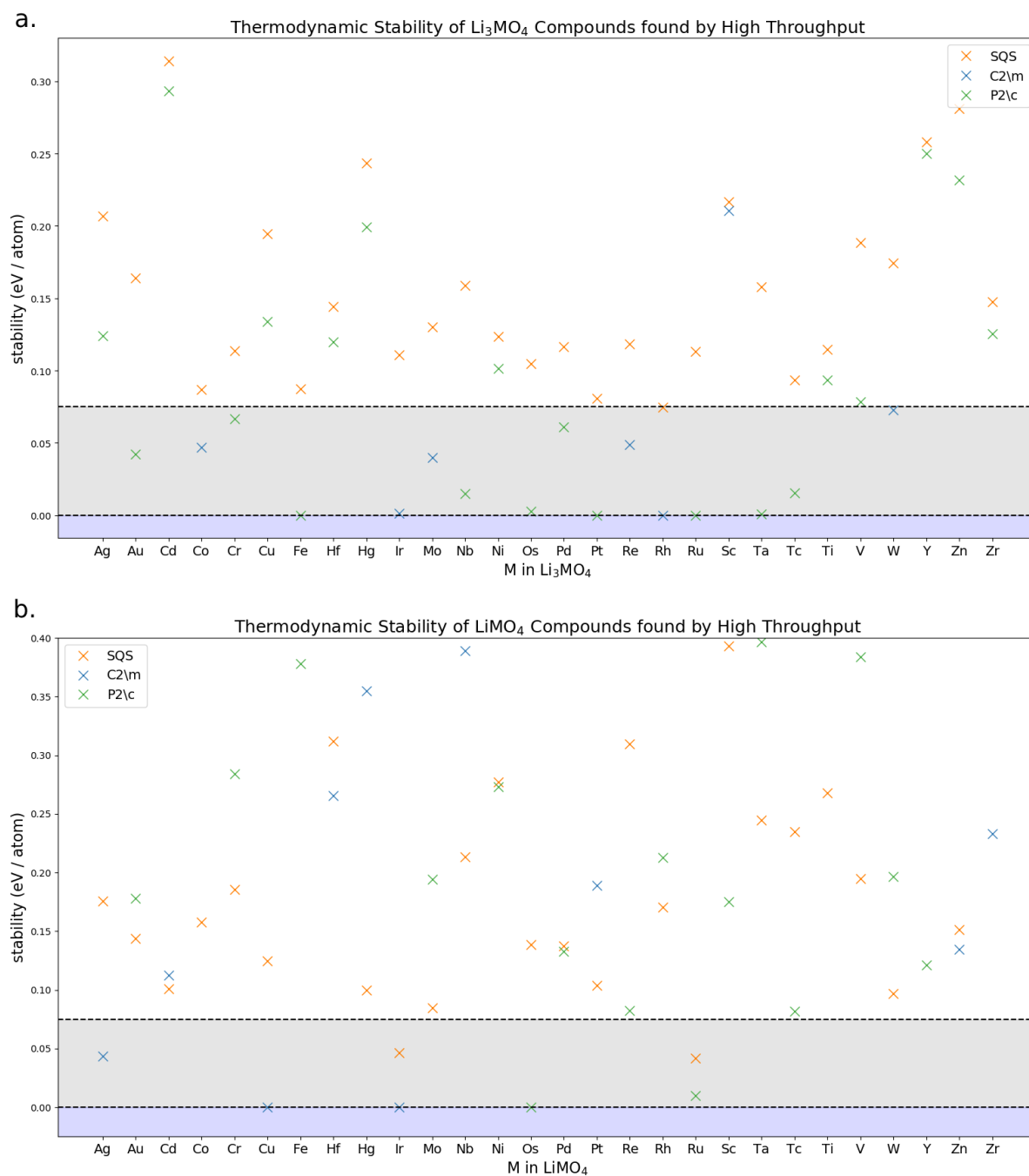


Figure 4.13. Thermodynamic stability of  $\text{Li}_3\text{MO}_4$  and  $\text{LiMO}_4$  candidates assessed during high throughput. Structures on the lower dashed line at 0 eV are predicted to be stable, while those within 75 meV/atom of the OQMD hull are characterized as metastable and potentially synthesizable.

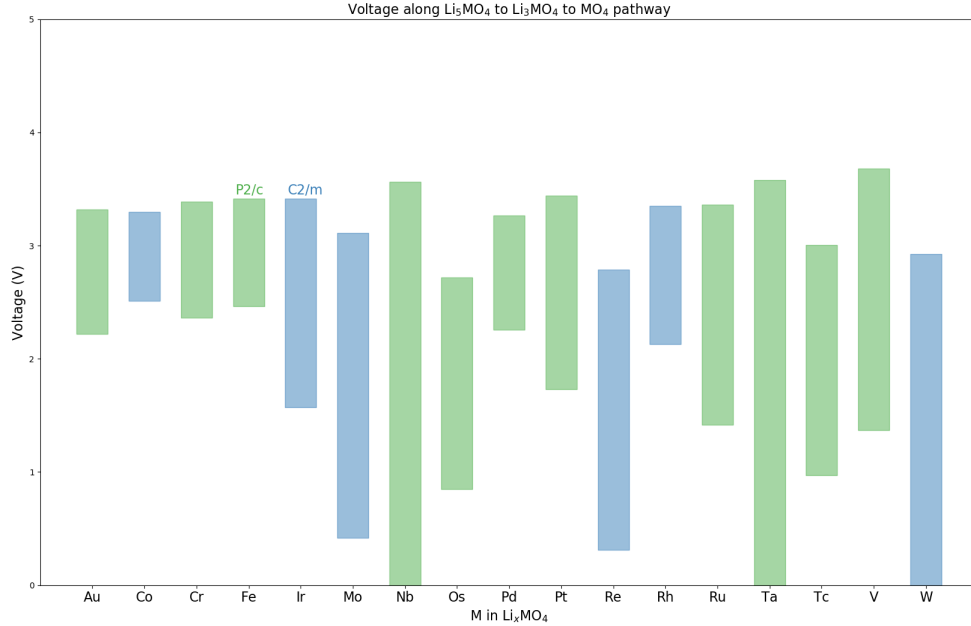


Figure 4.14. Calculated average voltage of  $\text{Li}_3\text{MO}_4$  cathodes as found during high throughput screening. The low voltages correspond to lithiation up to  $\text{Li}_5\text{MO}_4$ , those which are negative are predicted to be unable to incorporate further Li, even without the consideration of competing phases found along delithiation. The high voltage is calculated for the delithiation of  $\text{Li}_3\text{MO}_4$  against the competing phases found at a composition of  $\text{MO}_4$ .

## 4.5. Conclusion

In this chapter, we have discussed the role of cation ordering in  $\text{Li}_3\text{MO}_4$ . We have found that while the fully random disorder captured by the SQS is predicted to be thermodynamically unfavorable, the disordered cation layer enables the formation of oxygen fully coordinated by 6 lithium, which we argue leads to further capability of anionic redox, as shown by changes in the DoS, the magnetization upon delithiation, and the formation of short O-O bonds with antibonding character. Finally, we calculate the oxygen defect

formation energy as the cathode material is delithiated, showing that these oxygen fully coordinated by 6 lithium have low vacancy formation energies, though this is not predicted to be spontaneous. We finish this chapter with a high throughput search, which unveils a few novel candidates that merit further investigation.

## CHAPTER 5

## Phase Transformations and Defects in Zr-H using First-Principles and Machine Learning Interatomic Potentials

*This chapter is adapted from a publication in preparation for submission. Once accepted, permission will be requested*

### 5.1. Introduction

Zirconium alloys are widely used as cladding materials for nuclear fuel rods, due to their low neutron absorption cross section compared to other structural metals. In the high temperature, aqueous environments nuclear fuel rods are exposed to in light water reactors, the corrosion reaction of the alloy with the coolant water leads to the formation of  $\text{ZrO}_2$  as well as  $\text{H}_2$ . A small amount of this produced  $\text{H}_2$  gas is then picked up by the zirconium alloy, occupying interstices [106]. The hydrogen are highly mobile in the alloys, and are responsive to concentration, temperature, and stress gradients, leading to local concentrations that can easily exceed solubility limits, and can lead to precipitation of brittle hydride phases even at elevated operating temperatures in cooler regions. The formation and subsequent cracking of hydrides in the alloy can lead to a cascading cracking mechanism, in which hydrogen in solution will concentrate at the head of a crack tip, forming more of the hydride phase and continuing the cycle [165].

Four key Zr-H phases of interest are present in the Zr-H rich portion of the phase diagram, visualized in Fig. 5.1. Namely, we aim to capture the  $\alpha$ -Zr phase, as well as the

behavior of H tetrahedral and octahedral defects, the tetragonal  $\gamma$ -ZrH phase ( $c > a$ ), the fcc  $\delta$ -ZrH<sub>2-x</sub> phase containing hydrogen-vacancy disorder and most commonly observed in experiment, and the tetragonal  $\epsilon$ -ZrH<sub>2</sub> phase ( $c < a$ ). The  $\gamma$ -ZrH and  $\epsilon$  ZrH<sub>2</sub> are most commonly described as having face-centered tetragonal (fct) symmetry, in analogue to the face-centered cubic  $\delta$ -ZrH<sub>2-x</sub>, though the unit cell can be described more compactly as body-centered tetragonal. We will follow the convention of describing them as fct.

We also highlight some challenges encountered when using atomistic methods to model these phases. Most notably,  $\delta$ -ZrH<sub>2-x</sub> contains intrinsic hydrogen-vacancy disorder, and the fully ordered fcc-ZrH<sub>2</sub> phase is also dynamically unstable against transformations into the fct  $\epsilon$ -ZrH<sub>2</sub> phase. Other candidate cubic structures of  $\delta$ -ZrH<sub>2-x</sub>, such as  $\delta$ -ZrH<sub>1.5</sub> as first studied by Domain et. al [30], are also dynamically unstable against tetragonal distortion. This combination of factors means that there is not a single  $\delta$ -ZrH<sub>2-x</sub> phase with fcc symmetry that is found at 0K, and it is instead stabilized with temperature. We also note that hydrogen-vacancy interactions are important in  $\epsilon$ ZrH<sub>2</sub>, due to their relevancy in determining its stability against the formation of  $\delta$ -ZrH<sub>2-x</sub>. Finally, we note that there are many subtle hydrogen-vacancy effects in the elemental  $\alpha$ -Zr phase, including H congregation in Zr vacancies [100]. In addition, due to the small mass of H, zero point energy and vibrational free energy in general play a significant role in the system, particularly in the consideration of H defects in  $\alpha$ . Thus, the Zr-H system is interesting not only due to its relevance in nuclear systems, but for the intrinsic challenge it presents to probing via atomistics.

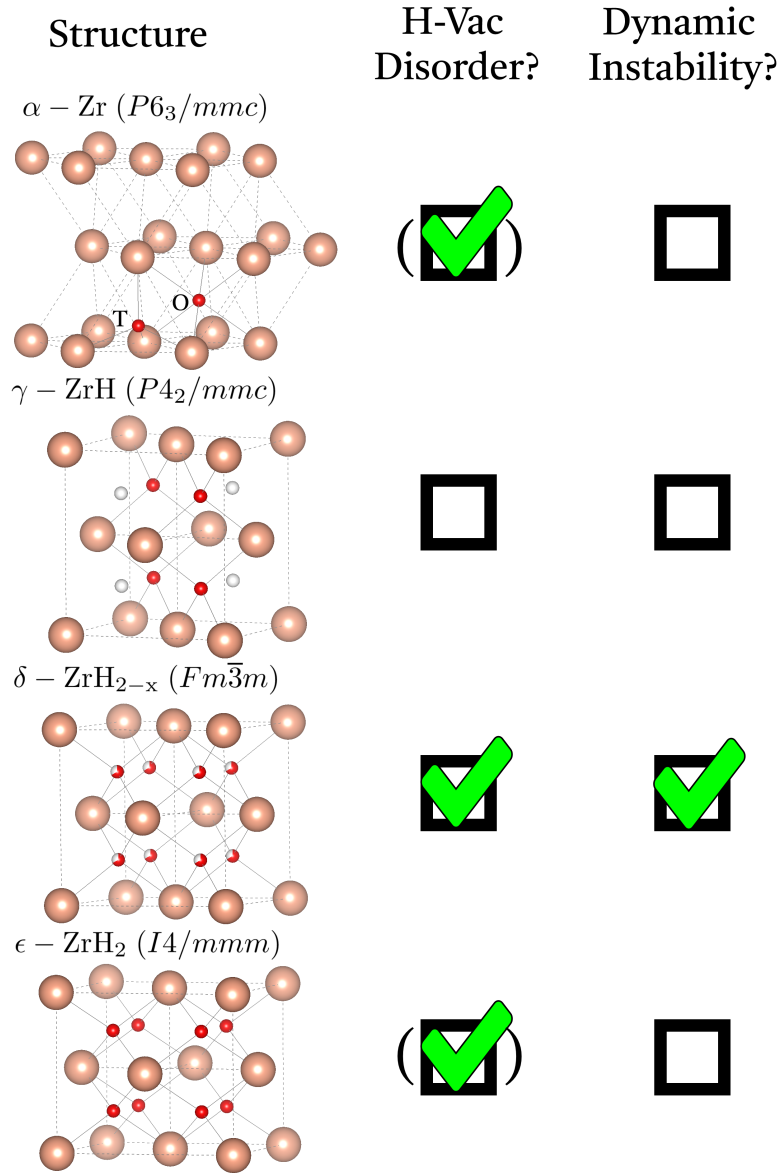


Figure 5.1. Structural schematics of relevant phases in the Zr (peach) - H (red) system, including  $\alpha$ -Zr, showing tetrahedral (T) and octahedral (O) sites,  $\gamma$ -ZrH phase, with H occupying tetrahedral sites in the [110] plane and other tetrahedral vacancies shown in white,  $\delta$ -ZrH<sub>2-x</sub> phase with hydrogen-vacancy disorder on tetrahedral sites, and  $\epsilon$ -ZrH<sub>2</sub> with fully occupied tetrahedral sites. The second column shows that hydrogen-vacancy disorder is critically important in capturing the intrinsically disordered  $\delta$ -ZrH<sub>2-x</sub> phase. The subtleties of the importance of hydrogen-vacancy disorder in the  $\alpha$ -Zr and  $\epsilon$ -ZrH<sub>2</sub> are discussed in the text. We also note that the fcc- $\delta$ -ZrH<sub>2-x</sub> phase is dynamically unstable at 0K. All structural visualizations are drawn in VESTA [104].

Density Functional Theory (DFT) has been the tool of choice among ab-initio atomistic computational methods when studying material phenomena that require high accuracy coupled with computational tractability. DFT is suitable for treating phenomena that can be captured in simulations containing dozens to hundreds of atoms, spanning bulk material phases to relatively simple point and planar defects [99]. In the past couple decades, DFT has been widely used to study the Zr-H system, including H in Zr interstices and bulk hydride phases [30, 114, 161, 18], plane defects including surfaces and interfaces [31, 154, 93], the effect of alloying metals [23], and the behavior of H-Vacancy interactions on the hcp-Zr [58, 57] and fcc-Zr lattices [14, 160]. The hundreds of atoms that DFT is capable of treating cannot capture mesoscopic phenomenon discussed above, motivating the use of empirical potentials that can be used to treat many thousands to millions of atoms. Empirical potentials such as the ZrH-v4 [22], an Embedded Atom Method potential based on the Zr-Zr interactions of Mendeleev-Ackland [101], a Charge Optimized Multi Body (COMB) potential [110], and the recent BMD 19.1 and 19.2 potentials [165] have been used to treat H interstices in Zr. A second COMB potential was introduced to also capture bulk zirconium hydride phases, however it erroneously finds  $\text{ZrH}_2$  to be fcc instead of tetragonal [176], with many  $\delta\text{-ZrH}_{2-x}$  ordered phases found to be on the convex hull. The dominant phase found in experiment and when studying hydrides found in used cladding materials, the  $\delta\text{-ZrH}_{2-x}$  phase, is of particular interest in modeling with an empirical potential, as it does not form a single ordered phase at 0K. Instead, it's formation competes with  $\epsilon\text{-ZrH}_2$ ; the phase boundary between these two structures shows an increasing transformation temperature with increased H content. Capturing the

temperature and composition dependence requires a potential that accurately models the vibrational and hydrogen-vacancy configurational properties.

Machine learning potentials (MLP) are growing in popularity as a means of capturing the high chemical accuracy of DFT, but with the tractability of empirical potentials. MLP, lacking a rigid functional form, are capable of capturing a wider variety of structural configurations and symmetries than a single empirical potential [11, 108]. Behler-Parrinello were the first to develop machine learning interatomic potentials, using neural network potentials (NNP) coupled with a local descriptor of atomic environments to model molecular systems [12]. Since then, numerous new MLP have been introduced, most prominently Gaussian approximation potentials (GAP)[10], and spectral neighbor analysis potentials (SNAP),[149]. MLP are typically trained on ab-initio data of the energy, forces, and stresses of a given geometry of atoms, and map these values onto a set of local descriptors of atomic environments. Careful consideration of the intended application of the MLP is thus critical in determining the contents of the training set, as they may lack transferability to atomic environments that are outside the scope of the training set. MLP have been used to study the zirconium system, including its mechanical properties [92], the  $\alpha$  to  $\omega$  [182] and  $\alpha$  to  $\beta$ [91] phase transformations, as well as phase transformations in  $\text{ZrO}_2$  [158], but have as of yet not been applied to the study of hydrides.

Here, we will develop a Zr-H moment tensor potential (MTP), a class of MLP, which represent interatomic interactions on a polynomial-like basis set [136, 121]. MTP have been used to produce Ag-Pd alloy phase diagrams [124], search for novel phases in Cu-Pd, Co-Nb-V, and Al-Ni-Ti systems [50], study vacancy diffusion in metals [113], and high temperature elastic behavior in  $\beta$ -Ti [137]. The demonstrated capability of MTP to

capture phase transformations, mixing behavior, diffusion, and elastic behavior, combined with the favorable low-cost and high accuracy of MTP, make the method appealing for studying the Zr-H system. We will train a novel MTP to study the Zr-H system, first focusing on its ability to capture phase transformations, and then finally validating its use on other properties of interest, including H diffusion, H-vacancy ordering, and defect properties.

The trained MTP captures lattice and elastic constants in excellent agreement with DFT, but it does not capture the predicted dynamic instability of  $\delta$ -ZrH<sub>2</sub>. Similarly, it calculates a modeled solvus boundary in excellent agreement with DFT, though both under predict experiment by about 200 K. It also captures the experimental behavior that increasing H concentration increases the phase transformation temperature between  $\epsilon$ -ZrH<sub>2</sub> to  $\delta$ -ZrH<sub>2-x</sub>. Considering defects, it reproduces 0K migration barrier heights for T-T, T-O, and O-O transitions by 20 meV, 3 meV, and 25 meV, when compared with DFT. The MTP captures the diffusion of H in  $\delta$ -ZrH<sub>2-x</sub> as having an activation energy within 0.01 eV of experiment. Of the other point and planar defects explored, all are well reproduced vs. DFT, except for the basal stacking fault energy, which is underpenalized by the MTP.

## 5.2. Methods

### 5.2.1. Density Functional Theory Calculations

Density functional theory (DFT) calculations were carried out using the Vienna Ab-Initio Simulation Package (VASP) [83, 84, 81, 82]. The following settings were used for all DFT calculations presented in this work. We use Projector Augmented-Wave potentials

[16, 85], within the Perdew-Burke-Ernzerhof formulation of the Generalized Gradient Approximation [119], with Zr valence electrons including 4s. A k-point mesh with a minimum density of  $0.15 \text{ \AA}^{-1}$  centered at  $\Gamma$  was used to sample the Brillouin zone, and the planewave cutoff was set to 400 eV. Gaussian smearing with a width of 0.05 eV was used, and the precision was set to Accurate.

### 5.2.2. Active Learning of Moment Tensor Potentials and Description of Training Sets

We have used Moment Tensor Potentials (MTP) to model Zr and Zr-H interactions, as implemented in the MLIP package [112], the formalism for which we will briefly describe here. MTPs represent the total energy of a system,  $E$ , as the sum of local contributions for each atom in the system,  $V(\mathbf{n}_i)$ , depending on  $(n_i)$ , the neighborhood of an atom  $i$  within the potential cut-off distance, represented by a set of vectors.

$$(5.1) \quad V(\mathbf{n}_i) = \sum_{j=1}^m \xi_j B_j(\mathbf{r}_i)$$

Here,  $\xi_j$  are coefficients found by minimizing the root mean square prediction error of energy, forces, and stresses against the DFT data set, each given a predetermined weight as input.  $B_j$  are the set of predefined basis functions, further information for which can be found here [112]. The functional form of the basis set defines a level of moments, increasing which increases the size of the basis set, in terms of radial and angular contributions. In recognizing the importance of the quality of the training set, MLIP also implements

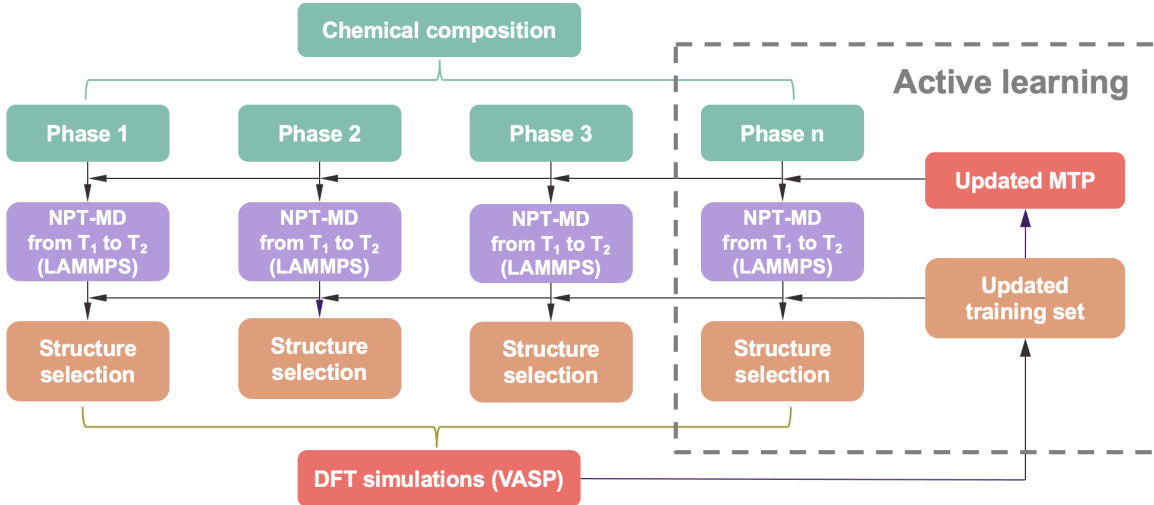


Figure 5.2. Flowchart of the process for training MTP using active learning for simulating structural phase transformations containing training sets for  $n$  phases. The dashed box constitutes a unit in which active learning occurs to iteratively provide new training examples. The NPT-MD steps consist of heating or cooling across a temperature range of interest.

an active learning scheme [122, 51, 52, 112], thus enabling effective selection of configurations for accurate interpolation. The active learning scheme adopts a special form of query strategy, known as the D-optimality criterion [51], which employs the so-called extrapolation grade  $\gamma$  based on a geometric criterion.  $\gamma$  is calculated by determining the most linearly independent set of structures already in the training set, and assessing the amount by which a candidate structure will increase the determinant (see more details in Ref. [122, 51, 52, 112] (see more details in Ref. [122, 51, 52, 112])).

Inspired by the on-the-fly MLP implemented in VASP [70], here we devise a semiautomatic algorithm to build training structures for MTP for materials systems with multiple structures and phases by taking advantage of the already implemented active learning scheme within MLIP. One advantage of our strategy is that it does not require explicit ab-initio molecular dynamics (AIMD) simulations, which are often time-consuming and

performed with low accuracy. This is achieved by (i) generating a seed MTP, either using lattice dynamics information from phonon calculations, or elastic constant and bulk modulus calculations, and (ii) iteratively refining the MTP by adding training structures evaluated by a DFT and selected from LAMMPS-MD simulations (run using an MTP) via active learning, the latter step resembling the on-the-fly-learning strategy. The complete schematic is displayed in Fig. 5.2. Specifically, we proceed with the construction of MTP as follows:

- I. Identify various phases involved during the structural phase transformation for given chemical composition. These may include bulk phases, but could also include structures relevant to the thermodynamics of phase transformations, such as dilute point defects or interfaces.
- II. Compute a simple initial training set to form the basis of a seed interatomic potential. Examples of relevant information that may be used to form a seed potential include supercell structures generated from the frozen phonon method, or structures generated while calculating elastic constants and bulk modulus.
- III. Perform NPT-MD simulations for each phase using LAMMPS for a wide temperature range covering the structural phase transformation, using the MTP.
- IV. Select training structures from the configurations generated in (3) using the active learning scheme available within MLIP.
- V. Calculate the selected structures using VASP with high convergence thresholds and retrain MTP after updating the training set with newly computed structures.
- VI. Iterate steps from (3) to (5) (an iteration of which we call an epoch) until no new structures are selected by active learning.

We find it necessary and advantageous to perform NPT-MD simulations using LAMMPS through a heating process in step (3) instead of NVT-MD. It is because if the structural phase transformation occurs at relatively high temperatures, thermal expansion effects would be crucial while the isothermal-isobaric ensemble can naturally capture these effects. We also find that the NPT-MD simulations need not be lengthy, as long as they approximately cover the volume changes and magnitudes of atomic displacements in the targeted temperature range. Furthermore, a typical time scale ranging from 50 ps to 100 ps with a time step of 0.5 fs works well.

The trained potential presented here focuses on providing a proof of concept of the ability of MTP to capture multiple phase transformations, and thus the training set is targeted towards capturing bulk energetics and lattice dynamics of relevant phases. For each of the desired phases in the training set, we iterate through our active learning scheme, refining the trained potential each epoch. We continue this until no new phases are found during NPT MD, while setting the extrapolation grade  $\gamma_{threshold}=5$ .  $\gamma_{threshold}$  is a metric for estimating the amount of new geometric information a structure adds to the training set, based on the D-Optimality criterion. For a full treatment please refer to Ref. [112]. We use the Zr-ZrH<sub>x</sub> MTP to predict phase transformations at the solvus boundary between  $\alpha$ -Zr and the model  $\gamma$ -ZrH phase, and use MD simulations to capture the temperature and composition dependence of the  $\epsilon$  and  $\delta$ -ZrH<sub>2-x</sub> transformation.

For the Zr-ZrH<sub>x</sub> MTP, the training set includes the following:

- structures used to fit elastic constants and bulk modulus values of:
  - $\alpha$ -Zr (2 atoms, 35 total structures)
  - dilute H in tetrahedral site of  $\alpha$ -Zr (37 atoms, 45 total structures)

- dilute H in octahedral site of  $\alpha$ -Zr (37 atoms, 45 total structures)
- $\gamma$ -ZrH, (12 atoms, 45 total structures)
- $\delta$ -ZrH<sub>2</sub> (12 atoms 28 total structures)
- $\epsilon$ -ZrH<sub>2</sub> (12 atoms in 45 total structures)
- NPT molecular dynamics snapshots for bulk phases, carried out until no new phases were added during active learning:
  - $\alpha$ -Zr (36 atoms, 303 structures from 3 epochs, heating from 100K to 1000K)
  - dilute H in tetrahedral site of  $\alpha$ -Zr (37 atoms, 556 total structures over 3 epochs, heating from 100K to 1000K)
  - dilute H in octahedral site of  $\alpha$ -Zr (37 atoms, 481 total structures over 3 epochs, heating from 100K to 1000K)
  - $\gamma$ -ZrH, (64 atoms, 449 total structures over 3 epochs, heating from 100K to 1000K)
  - $\delta$ -ZrH<sub>2</sub> (96 atoms, 203 total structures from 2 epochs, cooling from 1000K to 100K)
  - $\epsilon$ -ZrH<sub>2</sub> (96 atoms in 191 total structures from 2 epochs, heating from 100K to 1000K)
- NPT molecular dynamics snapshots for accessory phases and defects, carried out for a single epoch:
  - ZrH orthorhombic competing phase (32 atoms in 259 total structures, heating from 100K to 1000K)
  - ZrH fcc competing phase (64 atoms in 69 structures, heating from 100K to 1000K)

- ZrH bcc competing phase (64 atoms in 30 total structures, heating from 100K to 1000K)
- Zr fcc competing phase (32 atoms in 42 total structures, heating from 100K to 1000K)
- Zr basal surface (54 atoms in 11 total structures, heating from 100K to 1000K)
- Zr vacancy (35 atoms in 56 total structures, heating from 100K to 1000K)
- ZrH (111) surface (80 atoms in 23 total structures, heating from 100K to 1000K)
- Zr(001)-ZrH(111) interface (48 atoms in 73 total structures, heating from 100K to 1000K)
- $\delta$ -ZrH<sub>1.66</sub> (96 atoms in 80 total structures, cooling from 1000K to 100K)

The first 4 accessory phases are included to provide information on low energy phases that may be accessed during MD. The next four accessory phases are defects that we would like the MTP to describe well. The final accessory phase provides some information on the hydrogen-vacancy ordering at the composition close to the  $\delta$ -ZrH<sub>2-x</sub> to  $\epsilon$ -ZrH<sub>2</sub> phase boundary. The training information is summarized in Table 5.1.

### 5.2.3. Suppression of lost atoms during high temperature molecular dynamics

The flexibility of the functional form of MTP, and MLP in general, come with the drawback of potential non-physical interactions when relevant training examples are not in the training set. For the work presented here, we observed this in form of a strong non-physical attraction of H-H in short pair distances of  $< 1 \text{ \AA}$ , interactions which were not

Table 5.1. Summary of training information for the MTP presented in this work.

Training Information	Zr-ZrH <sub>x</sub>
LAMMPS-MD	NPT
Ensemble	
Temperature (K)	100K to 1000 K
Length (ps)	2.5
Step (fs)	0.25
MTP-AL	
# of epochs	2-3
# of structures	3069
Level of Moments	22
Training RMS Error	
Energy (meV/atom)	2.24
Force (eV/Å)	0.056
Stress (kBar)	1.770

probed by our training set but did occasionally lead to lost atoms during MD simulations above 900K when studying the  $\delta$ -ZrH<sub>2-x</sub> and  $\epsilon$ -ZrH<sub>2</sub> phases. The nearest H-H distances in these structures, at equilibrium, are 2.2-2.3 Å, so these interactions are quite rare during molecular dynamics, but still must be suppressed. When necessary, we have achieved this by overlaying a Ziegler-Biersack-Littmark (ZBL) style potential [181], using values of 6.0 and 40.0 for  $Z_H$  and  $Z_{Zr}$  respectively, with inner and outer cutoff distances of 0.01 and 1.0 Å. This is achieved using the *pair\_style hybrid/overlay* command in LAMMPS, which simply adds the ZBL potential to the MTP. The H-H pair interaction is shown in Fig. 5.3, with and without the ZBL applied. We will show that, because these interaction distances are rarely seen during MD, the addition of the ZBL does not change thermodynamic properties such as equilibrium lattice constants, or diffusion behavior.

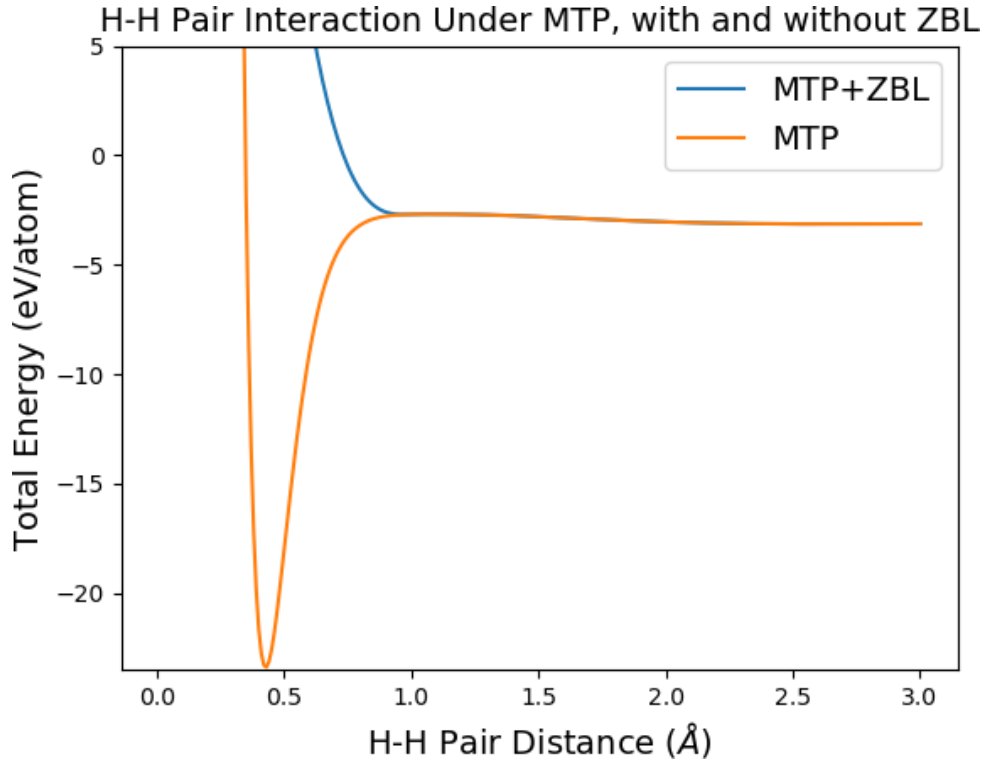


Figure 5.3. H-H Pair interaction, under the trained MTP and with an overlaid ZBL interaction to suppress the spurious attraction under 1 Å. The inclusion of the ZBL is required when close H-H interactions are probed during high temperature MD in H-saturated phases.

### 5.3. Results: Bulk and Vibrational Properties, and Phase Transformations in Zr-H

Results will be structured as follows. First, we will compare bulk and vibrational properties calculated using DFT and MTP, including lattice parameter, elastic constants, phonon dispersion, and Bain path distortions at ZrH and ZrH<sub>2</sub> compositions. Then, we will consider phase transformations, starting with the first-order phase transformation between  $\alpha$ - and  $\beta$ -Zr before moving onto the Zr-H system. Within the Zr-H system, we will treat the solvus boundary between  $\alpha$ -Zr and the ordered  $\gamma$ -ZrH model hydride phase,

and then the phase transformation between  $\delta$ -ZrH<sub>2-x</sub> and  $\epsilon$ -ZrH<sub>2</sub>. After treating phase transformations, we will then validate the use of the Zr-H potential (which we have named Zr-ZrH<sub>x</sub> MTP), for various properties related to phase transformations. These include H-vacancy ordering in  $\delta$ , H diffusion in  $\alpha$  and  $\delta$ , and finally defects in Zr, including point defects, surfaces, and the interface with  $\gamma$ -ZrH.

### 5.3.1. Comparison of calculated bulk properties between DFT and trained MTP

**5.3.1.1. Lattice and elastic constants of bulk phases.** Table 5.2 summarizes the lattice constants and elastic behavior of the pure  $\alpha$ -Zr phase and ordered hydride phases, both calculated using DFT and the trained MTP presented in this work, and experiment when available. Lattice constants predicted by the MTP are in excellent agreement with DFT, however there is some inaccuracies in capturing the elastic behavior of the hydride phases, especially the two ZrH<sub>2</sub> phases. We have also used NPT MD to estimate the thermal expansion coefficients of a and c in Zr, respectively at  $6.7 \times 10^{-6}/\text{deg}$  and  $7.95 \times 10^{-6}/\text{deg}$ , compared to  $5.5 \times 10^{-6}/\text{deg}$  and  $10.8 \times 10^{-6}/\text{deg}$  as measured experimentally [139].

**5.3.1.2. 0 K Energetics of Bulk Phases.** In order to capture the relevant bulk energetics in Figure. 5.4, we plot the Zr and ZrH<sub>2</sub> convex hull calculated using DFT and the trained MTP. We set the chemical potentials of  $\mu_{\text{Zr}}$  and  $\mu_{\text{H}}$  by solving the following system of equations:

Table 5.2. Comparison of equilibrium lattice parameters and elastic constants using VASP-PBE (this work) and the trained MTP. We compare with results from two theoretical results from the literature, the first using PBE within VASP as well [22], and the other using PBE within the GPAW package [18]. Experimental lattice parameters for  $\alpha$ -Zr,  $\gamma$ -ZrH, and  $\epsilon$ -ZrH<sub>2</sub> are taken from Zuzek et al [184], while the experimental  $B_v$  of  $\alpha$ -Zr is from Fisher et al [41]. We note excellent agreement between our DFT calculated lattice parameters and those calculated under the MTP. The largest deviation is in the a lattice parameter of  $\gamma$ -ZrH, at about 0.35. Elastic properties are reported in GPa. More significant deviations exist in the elastic properties. The properties of  $\alpha$ -Zr are very well reproduced, while the  $\gamma$ -ZrH phase is predicted to have a slightly harder bulk modulus under the trained MTP than DFT, and slightly softer shear and Young’s moduli. The two ZrH<sub>2</sub> phases offer a more complex potential energy surface due to the dynamic instability of the  $\delta$ -ZrH<sub>2</sub> phase, which the trained MTP is, unsurprisingly, not fully able to capture.

Phase	Method	a	c	c/a	C <sub>11</sub>	C <sub>33</sub>	C <sub>12</sub>	C <sub>13</sub>	C <sub>44</sub>	C <sub>66</sub>	B <sub>v</sub>	G <sub>v</sub>	E <sub>v</sub>
$\alpha$ -Zr	VASP-PBE	3.23	5.16	1.59	136.40	153.94	73.32	67.01	25.30	31.54	93.49	31.05	83.88
	Blomqvist	3.24	5.16	1.59	157.00	158.00	51.00	62.00	15.00	44.00	91.33	34.60	92.16
	Christensen										96.00	33.00	88.82
	Zr-ZrH <sub>x</sub> MTP	3.23	5.16	1.60	130.24	184.24	78.89	62.33	24.92	25.68	94.65	31.18	84.29
	Experiment	3.23	5.15	1.59	155.00	173.00	67.00	65.00	36.00	44.00	97.44	42.27	110.78
$\gamma$ -ZrH	VASP-PBE	4.58	5.03	1.10	122.62	183.96	118.17	95.70	49.97	64.91	116.48	40.95	109.95
	Blomqvist	4.59	5.00	1.09	131.00	176.00	123.00	92.00	64.00	75.00	116.89	49.33	129.75
	Christensen										113.00	25.00	69.85
	Zr-ZrH <sub>x</sub> MTP	4.57	5.02	1.10	141.07	185.89	140.99	116.81	38.65	56.26	135.25	32.94	91.40
	Experiment	4.596	4.97	1.08									
$\epsilon$ -ZrH <sub>2</sub>	VASP-PBE	5.00	4.40	0.88	174.92	158.77	148.55	103.42	32.05	64.47	135.49	35.93	99.03
	Blomqvist	5.00	4.43	0.89	156.00	132.00	144.00	107.00	40.00	60.00	128.89	33.73	93.08
	Christensen										130.00	24.00	67.83
	Zr-ZrH <sub>x</sub> MTP	4.99	4.41	0.88	176.77	146.65	145.64	123.34	58.43	65.79	142.76	43.72	119.01
	Experiment	4.975	4.45	0.89									
$\delta$ -ZrH <sub>2</sub>	VASP-PBE	4.80	4.80	1.00	73.82	73.82	164.43	164.43	-49.56	-49.56	134.23	-47.86	-162.94
	Christensen										132.00	-66.00	-238.00
	Zr-ZrH <sub>x</sub> MTP	4.80	4.80	1.00	109.91	109.91	128.18	128.18	35.79	35.79	122.09	17.82	50.98

$$(5.2) \quad \mu_{Zr} = E_{\alpha-Zr}$$

$$(5.3) \quad \mu_{Zr} + 2\mu_H = E_{\epsilon-ZrH_2}$$

Here,  $E_{\alpha-Zr}$  and  $E_{\epsilon-ZrH_2}$  are energies per formula unit. These reference chemical potentials are used to calculate the formation energy per atom of each phase. For an arbitrary  $Zr_aH_b$  the formation energy  $\Delta E$  is calculated as

$$(5.4) \quad \Delta E_{Zr_aH_b} = \frac{E_{Zr_aH_b} - a\mu_{Zr} - b\mu_H}{a + b}$$

This choice of chemical potentials corresponds to the coexistence of  $\alpha$ -Zr and  $\epsilon$ -ZrH<sub>2</sub>, and is thus relevant for the conditions leading to hydride formation in Zr fuel cladding. In addition to the bulk phases we have discussed so far, we include the ordered fcc ZrH<sub>1.5</sub> introduced by Domain et al [30] that is commonly used as a proxy for the cubic ZrH<sub>2-x</sub> phase. We also plot the formation energies of special quasi-random structures [183] (SQS), which capture disordered phases in finite computational cells. Here, we use SQS to account for hydrogen-vacancy disorder in hydride phases. SQS were generated using the *mcsqs* [157] code within the Alloy Theoretic Automated Toolkit (ATAT) package [155]. Pair, triplet, and quadruplet interactions were set to a cutoff distance of 6 Å and a maximum number of atoms set to 64. SQS were generated corresponding to ZrH, ZrH<sub>1.5</sub>, ZrH<sub>1.6</sub>, ZrH<sub>1.66</sub>, and ZrH<sub>1.75</sub>, corresponding to 42, 20, 26, 46, and 22 atoms.

The convex hull construction is the starting point for understanding the thermodynamics of phase stability in the Zr-H system. At 0 K, and without accounting for zero point energy, we predict the formation of a pure  $\gamma$ -ZrH phase, though with very low driving force as the formation energy just -1 meV. The trained MTP is able to nearly match the predicted formation energy of  $\gamma$ -ZrH under DFT. The SQS phases offer a rough

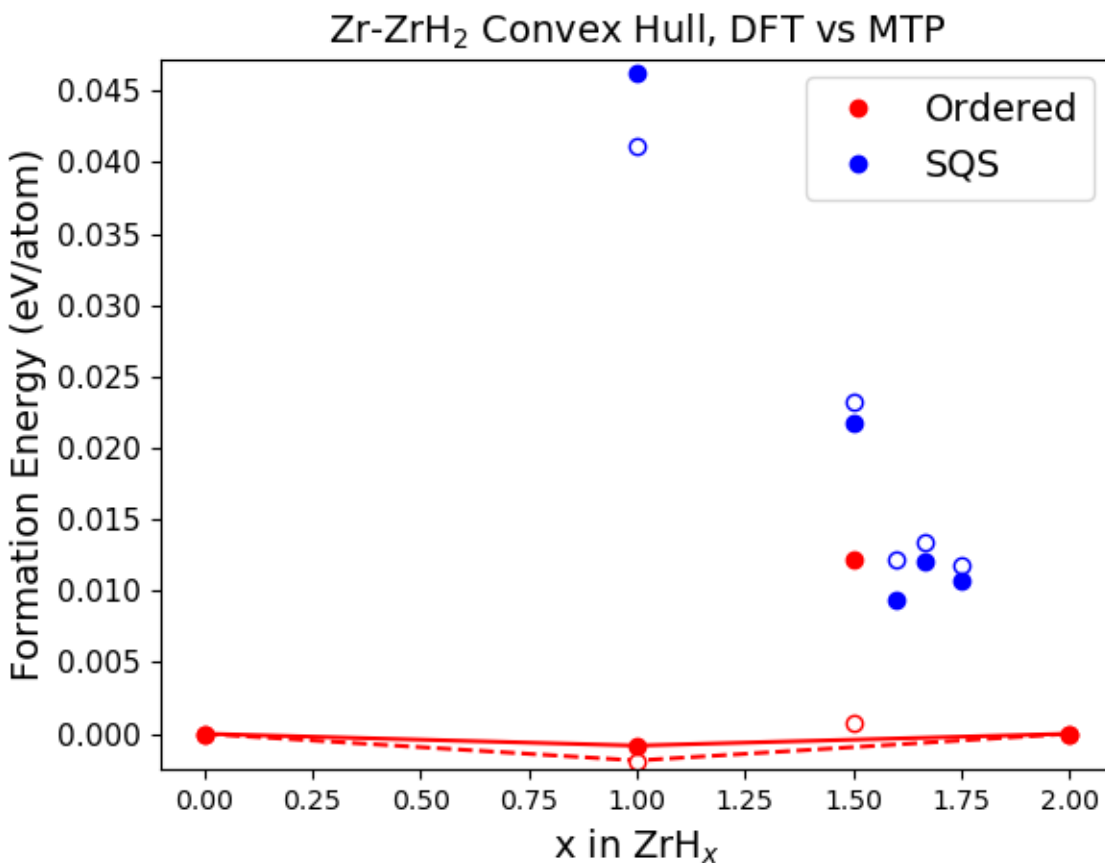


Figure 5.4. Convex Hull of formation energies, as calculated in Equation 5.4, against the formation of Zr and ZrH<sub>2</sub>. Solid markers indicate values from DFT calculations, while empty markers indicate values calculated under the MTP. Red circles indicate ordered phases, while blue circles indicate special quasi-random structures, which approximate hydrogen-vacancy disorder. At a temperature of 0K and ignoring zero point energy, we predict  $\gamma$ -ZrH to be a stable equilibrium phase, nearly degenerate in energy with the formation of Zr + ZrH<sub>2</sub>. The low energy of the disordered SQS phases between  $1.5 \leq x \leq 1.75$  indicates the low barrier to the stability of the  $\delta$ -ZrH<sub>2-x</sub> phase with increasing temperature, accessible by a combination of vibrational and configurational entropy. MTP shows a fairly strong agreement with DFT especially across disordered phases. The strongest disagreement is the over-stabilization of the cubic ZrH<sub>1.5</sub> phase.

quantification of the barrier to formation of the  $\delta$ -ZrH<sub>1.6</sub> to ZrH<sub>1.75</sub> phases. At 0 K, these SQS have a formation energy between 10-15 meV/atom under DFT and 15-20 meV/atom under the trained MTP, in reasonable agreement. The ordered model  $\delta$ -ZrH<sub>1.5</sub> phase is lower in energy under MTP by about 10 meV/atom, which we expect would suppress the transformation temperature under MTP of  $\epsilon$ ZrH<sub>2</sub> to  $\delta$ ZrH<sub>2-x</sub>. The strong agreement between MTP and DFT in this composition range indicates an ability for the MTP formalism to accurately interpolate between ZrH and ZrH<sub>2</sub>, based on the Hydrogen-Vacancy information from high temperature ZrH NPT snapshots.

The epitaxial Bain path (EBP) is of interest when studying tetrahedral and cubic phase transformations, making them a useful testcase for testing the ability of our trained MTP to capture hydride behavior. The EBP corresponds to varying biaxial stress in the (001) plane of the phase of choice, while allowing for relaxation along the perpendicular direction  $\langle 100 \rangle$  path. The EBP for ZrH (with the hydrogen ordering corresponding to the  $\gamma$ -ZrH phase) and ZrH<sub>2</sub> are shown in Figs. 5.5 and 5.6. For both Bain paths, we show the total energy per atom, plotted vs. the  $c/a$  ratio and as a ratio of the lattice parameter over the equilibrium lattice parameter. For the ZrH composition, we see maximal deviation of about 0.15 eV/atom. We also observe an inability for the trained MTP to capture the subtleties of the potential energy landscape, as it shows a purely monotonically increasing second derivative with distance from the minima in either plot. Under DFT, the second derivative changes sign around a  $c/a$  ratio of 0.9, however neither predicts a stable cubic phase or another minima besides  $\gamma$ -ZrH. The ZrH<sub>2</sub> EPB shows the  $\epsilon$  phase at the minimum of both plots, the  $\delta$  phase at the local maximum, and a third tetrahedral phase with a  $c/a$  ratio  $> 1$ . However, the cubic phase is significantly more stable under the trained MTP

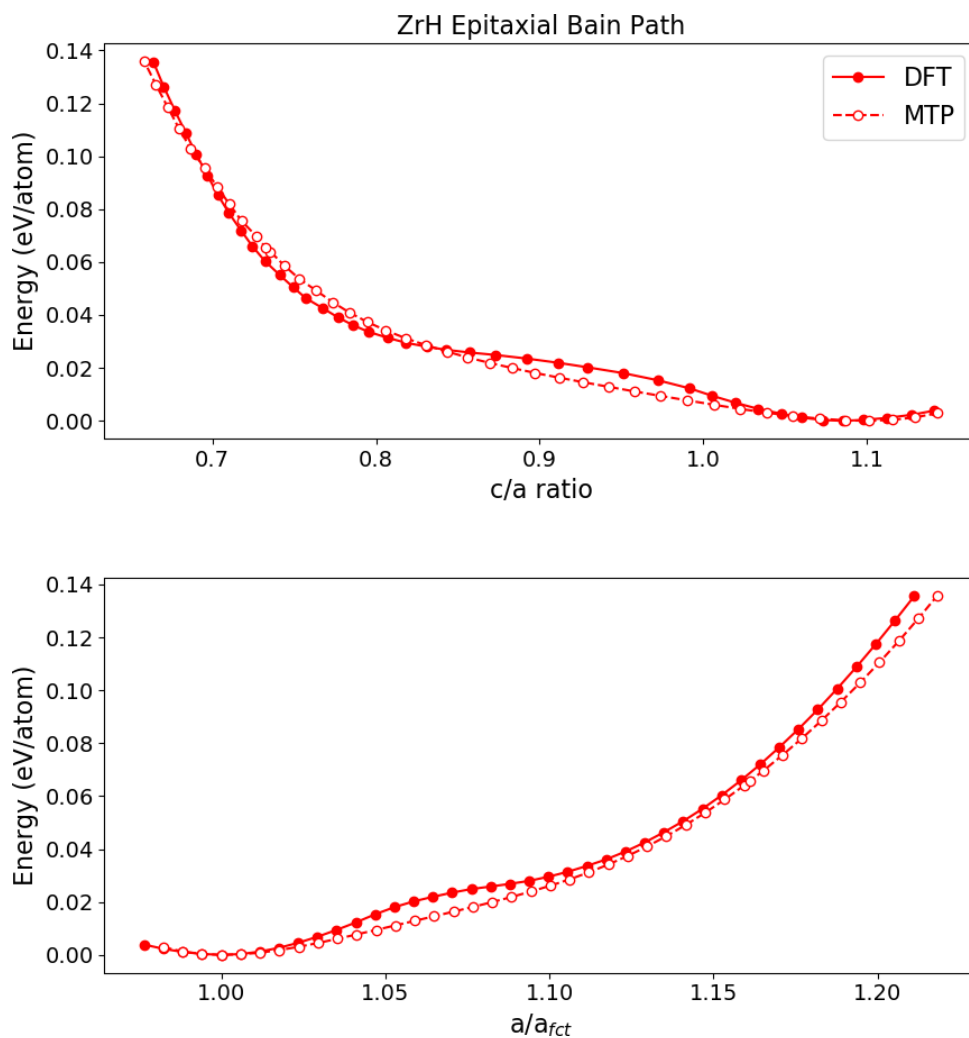


Figure 5.5. ZrH epitaxial Bain path

than DFT, at about 12 meV vs. 5.5 meV, so the local maximum it sits at is very subtle and nearly degenerate in energy with the tetragonal phase with  $c/a$  ratio  $>1$ . This phase may be synthesizable by introducing an epitaxial strain by growing  $\text{ZrH}_2$  on a suitable substrate.

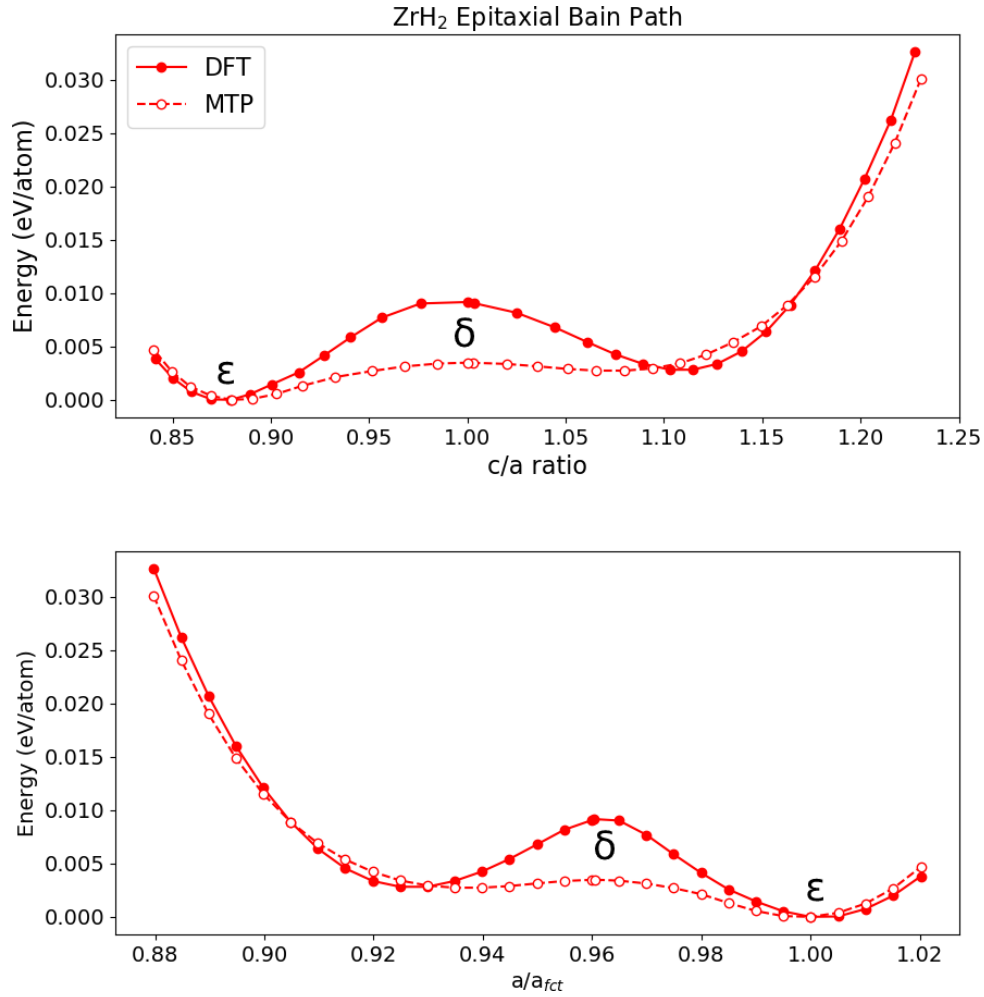


Figure 5.6. ZrH<sub>2</sub> epitaxial Bain path. The most notable feature is the lower energy of the metastable fcc  $\delta$  phase.

### 5.3.2. Vibrational Properties and Finite Temperature Thermodynamics

We use the Parlinski-Li-Kawazoe frozen phonon method [118] as implemented in the phonopy package to calculate phonon dispersions and density of states within the harmonic approximation, using both DFT and our trained MTP [150]. Dispersion and density of states are shown in Fig. 5.7. We use a 4x4x4 supercells for  $\alpha$  for a total of 128 atoms, a 3x3x3 supercell of  $\gamma$ -ZrH for a total of 216 atoms, and 2x2x2 supercells of

the  $\text{ZrH}_2$  phases, which total 96 atoms. The two  $\alpha$ -Zr defect cells contain 36 Zr atoms and 1 H atom, and we use the same size cell for supercell calculations. In general, we see excellent agreement between DFT and our trained MTP, in both dispersion behavior and density of states.

Previous theoretical treatments have attempted to address the significant effect of anharmonicity in the vibrational properties of dilute hydrogen in  $\alpha$ -Zr. These treatments ascribe all significant vibrational behavior to the light H atom, while fixing the Zr atoms which vibrate at lower frequencies and therefore may contribute less significantly to the vibrational free energy. Christensen and colleagues only treat the anharmonicity of the H defect in a tetrahedral site [22], by decomposing the vibrations of the dilute H atom into a harmonic mode parallel to the basal plane, and then add the contribution of the anharmonic double-well potential between neighboring tetrahedral sites by solving the 1-D Schrodinger equation, in the two limiting cases of freezing Zr atoms corresponding to the equilibrium H position, and freezing Zr atoms while H is in the transition state. In their calculations, the fully harmonic treatment makes the octahedral site lower in energy than the tetrahedral by 40 meV. Using their approach, the tetrahedral site remains preferred across the temperature range, in agreement with experiment.

Christensen and colleagues claim that the octahedral site is well described by the fully harmonic treatment. However, we have calculated the transition pathway between tetrahedral and octahedral sites, as well as between two octahedral sites using Nudged Elastic Band (NEB), and our results show significant anharmonicity for these sites as well, in addition to the well established anharmonicity in the tetrahedral-tetrahedral transition. These transition pathways are shown in Fig. 5.8 and the calculations details discussed

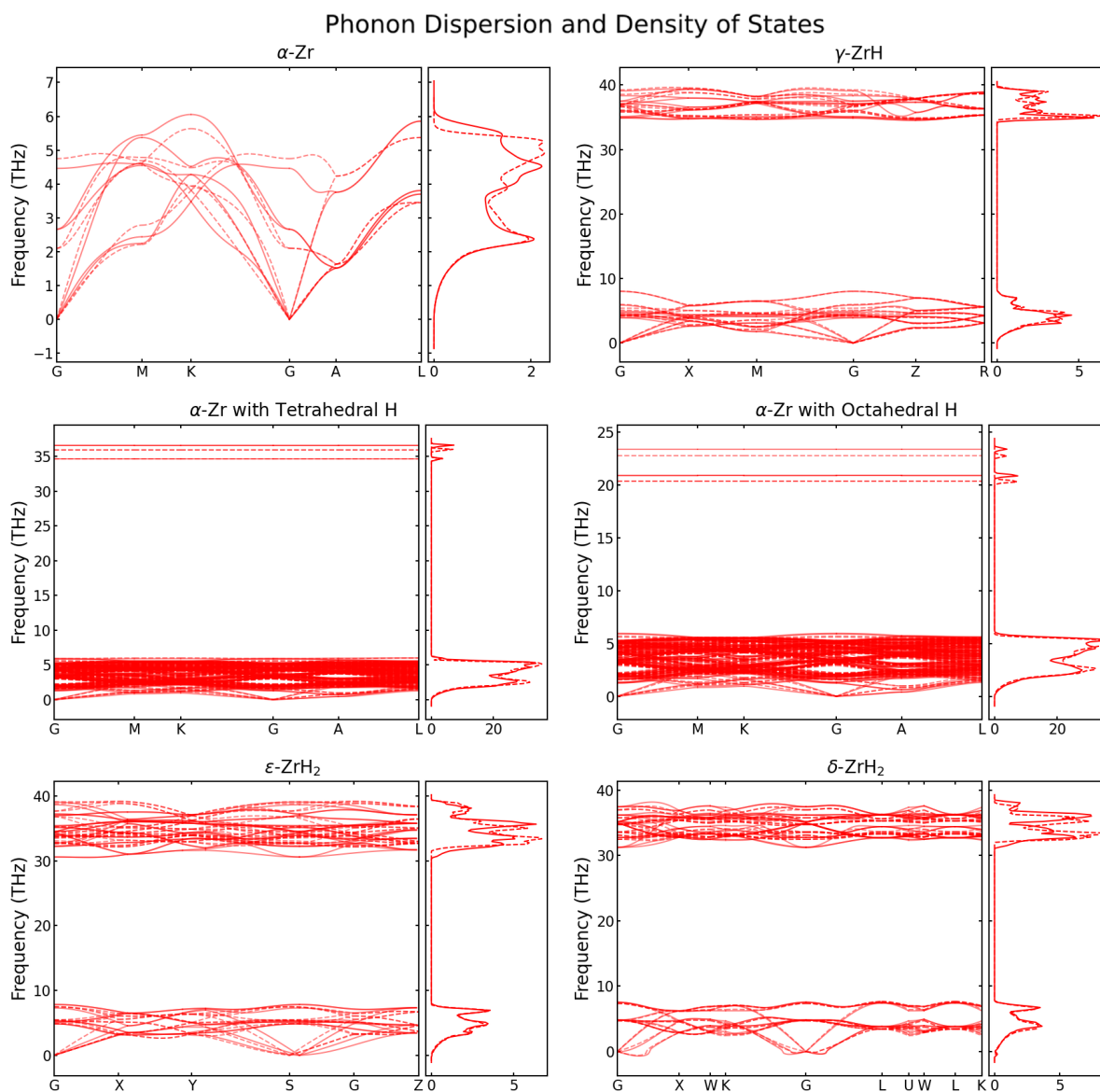


Figure 5.7. Phonon dispersions and Density of States (DoS) of  $\alpha$ -Zr,  $\alpha$ -Zr containing Hydrogen in interstices, and relevant hydride phases, comparing the Zr-ZrH<sub>x</sub> MTP with DFT results. DFT results are shown as a solid line, while predicted behavior calculated under the MTP are shown as the dashed line, and are generally in excellent agreement. The modes below 10 THz are dominated by Zr, while the high frequency modes above 20 THz correspond to H behavior.

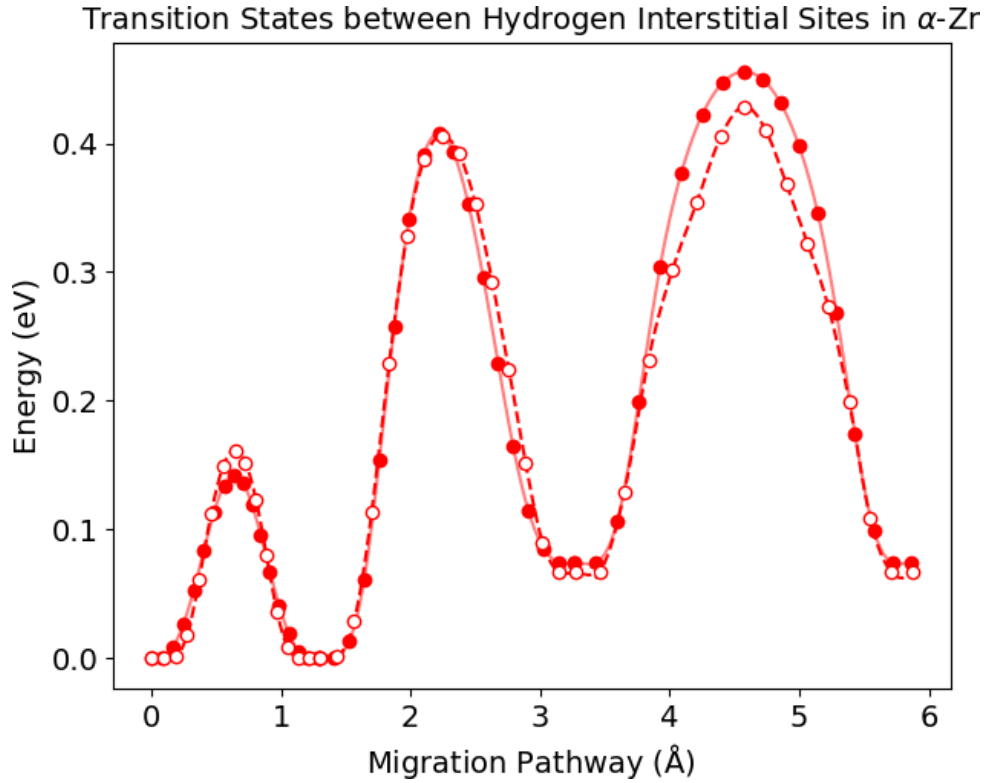


Figure 5.8. Migration pathway of H in  $\alpha$ -Zr, calculated using DFT (solid markers and lines) and MTP (empty circles and dashed lines), first between neighboring tetragonal-tetragonal sites, then tetrahedral to octahedral, and finally octahedral to octahedral. Barrier heights are well reproduced, with errors of 20 meV, 3 meV, and 25 meV for T-T, T-O, and O-O transitions.

thoroughly in section 5.4.2. Wang and colleagues treat anharmonicity in both defect sites [161], following the procedure of Nazarov et. al [109]. This approach displaces the defect H atoms along  $\langle 100 \rangle$ ,  $\langle 110 \rangle$ , and  $\langle 111 \rangle$  directions, applies a quartic fit, and then solves the anharmonic Schrodinger equation. Wang's approach calculates octahedral defects as more stable at 0 K when the vibrational zero point energy (ZPE) is considered, by 10-20 meV across supercell sizes, contradicting Christensen et. al. In the work presented here, we use the results from the fully harmonic treatment, the octahedral site is more stable at 0 K by about 20 meV, when ZPE is considered, as shown in Fig. 5.9.

### 5.3.3. Calculation of Solvus Boundary and Applicability of MTP

We next investigate the effect of temperature on the prediction of the solvus boundary. The experimental phase diagram shows increasing solubility of H into  $\alpha$ , up to about 6 % at 850K. Beyond the solubility limit, the  $\delta$ -ZrH<sub>2-x</sub> phase is found to precipitate in experiment. However the consideration of configurational entropy in the disordered hydrogen-vacancy sublattice of the  $\delta$ -ZrH<sub>2-x</sub> phase adds extra complexity to the question. Thus, similarly to Christensen and colleagues, we substitute the ordered  $\gamma$  phase in our thermodynamic analysis. We follow the ideal solution formulation Ozoliņš and Asta used to study the solubility of Sc in Al to formulate the solubility limit  $c_{s,x}(T)$  of H in a given defect site x in the  $\alpha$ -Zr lattice. [115]. Analogous to their work,  $\Delta G(\text{ZrH})$  is the formation value of the Gibbs free energy per atom of ZrH, while  $\Delta G(\text{H})$  is the solution free energy for a dilute H atom in the host  $\alpha$ -Zr lattice, expressed per H atom.

$$(5.5) \quad c_{s,x}(T) = \exp \left[ \frac{2\Delta G(\text{ZrH}) - \Delta G(\text{H})}{k_B T} \right]$$

In order to account for the two possible defect sites, we simply add the concentrations in both sites, scaled by the number of sites per Zr.

$$(5.6) \quad c_{s,\text{Total}}(T) = c_{s,\text{Octa}}(T) + 2 * c_{s,\text{Tetra}}(T)$$

We note that the only entropy considered is non-configurational:

$$(5.7) \quad \Delta G = \Delta H - T\Delta S_{nc}$$

Vibrational free energy contributions to H defects in  $\alpha$ -Zr and  $\gamma$ -ZrH are shown in Fig. 5.9. Our trained MTP over-stabilizes the interstitial defects when vibrational effects are ignored, however applying the fully harmonic treatment to calculate the vibrational free energy predicts less stable defects under the trained MTP than DFT. These differences are counteracting, such that the deviation in the predicted solvus boundary between DFT and MTP is only 25K at 6% atomic concentration. There is also a difference of about 220K between the solvus boundary predicted by the trained MTP and experiment at 6%. We note that the boundary predicted using the ordered  $\gamma$ -ZrH phase as a reference state should be lower than in experiment at 6%, in which the more stable  $\delta$ -ZrH<sub>2-x</sub> phase forms. If we assume this effect is purely entropic (motivated partially by the disorder of  $\delta$ -ZrH<sub>2-x</sub>, a temperature-independent  $\Delta S_{corr}$  value of 1.4  $k_B$  per hydrogen atom added on to our calculated solvus boundaries would bring them into excellent agreement with experiment. This value is significantly larger than what would be provided by configurational entropy, so it's quite likely either DFT is not fully accurate, or the harmonic approximation introduces significant error.

#### 5.3.4. Phase Transformation of $\epsilon$ -ZrH<sub>2</sub> to $\delta$ -ZrH<sub>2-x</sub>

The cubic  $\delta$ ZrH<sub>2-x</sub> and tetragonal  $\epsilon$ -ZrH<sub>2</sub> phases are closely related and establishing an exact temperature for the phase transformation is challenging due to the presence of oxygen and difficulty in equilibrating samples [184]. The phase diagram of Zr-H usually includes a coexistence region between the two phases [105], and correlation between increasing hydrogen content and transition temperature. Moore et. al measure up to ZrH<sub>1.81</sub>, above which there is significant hydrogen disassociation pressure. At that concentration, they

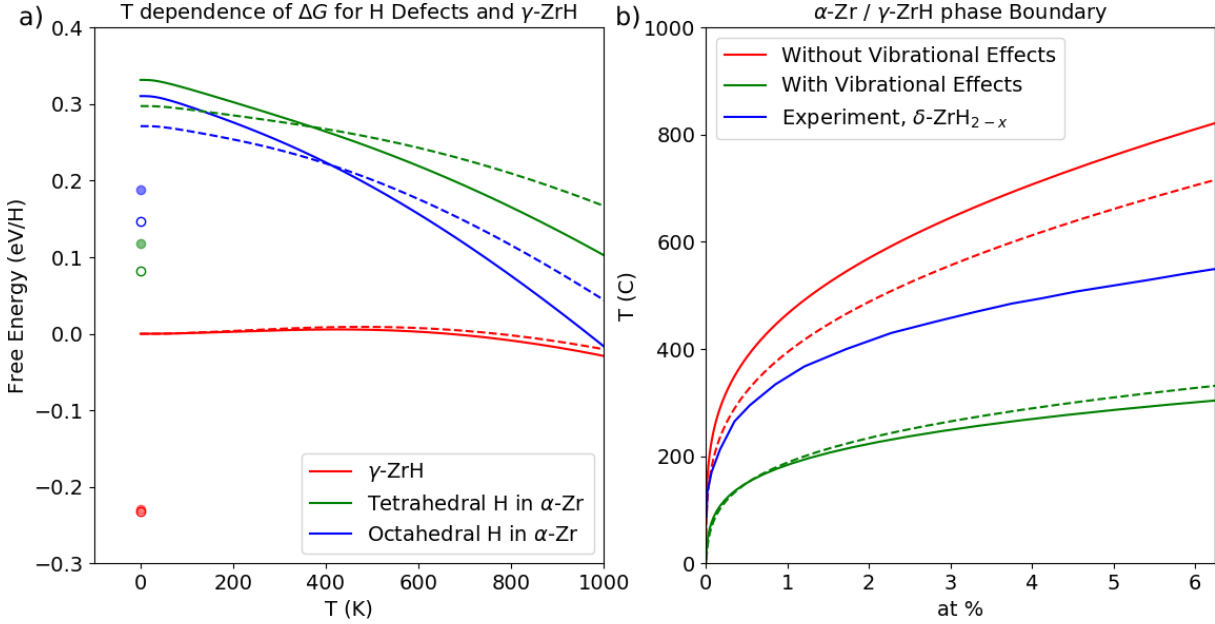


Figure 5.9. a) Free energy per hydrogen atom of dilute hydrogen defect in  $\alpha$ -Zr interstitials and in ordered  $\gamma$ -ZrH, with temperature dependence modeled from the vibrational free energy, calculated under the fully harmonic approximation. Single markers at 0K are purely internal energy values, while lines include vibrational free energy, including Zero Point Energy. Note that the free energy of  $\alpha$ -Zr is subtracted from each, while no reference H state is used, as the MTP is not trained on molecular  $H_2$ . Values are set such that the free energy of  $\gamma$ -ZrH is set to 0 at 0K. Solid lines indicate results from DFT, while dashed lines indicate results predicted by the trained MTP. We find strong agreement for the ordered ZrH phase, while a significant deviation in the defect phases. At 0K, the trained MTP over stabilizes the defects by about 40 meV. However, with increasing temperature, DFT predicts more stable defects within the harmonic approximation. MTP. b) Predicted solvus boundary as calculated from equations 5.5 and 5.6, using DFT (solid lines) and MTP results (dashed lines).

measure a transformation temperature of about 1000K. We further note that their samples contained 4 at % uranium, which may also add some uncertainty. Maimaitiyili et. al. find from their *in-situ* synchrotron x-ray diffraction experiments that no two-phase region exists, and argue that the phase transformation is second-order in nature and does not display any discontinuities.[97]. The coexistence region does not extend for the full extent

of the phase boundary, so it is plausible that the order changes from first to second with increasing temperature.

We next probe phase transformations using NPT molecular dynamics simulations with a Nose-Hoover thermostat, run over our trained MTP. We will carefully track the lattice parameters, searching for a transformation from  $\epsilon$ , in which  $a = b > c$ , to the cubic  $\delta$ -ZrH<sub>2-x</sub> phase, in which all three lattice vectors are equal. The determination of whether the phase transformation is first or second order is beyond the scope of this work, the signals which we carefully monitor during MD could plausibly correspond to either a continuous second order phase transformation, or the coexistence region characteristic of a first order transformation.

Experimentally, at a composition of ZrH<sub>1.83</sub>, the  $c$  lattice vector in  $\epsilon$  increases with rising temperature gradually, starting from about 4.5 Å at room temperature, and rising to about 4.6 Å at 900K, before quickly and continuously rising to 4.8 Å at 1000K. Between room temperature and 900K, the  $a$  and  $b$  lattice parameters only drop by about 0.03 Å. For each simulation, a time step of 0.5 femtosecond was used, with a time damping parameter of 50 femtoseconds and a pressure damping parameter of 500 femtoseconds. We begin with an 8x8x8 supercell of conventional  $\delta$ -ZrH<sub>2</sub>, containing 2048 Zr atoms and 4096 H atoms. We then randomly remove hydrogen to achieve stoichiometries of ZrH<sub>1.6</sub>, ZrH<sub>1.66</sub>, ZrH<sub>1.75</sub>, ZrH<sub>1.83</sub>, and ZrH<sub>1.9</sub>. For each of these stoichiometries and the fully occupied ZrH<sub>2</sub>, we equilibrate at 900K for 50 picoseconds, to minimize the effects of initial hydrogen occupancy on the simulation. We then conduct multiple simulations using these initial structures, each set to constant temperatures across the range of interest, up to 1000K, and equilibrate over 200 picoseconds. We take a time average of the lattice

parameters every 50 femtoseconds, averaging over 4 snapshots spaced by 5 femtoseconds, and then take the running average over the last picosecond. We plot the time average of the last 100 picoseconds for each individual simulation in Fig. 5.10.

The transformation temperature as, measured in experiment is usually taken at a limiting stoichiometry of about  $\text{ZrH}_{1.81}$ , above which significant hydrogen dissociation occurs, with phase diagrams of this region usually drawn off the work of [105]. At this stoichiometry, Moore and colleagues measure a transformation temperature of about 950 K, while for  $\text{ZrH}_{1.83}$ , we simulate a transformation temperature of about 700 K, so we underestimate the transformation temperature by about 250 K. They extrapolate from here, indicating that  $\text{ZrH}_2$  should have a transformation temperature of about 1150 K, a 200 K difference vs the measurement at  $\text{ZrH}_{1.81}$ , while we simulate that the difference is about 100 K under our trained MTP.

The inclusion of the overlaid ZBL was needed to suppress lost atoms during MD equilibration runs for  $\text{ZrH}_{1.83}$ ,  $\text{ZrH}_{1.9}$ ,  $\text{ZrH}_2$  structures at 900K, and for treating  $\text{ZrH}_2$  at 850K. We confirmed that the overlaid ZBL did not meaningfully change the MD trajectories at 800K for these structures.

We have also plotted the Zr-Zr radial distribution function (rdf) captured during these MD simulations in Fig. 5.11, which also confirm the trend of increasing transformation temperature with higher hydrogen content. The rdf is averaged in a similar fashion to the lattice parameter.

We have plotted the phase boundary as determined by the above molecular dynamics simulations, and compared it with experimental measurements from Moore and Young [105], including extrapolated sections, shown in Fig. 5.12. Though the boundary is well

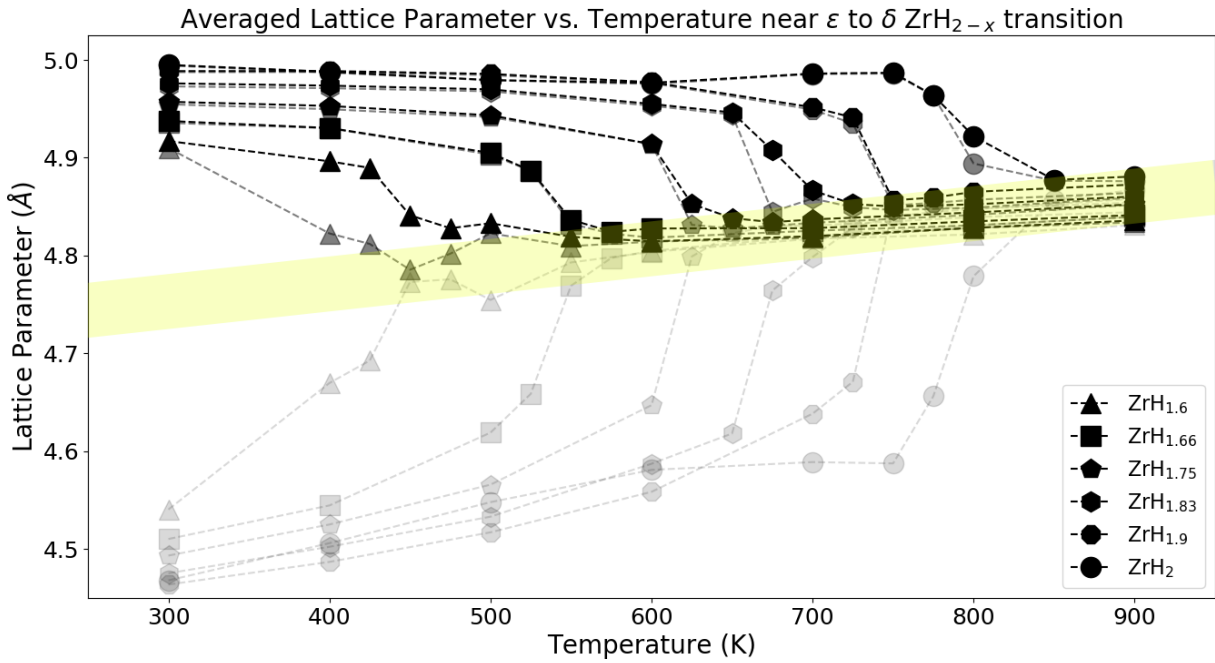


Figure 5.10. Time averaged lattice vectors for hydride stoichiometries ranging from  $\text{ZrH}_{1.6}$  to  $\text{ZrH}_2$  vs. the temperature set by the thermostat during molecular dynamics. Lattice vectors have also been normalized per number of unit cells along each direction. Marker type corresponds to stoichiometry, with more sides indicating higher H content, while darkness corresponds to the order of the lattice parameter, with the lightest marker corresponding to the shortest lattice parameter. We highlight in yellow a rough area corresponding to the cubic lattice parameter range, accounting for thermal expansion. There is a clear trend that the transformation temperature increases as more hydrogen is loaded into the hydride, consistent with experiment, though the trained MTP underestimates the transformation temperature by about 250 K.

estimated for lower hydrogen compositions, we have simulated a less steep temperature dependence with respect to composition. At the limit of experimental measurements, at about  $\text{ZrH}_{1.81}$ , we underestimated the boundary temperature by about 275K. This underestimation is due in some part to the overstabilization of the fully occupied  $\delta$   $\text{ZrH}_2$  phase. Other factors may be inaccuracies in the underlying DFT training set, the lack of

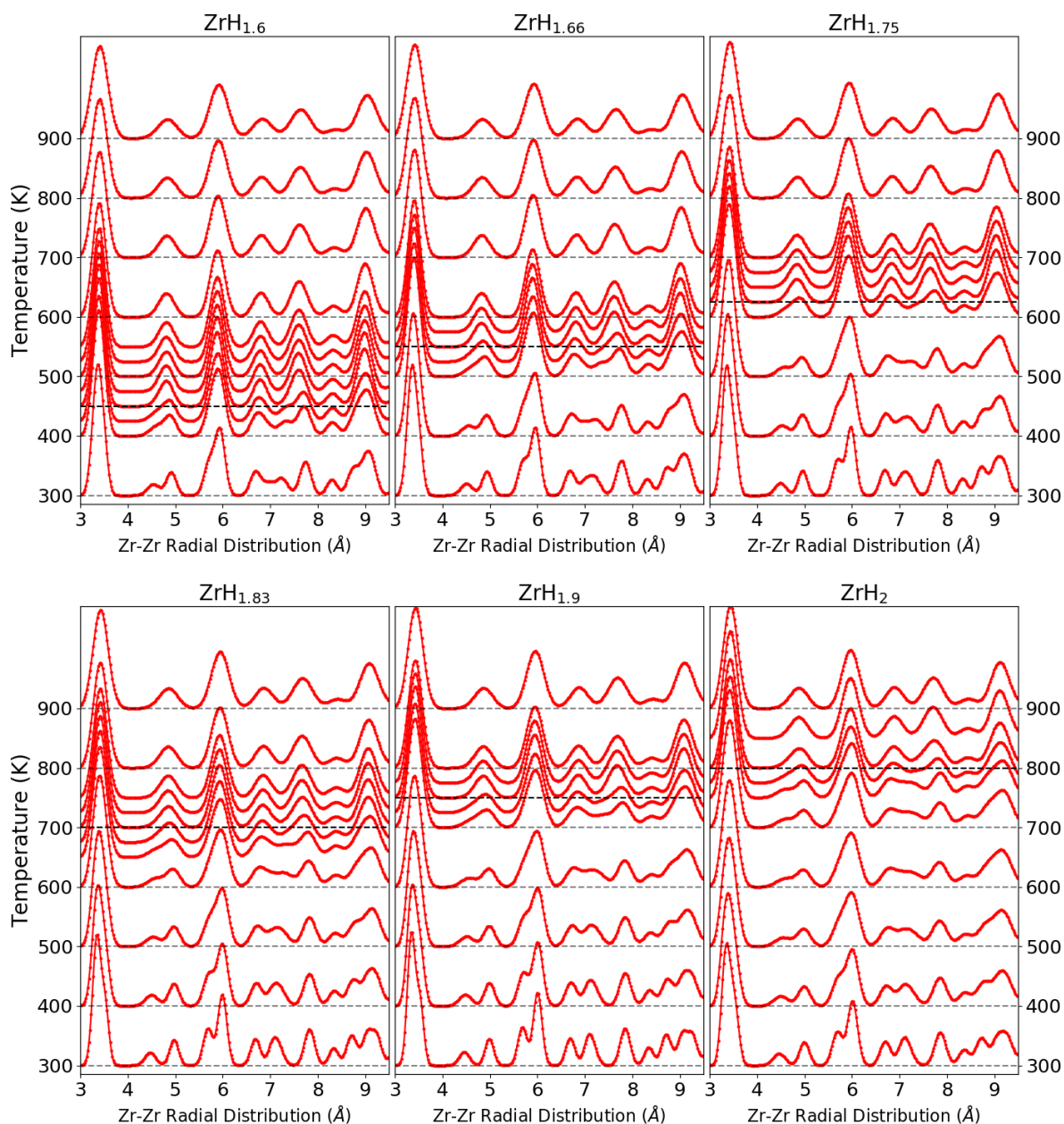


Figure 5.11. Zr-Zr radial distribution function as captured during molecular dynamics, with varying stoichiometry and temperature. The transformation temperature as estimated from 5.10 is marked with a black horizontal line. The trends in the rdf are consistent with the experimental observation that higher hydrogen content corresponds to higher  $\epsilon$  to  $\delta$  transformation temperature.

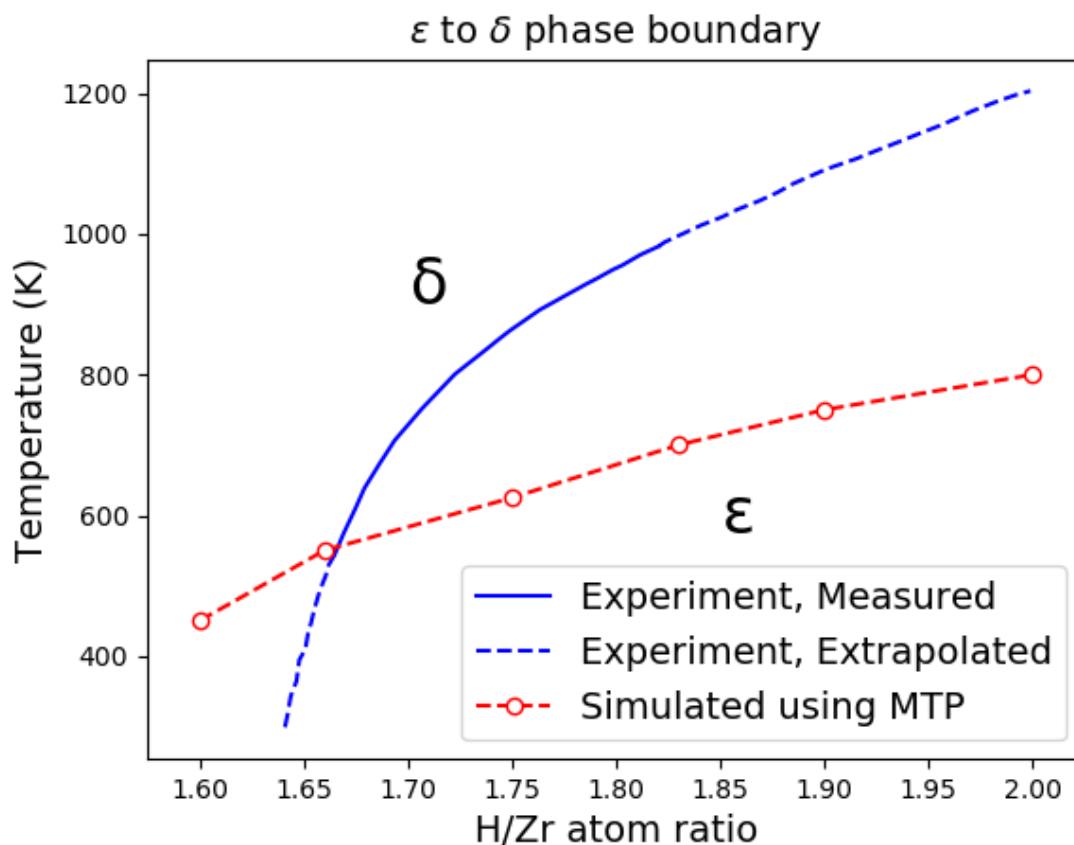


Figure 5.12. Temperature and compositional dependence of the phase boundary between  $\epsilon$  and  $\delta$  phases, calculated using MD simulations using the trained MTP and experiment [105].

quantum effects during simulation, or more information being needed in this portion of the training set.

## 5.4. Results: Validation of Zr-ZrH<sub>x</sub> MTP for Defects Thermodynamics and Migration

We will now validate the trained MTP for defects that are desirable to capture with a Zr-H MLP. These include H-vacancy ordering in the region of the  $\delta$ -ZrH<sub>2-x</sub> phase, H migration in  $\alpha$ -Zr and  $\delta$ -ZrH<sub>2-x</sub>, and various point and planar defects.

### 5.4.1. H-Vacancy ordering on fcc-Zr lattice

In order to more closely evaluate the ability for the trained MTP to accurately capture the dominant  $\delta$ -ZrH<sub>2-x</sub> phase, we have fit a real space cluster expansion using the *maps* program as implemented in ATAT [156], of H distributed on tetrahedral sites in fcc-Zr. Besson and Candela have previously fit cluster expansions of the same system, using short range and long range interactions, and considered the transformation between ordered  $\gamma$ -ZrH and  $\delta$ -ZrH<sub>2-x</sub>, building on previous use of reciprocal-space cluster expansions to model H in the hcp-Zr lattice [57]. In our work, we use 147 total training examples to fit the cluster expansion, as generated automatically using ATAT. We allow these structures to fully relax within DFT before fitting, following modes permitted by their underlying symmetry (ie, a phase that preserves tetragonal symmetry with its H-Vac sublattice will not follow arbitrary triclinic distortions). The results of the cluster expansion fit are shown in Fig. 5.13, with formation energies as calculated in Equation 5.4. A cross-validation score of 3.8 meV/tetrahedral site was found during fitting.

We have primarily fit this cluster expansion for the purpose of generating low energy ordered phases in the composition range corresponding to the  $\delta$ -ZrH<sub>2-x</sub> phase in order to evaluate the trained MTP. A comparison of the convex hulls of the phases used to

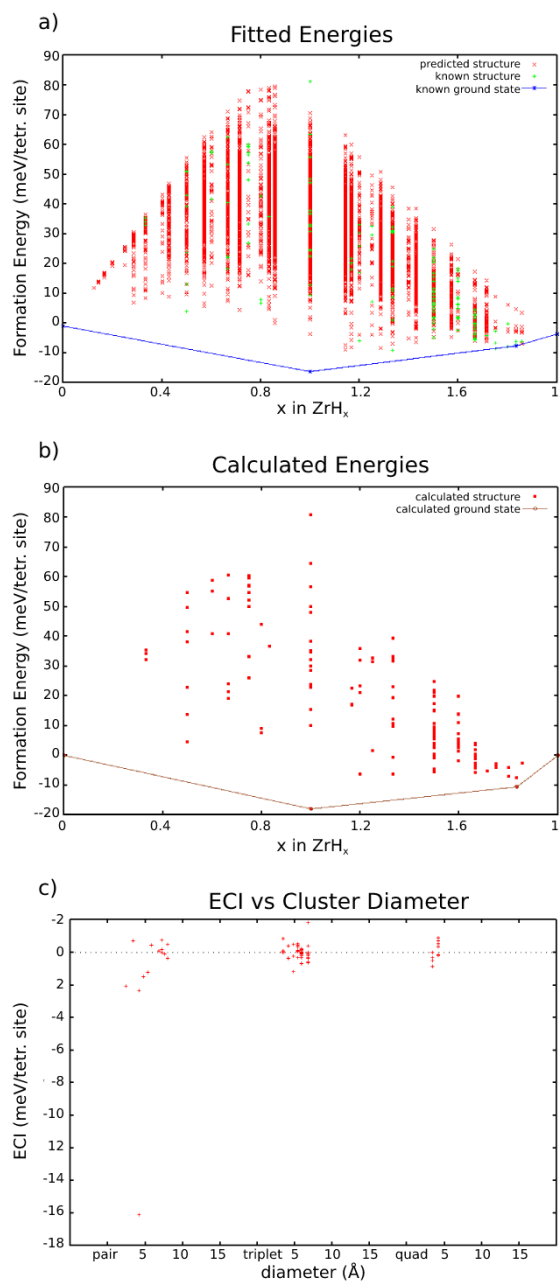


Figure 5.13. a) Cluster expansion fit and b) DFT calculated structures used to fit cluster expansion of tetrahedral H and vacancies decorating fcc Zr lattice. c) shows Effective Cluster Interaction, which is dominated by a short-range pair interaction. End members for the convex hulls are fcc-Zr and fcc-ZrH<sub>2</sub>, which are higher in energy than true ground states.

fit the cluster expansion, as calculated under DFT and the trained MTP, are shown in Fig. 5.14, however in these plots we have computed the convex hull with the known  $\alpha$ -Zr and  $\epsilon$ -Zr-H<sub>2</sub> end members, as well as the  $\gamma$ -ZrH phase, as we are interested in the formation against realistic competing phases. The MTP significantly over-stabilizes the low hydrogen content ZrH<sub>x</sub>,  $x < 1$ , but is able to accurately capture behavior in the low energy region corresponding to the  $\delta$ -ZrH<sub>2-x</sub> phase. Most importantly, the MTP does not erroneously predict any of these phases to be a ground state, though the fcc ZrH<sub>1.5</sub> phase comes close to breaking the convex hull.

Figs. 5.15 and 5.16 compare formation energies for these compounds as calculated by DFT and the trained MTP, with insets showing just the compounds with  $x > 1$  in ZrH<sub>x</sub>. We see that the most significant error is about 20 meV per atom among high hydrogen content structures. The root mean square error for the entire dataset of structures used to calculate the cluster expansion is 11.3 meV, while the rmse for the high hydrogen content subset is 6.3 meV. We note that these structures were not explicitly included in our training set, and the predictions of hydrogen-vacancy interaction is based off information from the MD of the ZrH and ZrH<sub>1.66</sub> phases.

#### 5.4.2. Migration of H in $\alpha$ -Zr and $\delta$ -ZrH<sub>2-x</sub>

It is critical that our trained MTP can accurately capture H diffusion in  $\alpha$ -Zr, as it is a necessary step in the phase transformations and coexistence between  $\alpha$  and hydride phases. We first begin our analysis of H migration in  $\alpha$ -Zr by explicitly computing the three relevant energy barriers: tetrahedral to tetrahedral (T-T), tetrahedral to octahedral (O-T), and octahedral to octahedral (O-O), using the climbing image-Nudged Elastic

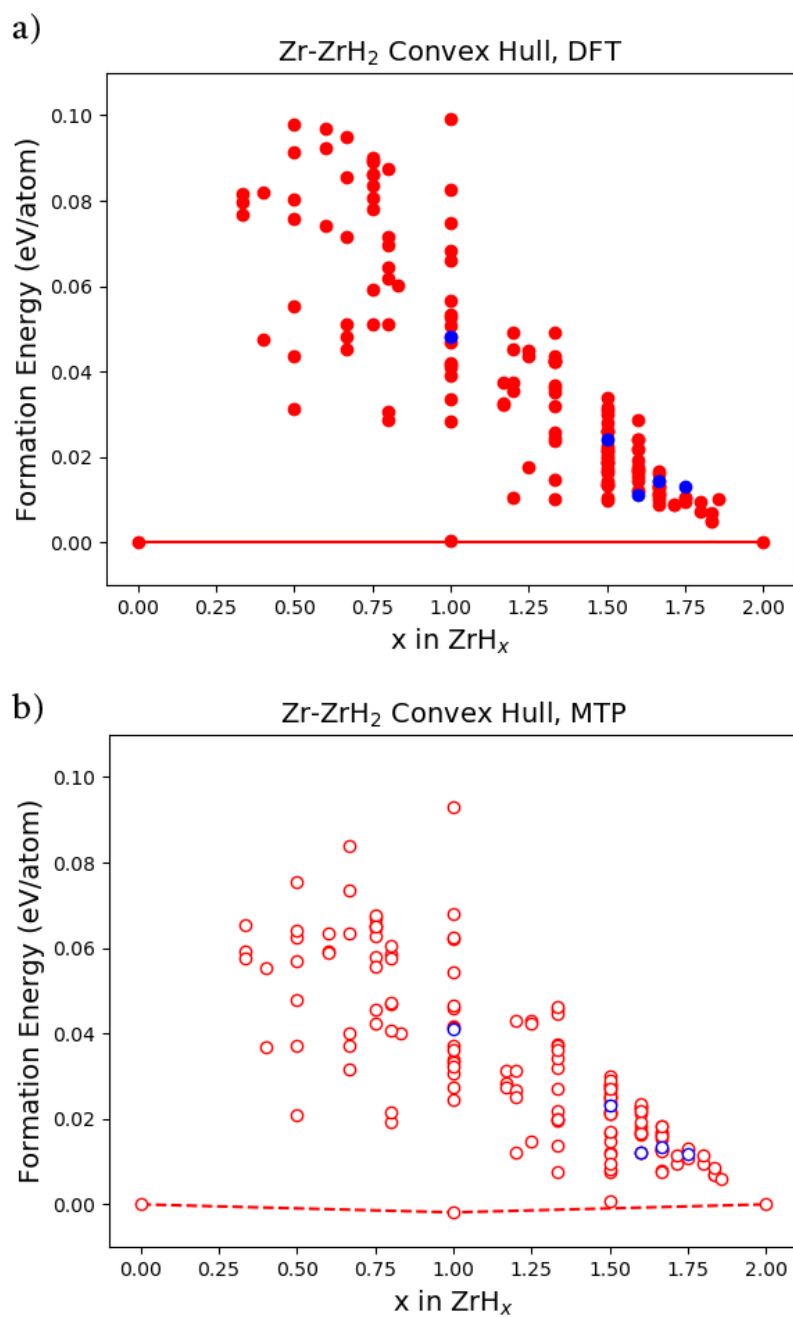


Figure 5.14. Convex Hull of 147 ZrH<sub>x</sub> structures used to fit a cluster expansion (red) and SQS (blue), calculated under DFT and the trained MTP. The low energy phases at  $x = 0, 1, 1.5,$  and  $2$  are hcp  $\alpha$ -Zr,  $\gamma$ -ZrH, the model  $\delta$ -ZrH<sub>1.5</sub>, and  $\epsilon$ -ZrH<sub>2</sub>, as shown in Fig. 5.4.

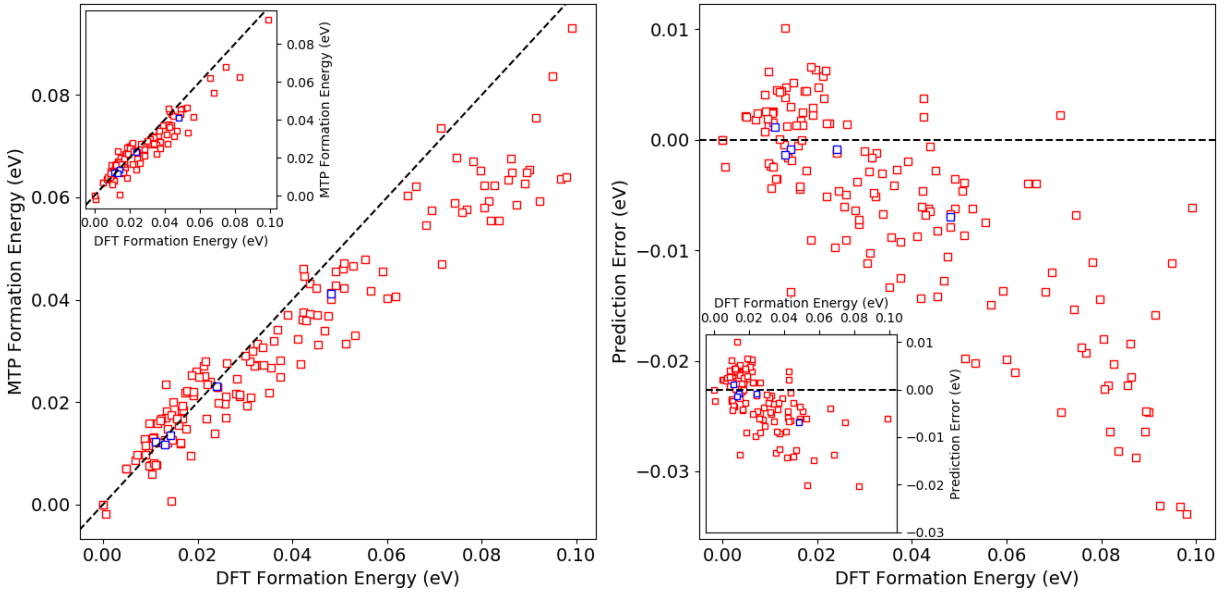


Figure 5.15. Comparison of formation energy of structures used to fit cluster expansion as calculated by DFT and the trained MTP. Insets show just the set of phases where  $x > 1$  in  $\text{ZrH}_x$ , which is better spanned by our training set, and more relevant in simulating bulk hydride behavior.

Band (ci-NEB) method [55] [54], using the Transition States Tools for VASP (VTST) package, and as implemented in LAMMPS. Defect cells were constructed using 36 Zr atoms and a single dilute H atom, and cell sizes were fixed at the equilibrium tetrahedral during ci-NEB. The transition pathways are shown in 5.8. DFT barrier heights are in good agreement with those calculated by Wimmer et al[165].

Tetrahedral interstices have only a single tetrahedral nearest neighbor, and thus the T-T transition presents an energy basin that must be exited in order to achieve net migration. Accelerated Kinetic Monte Carlo calculations carried out by Zhang and colleagues [177], in which this intra-basin step has been sidestepped by an analytical form, have predicted that about 80% of net migration moves are O-T or T-O, and 20% of moves being net T-T steps. These decline as a function of temperature, compensated by increasing O-O

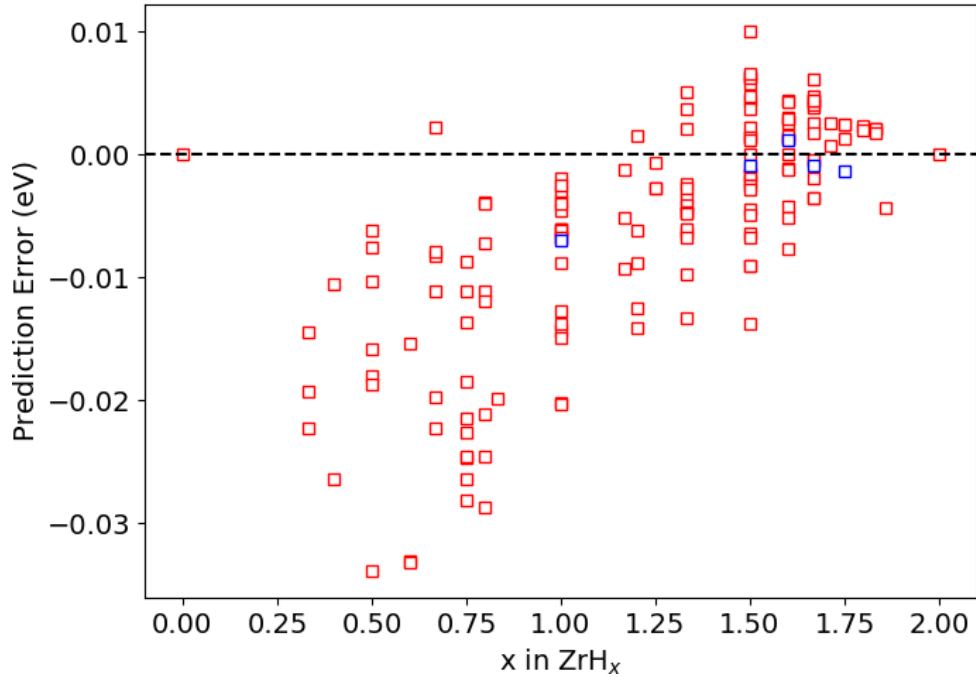


Figure 5.16. Prediction error as a function of hydrogen composition among the cluster expansion training set (red) and SQS structures (blue). We see significantly smaller errors for the hydrogen rich phases above  $x > 1$ , with the highest error of about 20 meV.

steps which read about 5% at 1000 K. Their work also includes an interesting discussion of how diffusion along  $\langle a \rangle$  vs  $\langle c \rangle$  directions are mediated by the different types of jumps, finding that H diffusion along  $\langle a \rangle$  occurs primarily via TO and OT moves, which have opposite  $\langle c \rangle$  components that would cancel out as well. Net diffusion along  $\langle c \rangle$  requires T-T and O-O jumps. Thus all three transition barriers are important in capturing total diffusion in  $\alpha$ -Zr.

We've calculated the diffusion of H in  $\alpha$ -Zr using NVT MD simulations, by tracking the mean-squared-displacement (msd) as a function of time. Cells containing 18 H and 648 Zr atoms were used. Equilibrium volumes were first determined using NPT MD simulations, similar to those carried out in section 5.3.4 concerning  $\epsilon$  and  $\delta$   $\text{ZrH}_{2-x}$ . We

ran the NVT simulations for 3 total nanoseconds, with the first 0.25 ns being treated as equilibration steps. Calculations were carried out at between 700 and 1000 K in intervals of 100 K. We then use linear regression to fit the slope of the final 2.75 ns vs.  $msd$ , to estimate the diffusivity as a function of temperature using the following equation.

$$(5.8) \quad D = \frac{msd}{6t}$$

The factor of 6 coming from the fact that we are treating diffusion in 3 dimensions. Though the presence of multiple relevant barriers means the behavior is not strictly Arrhenius, we can still fit the data to obtain the diffusion coefficient  $D_0$  and energy barrier  $E_a$ , which we estimate to be  $4.45 \times 10^{-7} \text{ m}^2/\text{s}$  and 0.3433 eV.

$$(5.9) \quad D = D_0 \exp \frac{-E_a}{KT}$$

We show our calculated diffusivities in Fig. 5.17, plotted alongside with experimental measurements. We calculate diffusivities that are greater than those in experiment, however the slope compares well, indicating that our activation energy is in good agreement. Zhang and colleagues calculate a  $D_0$  and  $E_a$  of  $5.55 \times 10^{-7} \text{ m}^2/\text{s}$  and 0.41 eV respectively from their KMC simulations, and note that the deviation from experiment is narrowed by the inclusion of impurity defects. The diffusion coefficient predicted by the trained MTP is in good agreement, though the calculated energy barrier is about 60 meV lower than in the KMC simulations. The lower activation barrier as estimated by our calculations maybe due to the lower barrier heights with pathways originating from the octahedral site, or a higher proportion of basin-exiting T-T steps.

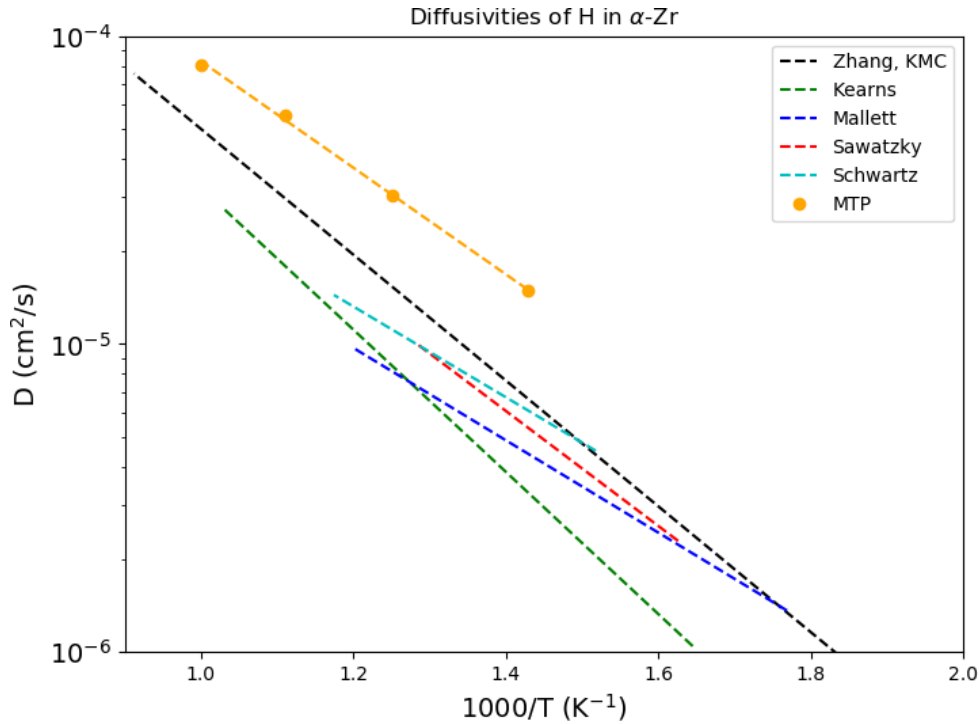


Figure 5.17. Diffusivity of dilute H in  $\alpha$ -Zr as calculated using our trained MTP (yellow) vs a variety of experimental measurements [72, 98, 130, 133], and theoretical KMC calculations [177].

We have also modeled the diffusion behavior of hydrogen in the dominant  $\delta$ -ZrH $_{2-x}$  hydride. The tetrahedral sites in which H sit in the fcc Zr lattice form a simple cubic lattice and permit net diffusion. For these calculations, we use volumes and cells as equilibrated in the previous section on the hydrogen-rich phase transformation, each containing 256 Zr atoms. Due to the larger number of H atoms, and therefore less statistical noise than when treating H defects in  $\alpha$ -Zr, we ran the NVT simulations for a shorter overall time of 0.5 ns, acquiring diffusivities from the final 0.4 ns.

Experimental studies of the diffusivity in the  $\delta$ -ZrH $_{2-x}$  phase are less common in the literature. Korn and Doren conducted an NMR study of diffusivity in both  $\delta$ -ZrH $_{2-x}$  and  $\epsilon$ -ZrH $_{2-x}$  phases, comparing three models of extracting diffusivity  $T_{1d}^{-1}$  from the total

relaxation rate  $\Gamma_1^{-1}$  [79]. We compare with diffusion coefficients and activation energies fit using the theory of Bloembergen, Purcell, and Pound [17]. To convert from their diffusion coefficients  $A$ , reported as a jump rate in Hz, we use the following equation [166].

$$(5.10) \quad D = a^2(1 - c)f(c)A$$

$a$  is the lattice parameter of the hydrogen sublattice, about 2.2 Å in the  $\delta$ -ZrH<sub>2-x</sub> phase,  $c = \frac{2-x}{2}$  is probability of any individual tetrahedral hydrogen site being occupied, and  $f(c)$  is a correlation factor, which is approximated by:

$$(5.11) \quad f(c) = \frac{1 + \langle \cos\theta \rangle}{1 + \langle \cos\theta \rangle * \frac{2-3c}{2-c}}$$

Here,  $\theta$  is the angle between successive diffusive moves in the limit of a fully occupied H sublattice. The expectation value of the cosine is well approximated by -0.2098.

The diffusivities and activation energies are summarized in Table 5.3. As Korn and Doren [79] note, the diffusion coefficient should correlate inversely with H occupation, as there are more vacancies into which diffusion is possible, which our measurements reflect. The modeled activation energies are in excellent agreement with experiment, however calculated diffusion coefficients are an order of magnitude higher than experiment. Some of the inaccuracy in the diffusion coefficient may be similar to the case of  $\alpha$ -Zr, in which sample impurity may suppress diffusion rates. The diffusion coefficient should decrease monotonically with increasing concentration, as is the case in experiment, due to the reduction in neighboring vacancies to jump into. The magnitudes of the diffusivities as

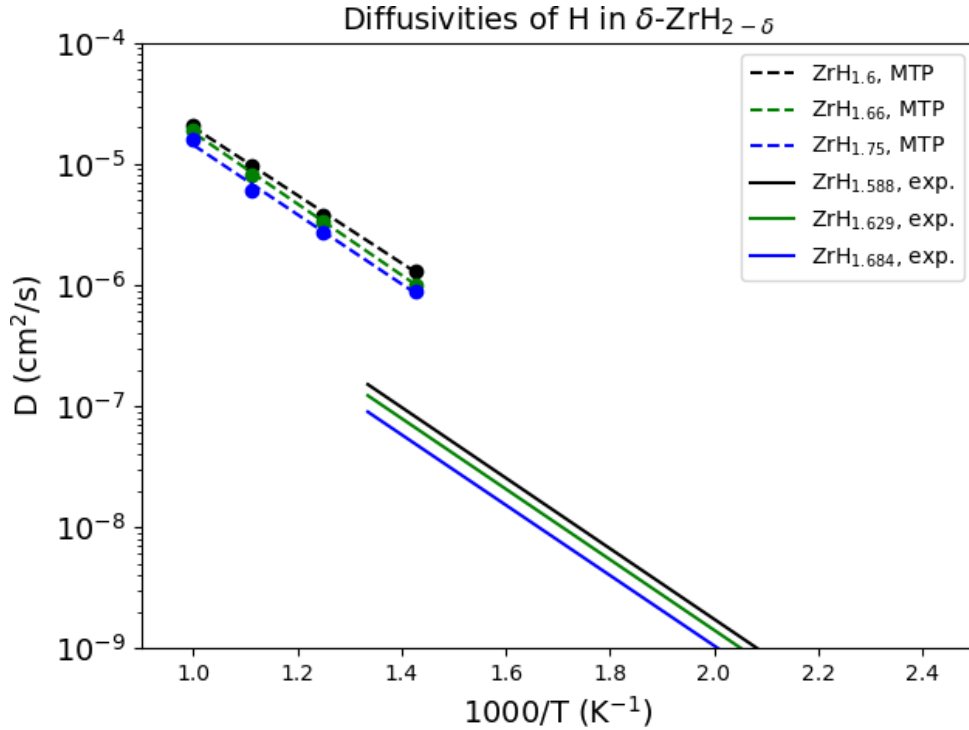


Figure 5.18. Diffusivity of H in  $\delta$ -ZrH<sub>2-x</sub> as calculated using our trained MTP (dashed lines) vs experimental measurements.

a function of temperature follow this trend in our calculations, indicating that this may simply be a numerical issue due to the small temperature range treated, and the relatively small number of H diffusion steps captured, compared to experiment.

The calculation of MSD at 1000K required the inclusion of the overlaid ZBL to suppress lost atoms during MD, as described previously. To test the effect including the ZBL on diffusion, we also overlaid the ZBL on simulations conducted at 900 K. For  $\text{ZrH}_{1.6}$  and  $\text{ZrH}_{1.75}$ , nearly identical trajectories were undergone, with no change in diffusion, indicating the close H-H interactions are very rare at this temperature. A small change of trajectory was seen for  $\text{ZrH}_{1.66}$ , however the difference in diffusivity was just  $4.92 \times 10^{-5} \text{ cm}^2/\text{s}^2$  to  $4.60 \times 10^{-5}$ , a minimal change that would not meaningfully effect

Table 5.3. Fit of H diffusion constant and activation energy in  $\delta$ -ZrH<sub>2-x</sub> phases with varying composition, compared with experimental quantities measured from NMR [79]. The calculated diffusion coefficients are an order of magnitude higher than in experiment, but activation energies are in excellent agreement.

	Comp	D <sub>0</sub> (m <sup>2</sup> /s)	E <sub>a</sub> (eV)
MTP	ZrH <sub>1.6</sub>	1.27 x 10 <sup>-6</sup>	0.556
	ZrH <sub>1.66</sub>	1.60 x 10 <sup>-6</sup>	0.584
	ZrH <sub>1.75</sub>	1.07 x 10 <sup>-6</sup>	0.570
Exp. [79]	ZrH <sub>1.588</sub>	1.18 x 10 <sup>-7</sup>	0.578
	ZrH <sub>1.629</sub>	9.47 x 10 <sup>-8</sup>	0.578
	ZrH <sub>1.684</sub>	6.76 x 10 <sup>-8</sup>	0.576

the calculated diffusion coefficient or activation energy. The presented result is without the overlaid ZBL.

### 5.4.3. Modeling of Defects in Zr

As a matter of practical use of this Zr-H potential, we model its ability to capture a variety of other defects, namely point defects: vacancies and self-interstitials in  $\alpha$ -Zr, and planar defects: surfaces and stacking faults in  $\alpha$ -Zr. These values are summarized in Table 5.4.

For point defects, we used a 3 x 3 x 2 supercell of  $\alpha$ -Zr, with one atom removed for the vacancy and one atom added to an octahedral site for the self interstitial, with calculation accuracy similar to that used to assemble the training set. Though snapshots of MD simulations of the vacancy were included in the training set, the error is quite large at about 0.5 eV higher compared to DFT, which may lead to inaccuracies when using our MTP to study related phenomena, such as H accumulation at vacancy loops. However, the self interstitial defect as calculated by MTP is in excellent agreement with DFT. The basal surface energy was calculated using 6 layers of Zr and about 15 Å of vacuum, and is

also captured well by the trained MTP. The basal stacking fault, however, is overstabilized by our trained MTP, by about  $10 \text{ meV}/\text{\AA}^2$ . This is similar to the error for the stacking fault as calculated under the BMD 19.1 and 19.2 EAM potentials, however in that case, Wimmer and colleagues contextualize this by the overstabilization of the fcc case (only about  $9 \text{ meV}/\text{atom}$  less stable than the groundstate hcp). The trained MTP does not overly stabilize the competing fcc phase, but does overstabilize the stacking fault. The low formation energy may lead to the nucleation of many stacking faults in  $\alpha$ -Zr, especially in the presence of hydride phases.

In order to estimate the interfacial energy of the basal  $\alpha$ -Zr (001) in contact with  $\gamma$ -ZrH (111), we follow a similar approach to Louchez and colleagues [93]. We first construct a series of interfacial multilayers with a 2:3 ratio of formula units of Zr and ZrH. We then calculate the formation energy of each interfacial multilayer cell  $\Delta E_{multi}(f, x)$ :

$$(5.12) \quad \Delta E_{multi}(f, x) = E_{total} - n_{Zr}\mu_{Zr} - n_H\mu_H$$

Here,  $n_i$  and  $\mu_i$  are the number of the each species in a given supercell, and their chemical potential. For this portion of the work, we set chemical potentials such that Zr and ZrH are in equilibrium.  $f$  and  $x$  are respectively the total number of formula units of  $\alpha$ -Zr and  $\gamma$ -ZrH, while  $x$  is the ratio of  $\alpha$  to  $\gamma$ .  $E_{total}$  is the internal energy after full relaxation of the internal coordinates as well as the cell vectors.

We then decompose the energy of each supercell to an interfacial contribution that is proportional to the interfacial area, and an elastic part that is proportional to the total volume of the cell.

Table 5.4. A comparison of point and planar defects in  $\alpha$ -Zr, as calculated by our trained MTP and DFT, as well as a comparison of other possible pure Zr constructs. The point defects are  $E_{vac}$  and  $E_{SIA}$  which are respectively vacancies and self interstitial atoms in Zr. The planar defects  $E_{BSF}$ ,  $E_{BS}$ , and  $E_{BI}$ , which are respectively the energies of basal stacking faults, basal surfaces, and basal interfaces of Zr in contact with ZrH. The majority of DFT reference values are from the work of Wimmer et al. [165], with the exception of  $E_{BS}$ [154] and  $E_{BI}$  [93]. Wimmer et. al show calculated energies of these defects and competing phases using their BMD potentials along with previous potentials from the literature, COMB3 and MA#3, in Table 3.

	$E_{vac}$ (eV)	$E_{SIA}$ (eV)	$E_{BSF}$ (meV/Å <sup>2</sup> )	$E_{BS}$ (meV/Å <sup>2</sup> )	$E_{BI}$ (meV/Å <sup>2</sup> )	$E_{bcc-hcp}$ (meV/atom)	$E_{fcc-hcp}$ (meV/atom)
MTP	2.49	2.91	2.59	95.97	18.49	65.04	29.81
DFT	1.94	3.02	10.77	90.01	20.80	82.62	36.59
DFT (ref)	2.05	2.96	13.80	100.00	12.48	83.00	43.00

$$(5.13) \quad \Delta E_{multi}(f, x) = 2A\sigma + e_{cs}(x)fV_f$$

Here,  $A$  is the area of the interfacial cell, with the factor of two coming from the two interfaces contained in a single cell due to periodic boundary conditions,  $e_{cs}$  is the coherency strain energy, and  $V_f$  is the volume per formula unit. After dividing both sides by  $2A$  and applying a linear fit, we can see that  $\sigma$ , the interfacial energy, can be estimated by the y intercept of the fitted line, while the slope of the fitted line is proportional to  $f$ , while the slope is equal to  $e_{cs}(x)V_f/2A$ . The results are shown in Fig. 5.19. We estimate an interfacial energy and coherency strain of  $\sigma=333.25$  mJ/m<sup>2</sup> and  $e_{cs} = 129.4$  J/cm<sup>3</sup> for DFT, while for MTP we estimate an interfacial energy and coherency strain of  $\sigma=296.28$  mJ/m<sup>2</sup> and  $e_{cs} = 62.6$  J/cm<sup>3</sup>

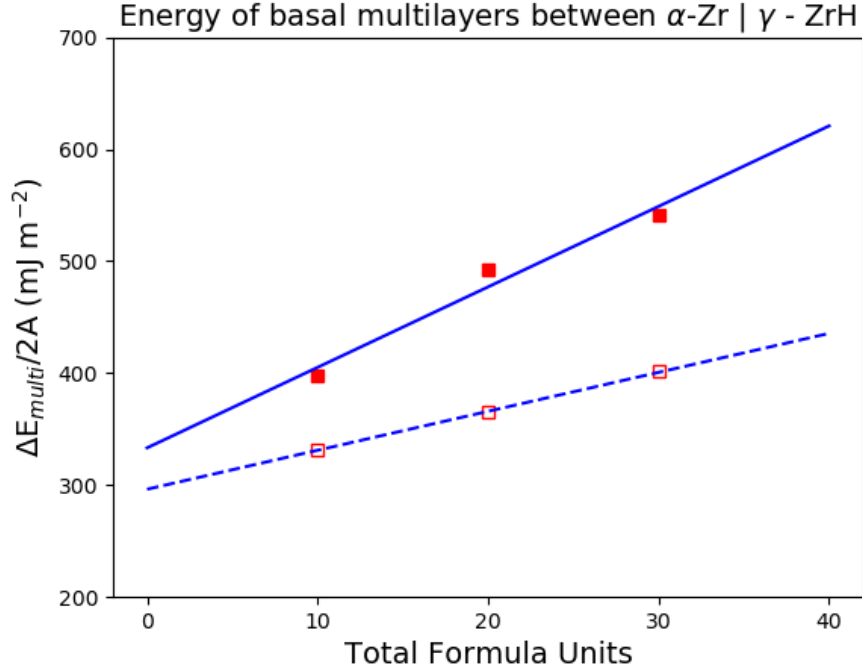


Figure 5.19. Multilayer energies for basal interfaces of  $\alpha$ -Zr and  $\gamma$ -ZrH, at a fixed ratio of  $\alpha$ : $\gamma$  of 2:3 for DFT (solid line and filled markers) and our trained MTP (empty marker and dashed line). By decomposing multilayer energies into interfacial and coherency strain contributions, we can estimate an interfacial energy and coherency strain.

We note Louchez and colleagues calculate a significantly lower interfacial energy than we do for the same cell geometries, at about 200 mJ/m<sup>2</sup>. We suspect that this is primarily due to their use of ultrasoft pseudopotentials. For a cell containing 10 formula units, they calculate a  $E_{multi}/2A$  of about 250 mJ/m<sup>2</sup>, while we calculate about 278 mJ/m<sup>2</sup> by using ultrasoft pseudopotentials, which would explain the bulk of the difference. As they report, we find that the interfacial cell undergoes significant distortion during relaxation. We note that in  $\gamma$ -ZrH in the (111) plane, the Zr-Zr nearest neighbor distances are 3.251 and 3.34 Å, vs in the (001) plane of  $\alpha$ -Zr the nearest neighbor distance is about 3.243. However,

after relaxation, the nearest neighbor distances within the interfacial plane range between 3.16-3.20 Å in the short case, and 3.35-3.38 Å in the long case. The relaxed cells also have a tilt in the  $\beta$  angle of about 85 °, deviating from the constructed 90 °. This distortion of the nearest neighbor distance hints that the ZrH phase is taking a different phase than the tetragonal  $\gamma$  phase, accessible by symmetry due to the presence of the interface.

### 5.5. Discussion

The worked presented here concerning hydrides was conducted using a single MTP, however in the course of investigation we trained many MTP, and noticed that several key properties were quite variable. The properties we have screened for are summarized in Table 5.5. Most notably, the magnitude of the energy of dilute H interstices in  $\alpha$ -Zr showed significant variability, with standard deviations of about 40 meV, enough to change the ordering of octahedral vs tetrahedral defects. Because of our interest in modeling the solvus boundary and subsequent use of the  $\gamma$ -ZrH phase to simplify the picture, we were also wary of a low symmetry orthogonal ZrH phase, which formed during molecular dynamics. This phase is just 0.5 meV/atom less stable than  $\gamma$  in DFT, and the vast majority of the trained MTP overstabilized it, despite it being in the training set. We chose from 5 MTP that correctly stabilized  $\gamma$  at 0K, opting for the potential that best captured the ordering of the formation energy of H in tetrahedral and octahedral sites, as well as  $\gamma$ -ZrH. The potential was also chosen because it compares well with the average behavior predicted by MTP from this ensemble for the formation energies of the  $\delta$ -ZrH<sub>2</sub> and  $\delta$ -ZrH<sub>1.5</sub>, which show a tendency to overstabilize these structures compared to DFT. The variability of certain phases might motivate new approaches when training MLP,

Table 5.5. Summary of outputs considered when screening for candidate MTP during training. Statistical values are all using the same training set and an MTP rank of 22, over a variety of initial weights for energy, force, and stress errors during optimizations. Considered, in order, are the defect formation of octahedral and tetrahedral H interstices in  $\alpha$ -Zr, the formation energy of  $\gamma$ -ZrH and a low energy orthorhombic phase at ZrH, the difference formation energy per H for  $\gamma$ -ZrH and the tetrahedral defect, the difference in formation energy for tetrahedral and octahedral interstitials, the formation energy of the fcc  $\delta$ -ZrH<sub>2</sub> phase, and the formation energy of the fcc  $\delta$ -ZrH<sub>1.5</sub> phase. We show these quantities for DFT, the chosen MTP, and statistics for the 60 trained MTP in this set. All units are meV/atom, except the values involving defect formation energies, which are meV/H

	$F_{H,oct}$ (meV)	$F_{H,tet}$	$F_{ZrH}$	$F_{ZrH,ortho}$	$F_{ZrH,H}-F_{tet,H}$	$F_{tet,H}-F_{oct,H}$	$F_{\delta ZrH_2}$	$F_{\delta ZrH_{1.5}}$
DFT	416.71	346.27	-0.39	0.08	-347.05	-70.44	8.79	12.13
MTP	374.71	309.44	-1.87	-1.87	-313.19	-65.27	3.49	0.70
average	335.19	288.52	-0.57	-3.06	-289.65	-46.68	3.60	0.86
std dev	40.60	43.09	1.01	1.66	42.89	33.06	1.31	3.52
min	230.28	189.25	-2.93	-7.39	-383.46	-116.73	0.88	-9.18
max	430.47	384.12	2.48	-0.43	-189.93	41.55	6.04	9.84

within the MTP framework or otherwise. For instance, it may be advantageous to modify the loss function as to ensure accurate prediction of 0K behavior.

## 5.6. Conclusion

In this work, we have presented a novel Moment Tensor Potential that is applicable to studying multiple phases in the Zr-H system, primarily trained on DFT static calculations selected during active learning during NPT molecular dynamics. The MTP faithfully captures bulk energetics and vibrational properties of both pure  $\alpha$ -Zr and hydride phases of interest, as well as H interstitials in  $\alpha$ -Zr, as calculated with DFT. In addition, the MTP is capable of capturing H-vacancy ordering in  $\delta$ -ZrH<sub>2-x</sub> and  $\epsilon$ -ZrH<sub>2-x</sub> phases. Thus, the MTP estimate of the solvus boundary is in good agreement with DFT, and we are

able to capture the direction of the temperature and composition dependency of the  $\delta$ -ZrH<sub>2-x</sub> to  $\epsilon$ -ZrH<sub>2</sub> phase transformation, albeit under estimating the temperature by about 250K. The MTP also performs well on other point and planar defects, with the notable exceptions of understabilizing Zr vacancies and significantly overstabilizing Zr stacking faults in  $\alpha$ -Zr. We hope this MLP will be used in the future for interesting studies of the Zr-H system or extended upon in the future.

## CHAPTER 6

**Summary and Outlook**

In this dissertation, I have presented three investigations that centered on the study of defects in energy materials. In the first, we adapted the Minima Hopping Method (MHM) to study fine atomic structure at grain boundaries of  $\text{SrTiO}_3$ , uncovering structures that are lower in energy than those previously found in the literature. In the second, we studied the role of cation disorder in  $\text{Li}_3\text{MO}_4$  cathodes in thermodynamic stability and facilitating anionic redox. In the third, we trained a novel Zr-H Moment Tensor Potential that is capable of accurately capturing a suite of defects that are critical in reproducing phase transformations, and is capable of capturing the finite temperature behavior of structures with an impressive level of variation.

There are a few interesting problems that can be addressed using the information and tools developed in this document. In particular, I would like to highlight the possible use of the minima hopping method for studying interfacial structure beyond the benchmarking work presented here. Of course, during my PhD, I spent much effort in doing this myself, in particular attempting to extend its use to the study of batteries. Unfortunately, the potentials available in the literature for Li-ion electrodes and electrolytes did not prove fruitful. Many reproduce grain boundaries that are unphysically found to be unstable against amorphization, at low temperatures of molecular dynamics. Others proved to have very deep energy wells for certain defect structures, likely due to the simple structural form of the interatomic potentials. Of course, an interatomic potential capable of describing

both an electrode and a solid electrolyte phase would be even more difficult to develop than in the case of a single phase. With the availability of computational time always growing, the MHM approach to interfaces might also be useful for generating candidate structures for high-throughput databases of solid-solid interfaces [167] by searching directly using DFT, when attempting to treat non-trivial interfaces which may have reconstructions. I have implemented routines for creating solid interfaces in qmpy, the python back end of OQMD, to help begin the production of our own interface database, and I hope the adapted MHM will be of use there as well.

The recent introduction of magnetic Moment Tensor Potentials (mMTP) [111] may also facilitate the study of complicated battery systems, perhaps even allowing the study of charge transfer. This could allow for more thorough investigations of the relationship between anionic redox and disorder during delithiation.

The inability to find a suitable battery system is what drove my initial interest in working on developing an MTP for Zr-H. The development of the MTP was concurrent with the first attempts in our research group of training MLP, and required that we first develop experience. While we did successfully develop a high-performance MTP for the system, the complications of treating the bulk phases of Zr-H meant I did not have time to treat realistic interfaces of the  $\delta$ -ZrH<sub>2-x</sub> and matrix  $\alpha$ -Zr. I hope a researcher reading this dissertation or the future publication is inspired to use the MTP we've developed to further study fine interactions between  $\delta$ -ZrH<sub>2-x</sub> and matrix  $\alpha$ -Zr, as it may guide the field to better understand the nature of hydride formation, and eventually learn how to suppress its formation.

## References

- [1] AMSLER, M., BOTTI, S., MARQUES, M. A., AND GOEDECKER, S. Conducting boron sheets formed by the reconstruction of the  $\alpha$ -boron (111) surface. *Physical Review Letters* 111, 13 (2013), 1–6.
- [2] AMSLER, M., AND GOEDECKER, S. Crystal structure prediction using the minima hopping method. *Journal of Chemical Physics* 133, 22 (2010).
- [3] AMSLER, M., HEGDE, V. I., JACOBSEN, S. D., AND WOLVERTON, C. Exploring the High-Pressure Materials Genome. *Physical Review X* 8, 4 (nov 2018), 041021.
- [4] AMSLER, M., ROSTAMI, S., TAHMASBI, H., KHAJEHPASHA, E. R., FARAJI, S., RASOULKHANI, R., AND GHASEMI, S. A. FLAME: A library of atomistic modeling environments. *Computer Physics Communications* 256 (2020), 107415.
- [5] AYKOL, M., KIM, S., AND WOLVERTON, C. Van der Waals Interactions in Layered Lithium Cobalt Oxides. *Journal of Physical Chemistry C* 119, 33 (2015), 19053–19058.
- [6] AYKOL, M., KIRKLIN, S., AND WOLVERTON, C. Thermodynamic aspects of cathode coatings for lithium-ion batteries. *Advanced Energy Materials* 4, 17 (2014), 1–11.
- [7] BAK, S.-M., HU, E., ZHOU, Y., YU, X., SENANAYAKE, S. D., CHO, S.-J., KIM, K.-B., CHUNG, K. Y., YANG, X.-Q., AND NAM, K.-W. Structural Changes and Thermal Stability of Charged  $\text{LiNi}_x\text{Mn}_y\text{Co}_z\text{O}_2$  Cathode Materials Studied by Combined In Situ Time-Resolved XRD and Mass Spectroscopy. *ACS Applied Materials and Interfaces* 6, 24 (dec 2014), 22594–22601.
- [8] BALLUFFI, R. W., AND SUTTON, A. P. Why should we be interested in the atomic structure of interfaces? *Materials Science Forum* 207-209, PART 1 (1996), 1–12.
- [9] BAO, K., GOEDECKER, S., KOGA, K., LANÇON, F., AND NEELOV, A. Structure of large gold clusters obtained by global optimization using the minima hopping method. *Physical Review B - Condensed Matter and Materials Physics* 79, 4 (2009), 1–4.

- [10] BARTÓK, A. P., PAYNE, M. C., KONDOR, R., AND CSÁNYI, G. Gaussian approximation potentials: The accuracy of quantum mechanics, without the electrons. *Physical review letters* 104, 13 (2010), 136403.
- [11] BEHLER, J. Perspective: Machine learning potentials for atomistic simulations. *Journal of Chemical Physics* 145, 17 (2016).
- [12] BEHLER, J., AND PARRINELLO, M. Generalized neural-network representation of high-dimensional potential-energy surfaces. *Phys. Rev. Lett.* 98 (Apr 2007), 146401.
- [13] BENEDEK, N. A., CHUA, A. L.-S., ELSÄSSER, C., SUTTON, A. P., AND FINNIS, M. W. Interatomic potentials for strontium titanate: An assessment of their transferability and comparison with density functional theory. *Physical Review B* 78, 6 (2008), 064110.
- [14] BESSON, R., AND CANDELA, R. Ab initio thermodynamics of fcc H-Zr and formation of hydrides. *Computational Materials Science* 114 (2016), 254–263.
- [15] BITZEK, E., KOSKINEN, P., GÄHLER, F., MOSELER, M., AND GUMBSCH, P. Structural relaxation made simple. *Phys. Rev. Lett.* 97 (Oct 2006), 170201.
- [16] BLÖCHL, P. E. Projector augmented-wave method. *Physical Review B* 50, 24 (1994), 17953–17979.
- [17] BLOEMBERGEN, N., PURCELL, E. M., AND POUND, R. V. Relaxation effects in nuclear magnetic resonance absorption. *Physical Review* 73, 7 (1948), 679–712.
- [18] BLOMQVIST, J., OLOFSSON, J., ALVAREZ, A. M., AND BJERKÉN, C. Structure and thermodynamical properties of zirconium hydrides from first-principle. *15th International Conference on Environmental Degradation of Materials in Nuclear Power Systems-Water Reactors 2011 1* (2011), 635–643.
- [19] BROBERG, D., MEDASANI, B., ZIMMERMANN, N. E., YU, G., CANNING, A., HARANCZYK, M., ASTA, M., AND HAUTIER, G. PyCDT: A Python toolkit for modeling point defects in semiconductors and insulators. *Computer Physics Communications* 226 (2018), 165–179.
- [20] CÉSAR, M., GALL, D., AND GUO, H. Reducing Grain-Boundary Resistivity of Copper Nanowires by Doping. *Physical Review Applied* 5, 5 (2016), 1–11.
- [21] CHEN, P. C., LIU, M., DU, J. S., MECKES, B., WANG, S., LIN, H., DRAVID, V. P., WOLVERTON, C., AND MIRKIN, C. A. Interface and heterostructure design in polyelemental nanoparticles. *Science* 363, 6430 (2019), 959–964.

- [22] CHRISTENSEN, M., WOLF, W., FREEMAN, C., WIMMER, E., ADAMSON, R. B., HALLSTADIUS, L., CANTONWINE, P. E., AND MADER, E. V. H in -Zr and in zirconium hydrides: Solubility, effect on dimensional changes, and the role of defects. *Journal of Physics Condensed Matter* 27, 2 (2015), 25402.
- [23] CHRISTENSEN, M., WOLF, W., FREEMAN, C. M., WIMMER, E., ADAMSON, R. B., HALLSTADIUS, L., CANTONWINE, P. E., AND MADER, E. V. Effect of alloying elements on the properties of Zr and the Zr-H system. *Journal of Nuclear Materials* 445, 1-3 (2014), 241–250.
- [24] CHUA, A. L.-S., BENEDEK, N. A., CHEN, L., FINNIS, M. W., AND SUTTON, A. P. A genetic algorithm for predicting the structures of interfaces in multicomponent systems. *Nature materials* 9, 5 (2010), 418–22.
- [25] CURTAROLO, S., SETYAWAN, W., HART, G. L., JAHNATEK, M., CHEPULSKII, R. V., TAYLOR, R. H., WANG, S., XUE, J., YANG, K., LEVY, O., MEHL, M. J., STOKES, H. T., DEMCHENKO, D. O., AND MORGAN, D. AFLOW: An automatic framework for high-throughput materials discovery. *Computational Materials Science* 58 (2012), 218–226.
- [26] CURTAROLO, S., SETYAWAN, W., WANG, S., XUE, J., YANG, K., TAYLOR, R. H., NELSON, L. J., HART, G. L., SANVITO, S., BUONGIORNO-NARDELLI, M., MINGO, N., AND LEVY, O. AFLOWLIB.ORG: A distributed materials properties repository from high-throughput ab initio calculations. *Computational Materials Science* 58 (2012), 227–235.
- [27] DEMKOV, A. A., FONSECA, L. R. C., VERRET, E., TOMFOHR, J., AND SANKEY, O. F. Complex band structure and the band alignment problem at the Si–high- $\kappa$  dielectric interface. *Physical Review B* 71, 19 (may 2005), 195306.
- [28] DERINGER, V. L. Modelling and understanding battery materials with machine-learning-driven atomistic simulations *Journal of Physics : Energy OPEN ACCESS* Modelling and understanding battery materials with machine-learning-driven atomistic simulations. *J. Phys. Energy* 2 (2020), 041003–1–11.
- [29] DERINGER, V. L., TCHOUGRÉEFF, A. L., AND DRONSKOWSKI, R. Crystal Orbital Hamilton Population (COHP) Analysis As Projected from Plane-Wave Basis Sets. *The Journal of Physical Chemistry A* 115, 21 (jun 2011), 5461–5466.
- [30] DOMAIN, C., BESSON, R., AND LEGRIS, A. Atomic-scale Ab-initio study of the Zr-H system: I. Bulk properties. *Acta Materialia* 50, 13 (aug 2002), 3513–3526.

- [31] DOMAIN, C., BESSON, R., AND LEGRIS, A. Atomic-scale ab initio study of the Zr-H system: II. Interaction of H with plane defects and mechanical properties. *Acta Materialia* 52, 6 (2004), 1495–1502.
- [32] DRONSKOWSKI, R., AND BLOECHL, P. E. Crystal orbital Hamilton populations (COHP): energy-resolved visualization of chemical bonding in solids based on density-functional calculations. *The Journal of Physical Chemistry* 97, 33 (aug 1993), 8617–8624.
- [33] DUDAREV, S. L., BOTTON, G. A., SAVRASOV, S. Y., SZOTEK, Z., TEMMERMAN, W. M., AND SUTTON, A. P. Electronic Structure and Elastic Properties of Strongly Correlated Metal Oxides from First Principles: LSDA + U, SIC-LSDA and EELS Study of UO<sub>2</sub> and NiO. *physica status solidi (a)* 166, 1 (mar 1998), 429–443.
- [34] EIVARI, H. A., GHASEMI, S. A., TAHMASBI, H., ROSTAMI, S., FARAJI, S., RASOULKHANI, R., GOEDECKER, S., AND AMSLER, M. Two-Dimensional Hexagonal Sheet of TiO<sub>2</sub>. *Chem. Mater.* 29, 20 (Oct. 2017), 8594–8603.
- [35] EMERY, A. A., SAAL, J. E., KIRKLIN, S., HEGDE, V. I., AND WOLVERTON, C. High-Throughput Computational Screening of Perovskites for Thermochemical Water Splitting Applications. *Chemistry of Materials* 28, 16 (aug 2016), 5621–5634.
- [36] ERNST, F., PIROUZ, P., AND HEUER, A. H. HRTEM study of a Cu/Al<sub>2</sub>O<sub>3</sub> interface. *Philosophical Magazine A* 63, 2 (feb 1991), 259–277.
- [37] FAN, Y., ZHANG, W., ZHAO, Y., GUO, Z., AND CAI, Q. Fundamental understanding and practical challenges of lithium-rich oxide cathode materials: Layered and disordered-rocksalt structure. *Energy Storage Materials* 40, February (2021), 51–71.
- [38] FARAJI, S., GHASEMI, S. A., ROSTAMI, S., RASOULKHANI, R., SCHAEFER, B., GOEDECKER, S., AND AMSLER, M. High accuracy and transferability of a neural network potential through charge equilibration for calcium fluoride. *Phys. Rev. B* 95, 10 (2017), 104105.
- [39] FENG, H. L., REEHUIS, M., HOSER, A., VALLDOR, M., AND JANSEN, M. Crystal structures and magnetic properties of dimorphic Li<sub>3</sub>OsO<sub>4</sub>. *Solid State Sciences* 97, September (2019), 106009.
- [40] FENG, L., HAO, R., LAMBROS, J., AND DILLON, S. J. The influence of dopants and complexion transitions on grain boundary fracture in alumina. *Acta Materialia* 142 (2018), 121–130.

- [41] FISHER, E. S., AND RENKEN, C. J. Single-crystal elastic moduli and the hcp  $\rightarrow$  bcc transformation in Ti, Zr, and Hf. *Physical Review* 135, 2A (1964).
- [42] FISICARO, G., SICHER, M., AMSLER, M., SAHA, S., GENOVESE, L., AND GOEDECKER, S. Surface reconstruction of fluorites in vacuum and aqueous environment. *Physical Review Materials* 1, 3 (aug 2017), 033609.
- [43] FREYSOLDT, C., NEUGEBAUER, J., AND VAN DE WALLE, C. G. Fully Ab Initio Finite-Size Corrections for Charged-Defect Supercell Calculations. *Physical Review Letters* 102, 1 (jan 2009), 016402.
- [44] FRIEDLINGSTEIN, P., JONES, M. W., O’SULLIVAN, M., ANDREW, R. M., BAKKER, D. C. E., HAUCK, J., LE QUÉRÉ, C., PETERS, G. P., PETERS, W., PONGRATZ, J., SITCH, S., CANADELL, J. G., CIAIS, P., JACKSON, R. B., ALIN, S. R., ANTHONI, P., BATES, N. R., BECKER, M., BELLOUIN, N., BOPP, L., CHAU, T. T. T., CHEVALLIER, F., CHINI, L. P., CRONIN, M., CURRIE, K. I., DECHARME, B., DJEUTCHOUANG, L. M., DOU, X., EVANS, W., FEELY, R. A., FENG, L., GASSER, T., GILFILLAN, D., GKRTZALIS, T., GRASSI, G., GREGOR, L., GRUBER, N., GÜRSES, Ö., HARRIS, I., HOUGHTON, R. A., HURTT, G. C., IIDA, Y., ILYINA, T., LUIJKX, I. T., JAIN, A., JONES, S. D., KATO, E., KENNEDY, D., KLEIN GOLDEWIJK, K., KNAUER, J., KORSBAKKEN, J. I., KÖRTZINGER, A., LANDSCHÜTZER, P., LAUVSET, S. K., LEFÈVRE, N., LIENERT, S., LIU, J., MARLAND, G., MCGUIRE, P. C., MELTON, J. R., MUNRO, D. R., NABEL, J. E. M. S., NAKAOKA, S.-I., NIWA, Y., ONO, T., PIERROT, D., POULTER, B., REHDER, G., RESPLANDY, L., ROBERTSON, E., RÖDENBECK, C., ROSAN, T. M., SCHWINGER, J., SCHWINGSHACKL, C., SÉFÉRIAN, R., SUTTON, A. J., SWEENEY, C., TANHUA, T., TANS, P. P., TIAN, H., TILBROOK, B., TUBIELLO, F., VAN DER WERF, G. R., VUICHARD, N., WADA, C., WANNINKHOF, R., WATSON, A. J., WILLIS, D., WILTSHIRE, A. J., YUAN, W., YUE, C., YUE, X., ZAEHLE, S., AND ZENG, J. Global Carbon Budget 2021. *Earth System Science Data* 14, 4 (apr 2022), 1917–2005.
- [45] GALE, J. D. GULP: A computer program for the symmetry-adapted simulation of solids. *Journal of the Chemical Society, Faraday Transactions* 93, 4 (1997), 629–637.
- [46] GALE, J. D., AND ROHL, A. L. The General Utility Lattice Program (GULP). *Molecular Simulation* 29, 5 (2003), 291–341.
- [47] GHASEMI, S. A., AMSLER, M., HENNIG, R. G., ROY, S., GOEDECKER, S., LENOSKY, T. J., UMRIGAR, C. J., GENOVESE, L., MORISHITA, T., AND NISHIO, K. Energy landscape of silicon systems and its description by force fields, tight

- binding schemes, density functional methods, and quantum Monte Carlo methods. *Phys. Rev. B* *81*, 21 (June 2010), 214107.
- [48] GOEDECKER, S. Minima hopping: An efficient search method for the global minimum of the potential energy surface of complex molecular systems. *Journal of Chemical Physics* *120*, 21 (2004), 9911–9917.
- [49] GOEL, N., WEBB, E. B., OZTEKIN, A., RICKMAN, J. M., AND NETI, S. Kapitza resistance at segregated boundaries in  $\beta$ -SiC. *Journal of Applied Physics* *118*, 11 (sep 2015), 115101.
- [50] GUBAEV, K., PODRYABINKIN, E. V., HART, G. L., AND SHAPEEV, A. V. Accelerating high-throughput searches for new alloys with active learning of interatomic potentials. *Computational Materials Science* *156*, June 2018 (2019), 148–156.
- [51] GUBAEV, K., PODRYABINKIN, E. V., HART, G. L., AND SHAPEEV, A. V. Accelerating high-throughput searches for new alloys with active learning of interatomic potentials. *Computational Materials Science* *156* (2019), 148–156.
- [52] GUBAEV, K., PODRYABINKIN, E. V., AND SHAPEEV, A. V. Machine learning of molecular properties: Locality and active learning. *The Journal of chemical physics* *148*, 24 (2018), 241727.
- [53] HE, J., AMSLER, M., XIA, Y., NAGHAVI, S. S., HEGDE, V. I., HAO, S., GOEDECKER, S., OZOLIŅŠ, V., AND WOLVERTON, C. Ultralow Thermal Conductivity in Full Heusler Semiconductors. *Physical Review Letters* *117*, 4 (jul 2016), 046602.
- [54] HENKELMAN, G., AND JÓNSSON, H. Improved tangent estimate in the nudged elastic band method for finding minimum energy paths and saddle points. *Journal of Chemical Physics* *113*, 22 (2000), 9978–9985.
- [55] HENKELMAN, G., UBERUAGA, B. P., AND JÓNSSON, H. Climbing image nudged elastic band method for finding saddle points and minimum energy paths. *Journal of Chemical Physics* *113*, 22 (2000), 9901–9904.
- [56] HOHENBERG, P., AND KOHN, W. Inhomogeneous Electron Gas. *Physical Review* *136*, 3B (nov 1964), B864–B871.
- [57] HOLLIGER, L., AND BESSON, R. Reciprocal-space cluster expansions for complex alloys with long-range interactions. *Physical Review B - Condensed Matter and Materials Physics* *83*, 17 (2011), 1–6.

- [58] HOLLIGER, L., LEGRIS, A., AND BESSON, R. Hexagonal-based ordered phases in H-Zr. *Physical Review B - Condensed Matter and Materials Physics* 80, 9 (2009), 1–9.
- [59] HU, C., HUANG, J., SUMPTER, B. G., MELETIS, E., AND DUMITRICĂ, T. Ab Initio Predictions of Strong Interfaces in Transition-Metal Carbides and Nitrides for Superhard Nanocomposite Coating Applications. *ACS Applied Nano Materials* 1, 5 (may 2018), 2029–2035.
- [60] HU, W., MOLODOV, D. A., SCHÖNFELDER, B., SHVINDLERMAN, L. S., AND GOTTSTEIN, G. HRTEM study on  $\Sigma 7$  grain boundary in aluminium bicrystals with and without Ga doping. *Interface Science* 8, 4 (2000), 335–349.
- [61] HUANG, L., LIU, M., LIN, H., XU, Y., WU, J., DRAVID, V. P., WOLVERTON, C., AND MIRKIN, C. A. Shape regulation of high-index facet nanoparticles by dealloying. *Science* 365, 6458 (2019), 1159–1163.
- [62] HY, S., LIU, H., ZHANG, M., QIAN, D., HWANG, B.-J., AND MENG, Y. S. Performance and design considerations for lithium excess layered oxide positive electrode materials for lithium ion batteries. *Energy & Environmental Science* 9, 6 (2016), 1931–1954.
- [63] IPCC. Summary for Policymakers. In *Climate Change 2022: Impacts, Adaptation and Vulnerability. Working Group II Contribution to the IPCC Sixth Assessment Report.*, vol. 6. Cambridge University Press, may 2022, pp. 3–33.
- [64] ISAACS, E. B., AND MARIANETTI, C. A. Compositional phase stability of correlated electron materials within DFT+DMFT. *Physical Review B* 102, 4 (2020), 1–11.
- [65] ISAACS, E. B., PATEL, S., AND WOLVERTON, C. Prediction of Li intercalation voltages in rechargeable battery cathode materials: Effects of exchange-correlation functional, van der Waals interactions, and Hubbard U. *Physical Review Materials* 4, 6 (2020), 1–11.
- [66] JACQUET, Q., IADECOLA, A., SAUBANÈRE, M., LEMARQUIS, L., BERG, E. J., ALVES DALLA CORTE, D., ROUSSE, G., DOUBLET, M. L., AND TARASCON, J. M. Competition between Metal Dissolution and Gas Release in Li-Rich Li<sub>3</sub>RuyIr<sub>1-y</sub>O<sub>4</sub> Model Compounds Showing Anionic Redox. *Chemistry of Materials* 30, 21 (2018), 7682–7690.

- [67] JAIN, A., HAUTIER, G., MOORE, C. J., PING ONG, S., FISCHER, C. C., MUELLER, T., PERSSON, K. A., AND CEDER, G. A high-throughput infrastructure for density functional theory calculations. *Computational Materials Science* 50, 8 (2011), 2295–2310.
- [68] JAIN, A., HAUTIER, G., ONG, S. P., DACEK, S., AND CEDER, G. Relating voltage and thermal safety in li-ion battery cathodes: A high-throughput computational study. *Physical Chemistry Chemical Physics* 17, 8 (2015), 5942–5953.
- [69] JAIN, A., ONG, S. P., HAUTIER, G., CHEN, W., RICHARDS, W. D., DACEK, S., CHOLIA, S., GUNTER, D., SKINNER, D., CEDER, G., AND PERSSON, K. A. Commentary: The Materials Project: A materials genome approach to accelerating materials innovation. *APL Materials* 1, 1 (jul 2013), 011002.
- [70] JINNOUCHI, R., LAHNSTEINER, J., KARSAI, F., KRESSE, G., AND BOKDAM, M. Phase transitions of hybrid perovskites simulated by machine-learning force fields trained on the fly with bayesian inference. *Physical review letters* 122, 22 (2019), 225701.
- [71] JOHNSTON, K., CASTELL, M. R., PAXTON, A. T., AND FINNIS, M. W. Sr-TiO<sub>3</sub>(001)(2×1) reconstructions: First-principles calculations of surface energy and atomic structure compared with scanning tunneling microscopy images. *Physical Review B - Condensed Matter and Materials Physics* 70, 8 (aug 2004), 085415.
- [72] KEARNS, J. Diffusion coefficient of hydrogen in alpha zirconium, Zircaloy-2 and Zircaloy-4. *Journal of Nuclear Materials* 43, 3 (jun 1972), 330–338.
- [73] KIM, K., ZHOU, B. C., AND WOLVERTON, C. Interfacial stability of  $\theta'$ /Al in Al-Cu alloys. *Scripta Materialia* 159 (2019), 99–103.
- [74] KIM, S., AYKOL, M., HEGDE, V. I., LU, Z., KIRKLIN, S., CROY, J. R., THACKERAY, M. M., AND WOLVERTON, C. Material design of high-capacity Li-rich layered-oxide electrodes: Li<sub>2</sub>MnO<sub>3</sub> and beyond. *Energy and Environmental Science* 10, 10 (2017), 2201–2211.
- [75] KIM, S., AYKOL, M., AND WOLVERTON, C. Surface phase diagram and stability of (001) and (111) LiM<sub>n</sub>O<sub>4</sub> spinel oxides. *Physical Review B - Condensed Matter and Materials Physics* 92, 11 (2015), 7–10.
- [76] KIRKLIN, S., SAAL, J. E., MEREDIG, B., THOMPSON, A., DOAK, J. W., AYKOL, M., RÜHL, S., AND WOLVERTON, C. The Open Quantum Materials Database (OQMD): assessing the accuracy of DFT formation energies. *npj Computational Materials* 1, 1 (dec 2015), 15010.

- [77] KLIME, J., BOWLER, D. R., AND MICHAELIDES, A. Van der Waals density functionals applied to solids. *Physical Review B - Condensed Matter and Materials Physics* 83, 19 (2011), 1–13.
- [78] KLIMEŠ, J., BOWLER, D. R., AND MICHAELIDES, A. Chemical accuracy for the van der Waals density functional. *Journal of Physics Condensed Matter* 22, 2 (2010).
- [79] KORN, C., AND GOREN, S. D. NMR study of hydrogen diffusion in zirconium hydride. *Physical Review B* 33, 1 (1986), 68–78.
- [80] KRAUSE, A. R., CANTWELL, P. R., MARVEL, C. J., COMPSON, C., RICKMAN, J. M., AND HARMER, M. P. Review of grain boundary complexion engineering: Know your boundaries. *Journal of the American Ceramic Society* (sep 2018), jace.16045.
- [81] KRESSE, G., AND FURTHMÜLLER, J. Efficiency of ab-initio total energy calculations for metals and semiconductors using a plane-wave basis set. *Computational Materials Science* 6, 1 (1996), 15–50.
- [82] KRESSE, G., AND FURTHMÜLLER, J. Efficient iterative schemes for ab initio total-energy calculations using a plane-wave basis set. *Physical Review B - Condensed Matter and Materials Physics* 54, 16 (1996), 11169–11186.
- [83] KRESSE, G., AND HAFNER, J. Ab initio molecular dynamics for liquid metals. *Physical Review B* 47, 1 (jan 1993), 558–561.
- [84] KRESSE, G., AND HAFNER, J. Ab initio molecular-dynamics simulation of the liquid-metalamorphous- semiconductor transition in germanium. *Physical Review B* 49, 20 (1994), 14251–14269.
- [85] KRESSE, G., AND JOUBERT, D. From ultrasoft pseudopotentials to the projector augmented-wave method. *Physical Review B* 59, 3 (jan 1999), 1758–1775.
- [86] KUMAGAI, Y., AND OBA, F. Electrostatics-based finite-size corrections for first-principles point defect calculations. *Physical Review B* 89, 19 (may 2014), 195205.
- [87] KVASHNIN, A. G., KVASHNIN, D. G., AND OGANOV, A. R. Novel Unexpected Reconstructions of (100) and (111) Surfaces of NaCl: Theoretical Prediction. *Scientific Reports* 9, 1 (oct 2019), 14267.
- [88] LEE, A., SARKER, S., SAAL, J. E., WARD, L., BORG, C., MEHTA, A., AND WOLVERTON, C. Machine learned synthesizability predictions aided by density functional theory. *Communications Materials* 3, 1 (2022), 1–11.

- [89] LI, L., CASTRO, F. C., PARK, J. S., LI, H., LEE, E., BOYKO, T. D., FREELAND, J. W., YAO, Z., FISTER, T. T., VINSON, J., SHIRLEY, E. L., WOLVERTON, C., CABANA, J., DRAVID, V. P., THACKERAY, M. M., AND CHAN, M. K. Probing Electrochemically Induced Structural Evolution and Oxygen Redox Reactions in Layered Lithium Iridate. *Chemistry of Materials* (2019).
- [90] LI, S., GUNDA, H., RAY, K. G., WONG, C. S., XIAO, P., FRIDDLE, R. W., LIU, Y. S., KANG, S. Y., DUN, C., SUGAR, J. D., KOLASINSKI, R. D., WAN, L. F., BAKER, A. A., LEE, J. R., URBAN, J. J., JASUJA, K., ALLENDORF, M. D., STAVILA, V., AND WOOD, B. C. Spontaneous dynamical disordering of borophenes in MgB<sub>2</sub> and related metal borides. *Nature Communications* 12, 1 (2021), 1–12.
- [91] LIU, P., VERDI, C., KARSAI, F., AND KRESSE, G.  $\alpha$ - $\beta$  Phase Transition of Zirconium Predicted By on-the-Fly Machine-Learned Force Field. *Physical Review Materials* 5, 5 (2021), 1–11.
- [92] LIYANAGE, M., REITH, D., EYERT, V., AND CURTIN, W. A. Machine learning for metallurgy V: A neural-network potential for zirconium. *Physical Review Materials* 6, 6 (2022), 63804.
- [93] LOUCHEZ, M. A., BESSON, R., THUINET, L., AND LEGRIS, A. Interfacial properties of hydrides in  $\mu$ -Zr: A theoretical study. *Journal of Physics Condensed Matter* 29, 41 (2017).
- [94] LUN, Z., OUYANG, B., CAI, Z., CLÉMENT, R. J., KWON, D. H., HUANG, J., PAPP, J. K., BALASUBRAMANIAN, M., TIAN, Y., MCCLOSKEY, B. D., JI, H., KIM, H., KITCHAEV, D. A., AND CEDER, G. Design Principles for High-Capacity Mn-Based Cation-Disordered Rocksalt Cathodes. *Chem* 6, 1 (2020), 153–168.
- [95] LUO, J. Interfacial engineering of solid electrolytes. *Journal of Materiomics* 1, 1 (2015), 22–32.
- [96] M GANOSE, A., J JACKSON, A., AND O SCANLON, D. sumo: Command-line tools for plotting and analysis of periodic ab initio calculations. *Journal of Open Source Software* 3, 28 (2018), 717.
- [97] MAIMAITIYILI, T., STEUWER, A., BLOMQUIST, J., BJERKÉN, C., BLACKMUR, M. S., ZANELATO, O., ANDRIEUX, J., AND RIBEIRO, F. Observation of the  $\delta$  to  $\epsilon$  Zr-hydride transition by in-situ synchrotron X-ray diffraction. *Crystal Research and Technology* 51, 11 (2016), 663–670.

- [98] MALLET, M. W., AND ALBRECHT, W. M. Low-Pressure Solubility and Diffusion of Hydrogen in Zirconium. *Journal of The Electrochemical Society* 104, 3 (1957), 142.
- [99] MARZARI, N., FERRETTI, A., AND WOLVERTON, C. Electronic-structure methods for materials design. *Nature Materials* 20, 6 (2021), 736–749.
- [100] MAXWELL, C. I., TORRES, E., AND PENCER, J. Molecular dynamics study of hydrogen-vacancy interactions in  $\alpha$ -zirconium. *Journal of Nuclear Materials* 511 (2018), 341–352.
- [101] MENDELEV, M. I., AND ACKLAND, G. J. Development of an interatomic potential for the simulation of phase transformations in zirconium. *Philosophical Magazine Letters* 87, 5 (2007), 349–359.
- [102] MIZUSHIMA, K., JONES, P., WISEMAN, P., AND GOODENOUGH, J.  $\text{Li}_x\text{CoO}_2$  ( $0 < x < 1$ ): A new cathode material for batteries of high energy density. *Materials Research Bulletin* 15, 6 (jun 1980), 783–789.
- [103] MOGCK, S., KOOL, B. J., DE HOSSON, J. T. M., AND FINNIS, M. W. Ab initio transmission electron microscopy image simulations of coherent Ag - Mg O interfaces. *Physical Review B* 70, 24 (dec 2004), 245427.
- [104] MOMMA, K., AND IZUMI, F. VESTA 3 for three-dimensional visualization of crystal, volumetric and morphology data. *Journal of Applied Crystallography* 44, 6 (2011), 1272–1276.
- [105] MOORE, K., AND YOUNG, W. Phase studies of the Zr-H system at high hydrogen concentrations. *Journal of Nuclear Materials* 27, 3 (sep 1968), 316–324.
- [106] MOTTA, A. T., CAPOLUNGO, L., CHEN, L. Q., CINBIZ, M. N., DAYMOND, M. R., KOSS, D. A., LACROIX, E., PASTORE, G., SIMON, P. C. A., TONKS, M. R., WIRTH, B. D., AND ZIKRY, M. A. Hydrogen in zirconium alloys: A review. *Journal of Nuclear Materials* 518 (2019), 440–460.
- [107] MUELLER, T., HAUTIER, G., JAIN, A., AND CEDER, G. Evaluation of Tavorite-Structured Cathode Materials for Lithium-Ion Batteries Using High-Throughput Computing. *Chemistry of Materials* 23, 17 (2011), 3854–3862.
- [108] MUELLER, T., KUSNE, A. G., AND RAMPRASAD, R. Machine Learning in Materials Science : Recent Progress and Emerging Applications.

- [109] NAZAROV, R., HICKEL, T., AND NEUGEBAUER, J. Ab initio study of H-vacancy interactions in fcc metals: Implications for the formation of superabundant vacancies. *Physical Review B* 89, 14 (apr 2014), 144108.
- [110] NOORDHOEK, M. J., LIANG, T., CHIANG, T. W., SINNOTT, S. B., AND PHILLPOT, S. R. Mechanisms of Zr surface corrosion determined via molecular dynamics simulations with charge-optimized many-body (COMB) potentials. *Journal of Nuclear Materials* 452, 1-3 (2014), 285–295.
- [111] NOVIKOV, I., GRABOWSKI, B., KÖRMANN, F., AND SHAPEEV, A. Magnetic Moment Tensor Potentials for collinear spin-polarized materials reproduce different magnetic states of bcc Fe. *npj Computational Materials* 8, 1 (2022), 1–6.
- [112] NOVIKOV, I. S., GUBAEV, K., PODRYABINKIN, E. V., AND SHAPEEV, A. V. The MLIP package: moment tensor potentials with MPI and active learning. *Machine Learning: Science and Technology* 2, 2 (jan 2021), 025002.
- [113] NOVOSELOV, I., YANILKIN, A., SHAPEEV, A., AND PODRYABINKIN, E. Moment tensor potentials as a promising tool to study diffusion processes. *Computational Materials Science* 164 (jun 2019), 46–56.
- [114] OLSSON, P. A., KESE, K., AND ALVAREZ HOLSTON, A. M. On the role of hydrogen filled vacancies on the embrittlement of zirconium: An ab initio investigation. *Journal of Nuclear Materials* 467 (2015), 311–319.
- [115] OZOLIŅŠ, V., AND ASTA, M. Large vibrational effects upon calculated phase boundaries in Al-Sc. *Physical Review Letters* 86, 3 (2001), 448–451.
- [116] PADHI, A. K., NANJUNDASWAMY, K. S., MASQUELIER, C., OKADA, S., AND GOODENOUGH, J. B. Effect of Structure on the Fe<sup>3+</sup> / Fe<sup>2+</sup> + Redox Couple in Iron Phosphates. *Journal of The Electrochemical Society* 144, 5 (may 1997), 1609–1613.
- [117] PARK, J. S., KIM, S., XIE, Z., AND WALSH, A. Point defect engineering in thin-film solar cells. *Nature Reviews Materials* 3, 7 (2018), 194–210.
- [118] PARLINSKI, K., LI, Z. Q., AND KAWAZOE, Y. First-Principles Determination of the Soft Mode in Cubic ZrO<sub>2</sub>. *Physical Review Letters* 78, 21 (may 1997), 4063–4066.
- [119] PERDEW, J. P., BURKE, K., AND ERNZERHOF, M. Generalized gradient approximation made simple. *Physical Review Letters* 77, 18 (1996), 3865–3868.

- [120] PEREZ, A. J., JACQUET, Q., BATUK, D., IADECOLA, A., SAUBANÈRE, M., ROUSSE, G., LARCHER, D., VEZIN, H., DOUBLET, M. L., AND TARASCON, J. M. Approaching the limits of cationic and anionic electrochemical activity with the Li-rich layered rocksalt  $\text{Li}_3\text{IrO}_4$ . *Nature Energy* 2, 12 (2017), 954–962.
- [121] PODRYABINKIN, E. V., AND SHAPEEV, A. V. Active learning of linearly parametrized interatomic potentials. *Computational Materials Science* 140 (dec 2017), 171–180.
- [122] PODRYABINKIN, E. V., AND SHAPEEV, A. V. Active learning of linearly parametrized interatomic potentials. *Computational Materials Science* 140 (2017), 171–180.
- [123] QIAN, D., XU, B., CHI, M., AND MENG, Y. S. Uncovering the roles of oxygen vacancies in cation migration in lithium excess layered oxides. *Phys. Chem. Chem. Phys.* 16, 28 (jun 2014), 14665–14668.
- [124] ROSENBROCK, C. W., GUBAEV, K., SHAPEEV, A. V., PÁRTAY, L. B., BERNSTEIN, N., CSÁNYI, G., AND HART, G. L. Machine-learned interatomic potentials for alloys and alloy phase diagrams. *npj Computational Materials* 7, 1 (2021), 1–9.
- [125] ROY, S., GOEDECKER, S., FIELD, M. J., AND PENEV, E. A Minima Hopping Study of All-Atom Protein Folding and Structure Prediction. *The Journal of Physical Chemistry B* 113, 20 (may 2009), 7315–7321.
- [126] ROY, S., GOEDECKER, S., AND HELLMANN, V. Bell-evans-polanyi principle for molecular dynamics trajectories and its implications for global optimization. *Phys. Rev. E* 77 (May 2008), 056707.
- [127] SAAL, J. E., KIRKLIN, S., AYKOL, M., MEREDIG, B., AND WOLVERTON, C. Materials design and discovery with high-throughput density functional theory: The open quantum materials database (OQMD). *Jom* 65, 11 (2013), 1501–1509.
- [128] SAKAGUCHI, N., ICHINOSE, H., AND WATANABE, S. Atomic Structure of Faceted  $\Sigma 3$  CSL Grain Boundary in Silicon: HRTEM and Ab-initio Calculation. *MATERIALS TRANSACTIONS* 48, 10 (2007), 2585–2589.
- [129] SANCHEZ-LOPEZ, D. Sustainable Governance of Strategic Minerals: Post-Neoliberalism and Lithium in Bolivia. *Environment: Science and Policy for Sustainable Development* 61, 6 (nov 2019), 18–30.
- [130] SAWATZKY, A. The diffusion and solubility of hydrogen in the alpha phase of zircaloy-2. *Journal of Nuclear Materials* 2, 1 (mar 1960), 62–68.

- [131] SCHAEFER, B., MOHR, S., AMSLER, M., AND GOEDECKER, S. Minima hopping guided path search: An efficient method for finding complex chemical reaction pathways. *Journal of Chemical Physics* 140, 21 (2014).
- [132] SCHUSTERITSCH, G., AND PICKARD, C. J. Predicting interface structures: From SrTiO<sub>3</sub> to graphene. *Physical Review B - Condensed Matter and Materials Physics* 90, 3 (2014), 1–7.
- [133] SCHWARTZ, C. M., AND MALLET, M. W. Observations on the Behavior of Hydrogen in Zirconium. undefined.
- [134] SCHWENKER, E., KOLLURU, V. S. C., GUO, J., ZHANG, R., HU, X., LI, Q., PAUL, J. T., HERSAM, M. C., DRAVID, V. P., KLIE, R., GUEST, J. R., AND CHAN, M. K. Ingrained: An Automated Framework for Fusing Atomic-Scale Image Simulations into Experiments. *Small* 18, 19 (2022), 1–10.
- [135] SEO, D. H., LEE, J., URBAN, A., MALIK, R., KANG, S., AND CEDER, G. The structural and chemical origin of the oxygen redox activity in layered and cation-disordered Li-excess cathode materials. *Nature Chemistry* 8, 7 (2016), 692–697.
- [136] SHAPEEV, A. V. Moment Tensor Potentials: A Class of Systematically Improvable Interatomic Potentials. *Multiscale Modeling & Simulation* 14, 3 (jan 2016), 1153–1173.
- [137] SHAPEEV, A. V., PODRYABINKIN, E. V., GUBAEV, K., TASNÁDI, F., AND ABRIKOSOV, I. A. Elinvar effect in  $\beta$ -Ti simulated by on-the-fly trained moment tensor potential. *New Journal of Physics* 22, 11 (2020).
- [138] SHENGO, M. L., KIME, M. B., MAMBWE, M. P., AND NYEMBO, T. K. A review of the beneficiation of copper-cobalt-bearing minerals in the Democratic Republic of Congo. *Journal of Sustainable Mining* 18, 4 (2019), 226–246.
- [139] SKINNER, G. B., AND JOHNSTON, H. L. Thermal expansion of zirconium between 298°K and 1600°K. *The Journal of Chemical Physics* 21, 8 (1953), 1383–1384.
- [140] SLADE, T. J., BAILEY, T. P., GROVOGUI, J. A., HUA, X., ZHANG, X., KUO, J. J., HADAR, I., SNYDER, G. J., WOLVERTON, C., DRAVID, V. P., UHER, C., AND KANATZIDIS, M. G. High Thermoelectric Performance in PbSe–NaSbSe<sub>2</sub> Alloys from Valence Band Convergence and Low Thermal Conductivity. *Advanced Energy Materials* 9, 30 (2019), 1–12.
- [141] SNYDACKER, D. H., AND WOLVERTON, C. Transition-Metal Mixing and Redox Potentials in Li<sub>x</sub>(M<sub>1–y</sub>M'<sub>y</sub>)PO<sub>4</sub> (M, M' = Mn, Fe, Ni) Olivine Materials from

- First-Principles Calculations. *The Journal of Physical Chemistry C* 120, 11 (mar 2016), 5932–5939.
- [142] STEINHARDT, P. J., NELSON, D. R., AND RONCHETTI, M. Bond-orientational order in liquids and glasses. *Physical Review B* 28, 2 (jul 1983), 784–805.
- [143] SWIFT, M. W., JAGAD, H., PARK, J., QIE, Y., WU, Y., AND QI, Y. Predicting low-impedance interfaces for solid-state batteries. *Current Opinion in Solid State and Materials Science* 26, 3 (2022), 100990.
- [144] SWIFT, M. W., AND QI, Y. First-principles prediction of potentials and space-charge layers in all-solid-state batteries. *Physical Review Letters* 122, 16 (2019), 167701.
- [145] TAYLOR, N. T., DAVIES, F. H., RUDKIN, I. E. M., PRICE, C. J., CHAN, T. H., AND HEPPLESTONE, S. P. ARTEMIS: Ab initio restructuring tool enabling the modelling of interface structures. *Computer Physics Communications* 257 (2020), 107515.
- [146] THACKERAY, M., JOHNSON, P., DE PICCIOTTO, L., BRUCE, P., AND GOODE-NOUGH, J. Electrochemical extraction of lithium from  $\text{LiMn}_2\text{O}_4$ . *Materials Research Bulletin* 19, 2 (feb 1984), 179–187.
- [147] THACKERAY, M. M., WOLVERTON, C., AND ISAACS, E. D. Electrical energy storage for transportation - Approaching the limits of, and going beyond, lithium-ion batteries. *Energy and Environmental Science* 5, 7 (2012), 7854–7863.
- [148] THOMAS, B. S., MARKS, N. A., AND BEGG, B. D. Defects and threshold displacement energies in  $\text{SrTiO}_3$  perovskite using atomistic computer simulations. *Nuclear Instruments and Methods in Physics Research, Section B: Beam Interactions with Materials and Atoms* 254, 2 (2007), 211–218.
- [149] THOMPSON, A. P., SWILER, L. P., TROTT, C. R., FOILES, S. M., AND TUCKER, G. J. Spectral neighbor analysis method for automated generation of quantum-accurate interatomic potentials. *Journal of Computational Physics* 285 (2015), 316–330.
- [150] TOGO, A., AND TANAKA, I. First principles phonon calculations in materials science. *Scripta Materialia* 108 (nov 2015), 1–5.
- [151] TSCHOPP, M. A., AND MCDOWELL, D. L. Asymmetric tilt grain boundary structure and energy in copper and aluminium. *Philosophical Magazine* 87, 25 (sep 2007), 3871–3892.

- [152] TSCHOPP, M. A., AND MCDOWELL, D. L. Structures and energies of  $\Sigma$  3 asymmetric tilt grain boundaries in copper and aluminium. *Philosophical Magazine* 87, 22 (aug 2007), 3147–3173.
- [153] TSCHOPP, M. A., SOLANKI, K. N., GAO, F., SUN, X., KHALEEL, M. A., AND HORSTEMEYER, M. F. Probing grain boundary sink strength at the nanoscale: Energetics and length scales of vacancy and interstitial absorption by grain boundaries in  $\alpha$ -Fe. *Physical Review B* 85, 6 (feb 2012), 064108.
- [154] UDAGAWA, Y., YAMAGUCHI, M., ABE, H., SEKIMURA, N., AND FUKETA, T. Ab initio study on plane defects in zirconium-hydrogen solid solution and zirconium hydride. *Acta Materialia* 58, 11 (2010), 3927–3938.
- [155] VAN DE WALLE, A., ASTA, M., AND CEDER, G. The alloy theoretic automated toolkit: A user guide. *Calphad: Computer Coupling of Phase Diagrams and Thermochemistry* 26, 4 (2002), 539–553.
- [156] VAN DE WALLE, A., AND CEDER, G. Automating first-principles phase diagram calculations. *Journal of Phase Equilibria* 23, 4 (2002), 348–359.
- [157] VAN DE WALLE, A., TIWARY, P., DE JONG, M., OLMSTED, D. L., ASTA, M., DICK, A., SHIN, D., WANG, Y., CHEN, L. Q., AND LIU, Z. K. Efficient stochastic generation of special quasirandom structures. *Calphad: Computer Coupling of Phase Diagrams and Thermochemistry* 42 (2013), 13–18.
- [158] VERDI, C., KARSAI, F., LIU, P., JINNOUCHI, R., AND KRESSE, G. Thermal transport and phase transitions of zirconia by on-the-fly machine-learned interatomic potentials. *npj Computational Materials* 7, 1 (dec 2021), 156.
- [159] VON ALFTHAN, S., HAYNES, P. D., KASKI, K., AND SUTTON, A. P. Are the structures of twist grain boundaries in silicon ordered at 0 K? *Physical Review Letters* 96, 5 (2006), 1–4.
- [160] WANG, H., CHRONEOS, A., JIANG, C., AND SCHWINGENSCHLÖGL, U. Modelling zirconium hydrides using the special quasirandom structure approach. *Physical Chemistry Chemical Physics* 15, 20 (2013), 7599.
- [161] WANG, J., SHAO, B., SHAN, D., GUO, B., AND ZONG, Y. Effect of strain on solution energy of hydrogen in alpha-zirconium from first-principle calculations. *International Journal of Hydrogen Energy* 45, 35 (jul 2020), 18001–18009.

- [162] WANG, K.-X., LI, X.-H., AND CHEN, J.-S. Surface and Interface Engineering of Electrode Materials for Lithium-Ion Batteries. *Advanced Materials* 27, 3 (jan 2015), 527–545.
- [163] WARBURTON, R. E., IDDIR, H., CURTISS, L. A., AND GREELEY, J. Thermodynamic Stability of Low- and High-Index Spinel LiMn<sub>2</sub>O<sub>4</sub> Surface Terminations. *ACS Applied Materials and Interfaces* 8, 17 (2016), 11108–11121.
- [164] WARBURTON, R. E., KIM, J. J., PATEL, S., HOWARD, J. D., CURTISS, L. A., WOLVERTON, C., BUCHHOLZ, D. B., VAUGHEY, J. T., FENTER, P., FISTER, T. T., AND GREELEY, J. Tailoring Interfaces in Solid-State Batteries Using Interfacial Thermochemistry and Band Alignment. *Chemistry of Materials* 33, 21 (nov 2021), 8447–8459.
- [165] WIMMER, E., CHRISTENSEN, M., WOLF, W., HOWLAND, W. H., KAMMENZIND, B., AND SMITH, R. W. Hydrogen in zirconium: Atomistic simulations of diffusion and interaction with defects using a new embedded atom method potential. *Journal of Nuclear Materials* 532 (2020), 152055.
- [166] WIPF, H., KAPPESSER, B., AND WERNER, R. Hydrogen diffusion in titanium and zirconium hydrides. *Journal of Alloys and Compounds* 310, 1-2 (2000), 190–195.
- [167] WOLLOCH, M., LOSI, G., CHEHAIMI, O., YALCIN, F., FERRARIO, M., AND RIGHI, M. C. High-throughput generation of potential energy surfaces for solid interfaces. *Computational Materials Science* 207, February (2022), 111302.
- [168] WOLVERTON, C., OZOLIŅŠ, V., AND ZUNGER, A. Short-range-order types in binary alloys: A reflection of coherent phase stability. *Journal of Physics Condensed Matter* 12, 12 (2000), 2749–2768.
- [169] WOLVERTON, C., AND ZUNGER, A. First-principles prediction of vacancy order-disorder and intercalation battery voltages in Li<sub>x</sub>CoO<sub>2</sub>. *Physical Review Letters* 81, 3 (1998), 606–609.
- [170] WOOD, M., AYDEMIR, U., OHNO, S., AND SNYDER, G. J. Observation of valence band crossing: the thermoelectric properties of CaZn<sub>2</sub>Sb<sub>2</sub>–CaMg<sub>2</sub>Sb<sub>2</sub> solid solution. *Journal of Materials Chemistry A* 6, 20 (2018), 9437–9444.
- [171] WU, A., RIBIS, J., BRACHET, J.-C., CLOUET, E., LEPRÊTRE, F., BORDAS, E., AND ARNAL, B. HRTEM and chemical study of an ion-irradiated chromium/zircaloy-4 interface. *Journal of Nuclear Materials* 504 (jun 2018), 289–299.

- [172] YABUUCHI, N., TAKEUCHI, M., NAKAYAMA, M., SHIIBA, H., OGAWA, M., NAKAYAMA, K., OHTA, T., ENDO, D., OZAKI, T., INAMASU, T., SATO, K., AND KOMABA, S. High-capacity electrode materials for rechargeable lithium batteries: Li<sub>3</sub>NbO<sub>4</sub>-based system with cation-disordered rocksalt structure. *Proceedings of the National Academy of Sciences of the United States of America* 112, 25 (2015), 7650–7655.
- [173] YAO, Z., CHAN, M. K., AND WOLVERTON, C. Exploring the Origin of Anionic Redox Activity in Super Li-Rich Iron Oxide-Based High-Energy-Density Cathode Materials. *Chemistry of Materials* (2022).
- [174] YAO, Z., KIM, S., HE, J., HEGDE, V. I., AND WOLVERTON, C. Interplay of cation and anion redox in Li<sub>4</sub>Mn<sub>2</sub>O<sub>5</sub> cathode material and prediction of improved Li<sub>4</sub>(Mn,M)<sub>2</sub>O<sub>5</sub> electrodes for Li-ion batteries. *Science Advances* 4, 5 (2018), eaao6754.
- [175] ZHAN, C., YAO, Z., LU, J., MA, L., MARONI, V. A., LI, L., LEE, E., ALP, E. E., WU, T., WEN, J., REN, Y., JOHNSON, C., THACKERAY, M. M., CHAN, M. K., WOLVERTON, C., AND AMINE, K. Enabling the high capacity of lithium-rich anti-fluorite lithium iron oxide by simultaneous anionic and cationic redox. *Nature Energy* 2, 12 (2017), 963–971.
- [176] ZHANG, Y., BAI, X.-M., YU, J., TONKS, M. R., NOORDHOEK, M. J., AND PHILLPOT, S. R. Homogeneous hydride formation path in  $\alpha$ -Zr: Molecular dynamics simulations with the charge-optimized many-body potential. *Acta Materialia* 111 (jun 2016), 357–365.
- [177] ZHANG, Y., JIANG, C., AND BAI, X. Anisotropic hydrogen diffusion in  $\alpha$ -Zr and Zircaloy predicted by accelerated kinetic Monte Carlo simulations. *Scientific Reports* 7, October 2016 (2017), 1–13.
- [178] ZHAO, X., SHU, Q., NGUYEN, M. C., WANG, Y., JI, M., XIANG, H., HO, K. M., GONG, X., AND WANG, C. Z. Interface structure prediction from first-principles. *Journal of Physical Chemistry C* 118, 18 (2014), 9524–9530.
- [179] ZHU, D., PENG, S., CHEN, X., GAO, X., AND YANG, T. Fabrication and characterization of Li<sub>3</sub>TaO<sub>4</sub> ceramic pebbles by wet process. *Journal of Nuclear Materials* 396, 2-3 (2010), 245–250.
- [180] ZHU, L., AMSLER, M., FUHRER, T., SCHAEFER, B., FARAJI, S., ROSTAMI, S., GHASEMI, S. A., SADEGHI, A., GRAUZINYTE, M., WOLVERTON, C., AND

- GOEDECKER, S. A fingerprint based metric for measuring similarities of crystalline structures. *The Journal of Chemical Physics* 144, 3 (jan 2016), 034203.
- [181] ZIEGLER, JAMES F. AND BIRSACK, J. P. Treatise on Heavy-Ion Science. In *Treatise on Heavy-Ion Science*, D. A. Bromley, Ed. 1985, ch. The Stopping and Range of Ions in Matter, pp. 95 – 132.
- [182] ZONG, H., PILANIA, G., DING, X., ACKLAND, G. J., AND LOOKMAN, T. Developing an interatomic potential for martensitic phase transformations in zirconium by machine learning. *npj Computational Materials* 4, 1 (dec 2018), 48.
- [183] ZUNGER, A., WEI, S.-H., FERREIRA, L. G., AND BERNARD, J. E. Special quasirandom structures. *Physical Review Letters* 65, 3 (jul 1990), 353–356.
- [184] ZUZEK, E., ABRIATA, J. P., SAN-MARTIN, A., AND MANCHESTER, F. D. The H-Zr (hydrogen-zirconium) system. *Bulletin of Alloy Phase Diagrams* 11, 4 (aug 1990), 385–395.

## Vita

- Robert E Warburton, Jae Jin Kim, **Shane Patel**, Jason D Howard Curtiss, Larry A, Chris Wolverton, D Bruce Buchholz, John T Vaughey, Paul Fenter, Timothy T Fister, Jeffrey Greeley. "Tailoring Interfaces in Solid-State Batteries Using Interfacial Thermochemistry and Band Alignment", **Chemistry of Materials** **33**, pp 8447-8459 (2021).
- Daniel Friedrich, Shiqiang Hao, **Shane Patel**, Chris Wolverton, Mercuri G Kanatzidis. "Vast Structural and Polymorphic Varieties of Semiconductors  $AMM'Q_4$  ( $A = K, Rb, Cs, Tl$ ;  $M = Ga, In$ ;  $M' = Ge, Sn$ ;  $Q = S, Se$ )", **Chemistry of Materials**, pp. 6572-6583 (2021).
- Yi Xia, Vinay I Hegde, Koushik Pal, Xia Hua, Dale Gaines, **Shane Patel**, Jiangang He, Muratahan Aykol, Chris Wolverton. "High-throughput study of lattice thermal conductivity in binary rocksalt and zinc blende compounds including higher-order anharmonicity", **Physical Review X** **10**, 041029 (2020).
- Daniel Friedrich, Hye Ryung Byun, Shiqiang Hao, **Shane Patel**, Chris Wolverton, Joon Ik Jang, Mercuri G Kanatzidis. "Layered and Cubic Semiconductors  $AGaM'Q_4$  ( $A^+ = K^+, Rb^+, Cs^+, Tl^+$ ;  $M'^4+ = Ge^{4+}, Sn^{4+}$ ;  $Q^{2-} = S^{2-}, Se^{2-}$ )

and High Third-Harmonic Generation”, **Journal of the American Chemical Society** **142** pp. 17730-17742 (2020).

- Eric B Isaacs, **Shane Patel**, Chris Wolverton. ”Prediction of Li intercalation voltages in rechargeable battery cathode materials: Effects of exchange-correlation functional, van der Waals interactions, and Hubbard U”, **Physical Review Materials** **4**, 065405 (2020).
- **Shane Patel**, Max K Amsler, Chris Wolverton. ”Predicting Interface Structures with the Minima Hopping Method”, in preparation (2023).
- **Shane Patel**, Yi Xia, Chris Wolverton. ”Phase Transformations in Zr-H using First-Principles and Machine Learning Interatomic Potentials”, in preparation (2023).
- **Shane Patel**, Jiahong Shen, Eric B Isaacs, Shiqiang Hao, Yizhou Zhu. ”The role of cation disorder in anionic redox in  $\text{Li}_3\text{MO}_4$  cathodes”, in preparation (2023).